Tokyo Metropolitan University

Doctoral Thesis

Particle Identification using the Aerogel RICH Counter at the Belle II Experiment

Author:
Masanobu Yonenaga

Supervisor:
Prof. Hidekazu Kakuno

A dissertation submitted in partial fulfillment of the requirements
for the degree of Doctor of Philosophy in Science

in the

High Energy Physics Group
Department of Physics
Science and Engineering

August, 2020

Abstract

The Standard Model (SM) has been completed by observing the Higgs boson which is a last particle expected by the SM in 2012. However, the SM cannot explain non-zero neutrino mass, existence of dark matter and lack of gravity and so on. Therefore, we need the new physics (NP) beyond the SM to explain those things. The energy frontier experiment which directly produce the NP particles using high energy collision doesn't find the sign of the NP so far, and the NP is expected to exist in the more high energy region. The luminosity frontier experiment which find the signature of NP in the intermediate state can reach more high energy region by precise measurement, and expected to discover the NP.

The Belle II experiment is a luminosity frontier experiment and is searching NP by studying CP asymmetry and rare decays of B and D mesons and τ leptons using high statistic data. Discrimination for CP eigenstate and rare decay process in wide momentum region is required to study precisely. Therefore, particle identification has an important role to measure rare decays with high precision to search NP. We have developed a new particle identification device in the forward end-cap region at the Belle II spectrometer called the aerogel Ring Imaging Cherenkov (ARICH) counter to realize particle identification in high accuracy for charged particles with momenta up to $4\,\mathrm{GeV}/c$.

The ARICH counter consists of a silica aerogel layer as the radiator and Hybrid Avalanche Photo Detector (HAPD) as the photon detector. The construction was completed in October 2018 and the ARICH counter was installed into the Belle II spectrometer in December 2018. We evaluated the particle identification performance of ARICH using $D^* \to D^0(\to K\pi)\pi$ decays with early beam collision data which correspond to an integrated luminosity of $5.15\,\mathrm{ab}^{-1}$. The result of overall performance of ARICH shows that $K(\pi)$ efficiency is $93.5 \pm 0.6\%$ ($87.5 \pm 0.9\%$) with $\pi(K)$ misidentification probability of $10.9 \pm 0.9\%$ ($5.6 \pm 0.3\%$). We also evaluated the dependance of the performance on the particle momentum or polar angle, and the results demonstrate that ARICH has capability to identify particles for all regions.

A $b \to s(d)\gamma$ process induced by the Flavor Changing Neutral Current (FCNC), and is forbidden at the tree level diagram and occur through a loop level diagram in the SM. The particles indicated in new physics beyond the SM such as charged Higgs boson and supersymmetric particles can contribute in the loop, therefore, the process is a good probe to search new physics. $b \to s(d)\gamma$ process can be observed in Bmeson decays such as $B \to \rho(\to \pi\pi)\gamma$ and $B \to K^*(\to K\pi)\gamma$.

We search $B \to K^*\gamma$ decays using the early Belle II data collected between March and May in 2019 which corresponds to an integrated luminosity of $2.62\,\mathrm{fb}^{-1}$, aiming to demonstrate that the Belle II operation in total. The result shows that the number of signals are 19.1 ± 5.2, 9.8 ± 3.4 and 6.6 ± 3.1 for $B^0 \to K^{*0}(\to K^+\pi^-)\gamma$, $B^+ \to K^{*+}(\to K^+\pi^0)\gamma$ and $B^+ \to K^{*+}(\to K^0_S\pi^+)\gamma$, respectively. This results are consistent with a Monte Carlo simulation of Belle II and the world average. The combined significance of the $B \to K^*\gamma$ decays is $6.2\,\sigma$, and we rediscover the $B \to K^*\gamma$ decays with the significance more than $5\,\sigma$. We demonstrate that the Belle II has capability to search rare B decays as expected through rediscovering $B \to K^*\gamma$ decays.

Acknowledgements

First of all, I would like to express my sincere gratitude to my supervisor, Professor Hidekazu Kakuno. He gave me a lot of constructive advices and suggestions from various points while also taking into account my thoughts, and led the right direction. I couldn't have been able to complete this thesis without it. I cannot thank you enough for what he has supported me.

I would like to express my appreciation to Professor Takayuki Sumiyoshi who continuously encourages me. His comments, not only in the laboratory but also on the drives to Tsukuba, are a valuable asset to me.

I would like to thank all members of the Belle II ARICH group, especially, Professor Ichiro Adachi and Professor Shohei Nishida. They give me many valuable comments and suggestions for my works, slides, documents, and so on. Their support on site has helped me grow as an experimentalist.

I am grateful to the members of Slovenia, especially, Dr. Luka Šantelj who gives me the instruction in ARICH software and consultation about ARICH analysis. I would also like to thank Professor Peter Križan, Professor Samo Korpar, Professor Rok Pestotnik, and Dr. Manca Mrvar. They gently discuss with me, even though my English is poor, and gave me critical and practical comments. Besides, I could enjoy my life in Slovenia thanks to them. It's no exaggeration to say Slovenia is my second hometown.

A special gratitude I give to Associate Professor Akimasa Ishikawa for his generous guidance for physics analysis. Daily meeting with him during the most exciting days of physics analysis at Belle II is one of the hardest and growing days in my life.

I would like to appreciate Dr. Tetsuro Kumita who helps many times with his English knowledge. Thanks to him, I have always enjoyed my life in the laboratory. I would appreciate to Dr. Tomoyuki Konno of Kitasato University. I'm not quite there yet, but I learned coding and software from him. Also, an unreserved discussion with him about various topics were really helpful. I would like to thank Dr. Shuichi Iwata who kindly taught me the basics of the experiment. It is my good fortune to meet him in the first period of my life as an experimentalist. I would thank Dr. Miki Nishimura. I worked with her at last year of my KEK life, her cheerfulness has made my life at KEK dramatically more enjoyable.

I thank present and left peoples of high energy physics group at TMU and other institutes who are able to have casual and in-depth discussions with me and it's very helpful for me. Especially, I would thank my friend Mr. Kazuya Ogawa of Niigata University who is my peer and I spent many great times with him at KEK and conference and so on.

Finally, I thank my family, my father Shinji, my mother Hiromi, and my sister Misato for their supports and understandings for my mind. And I'm grateful to all of the people who helped and encouraged me.

Masanobu YONENAGA

Contents

List of Figures

List of Tables

Chapter 1

Introduction

The universe dominates matters, although anti-matter, the particle having same mass and inverse charge of particle, must be generated same amount when the universe is birthed. To explain this particle dominant universe, anti-particles must be disappeared. Conditions to disappear anti-particles are called Sakharov conditions [1]: baryon number violation, C-symmetry and CP-symmetry violation, and interactions out of thermal equilibrium. CP violation was first observed in Kaon system [2] and quark mixing among three generations naturally explains this CP violation in the Standard Model (SM) [3]. However, the scale of CP violation in the SM is still too small to explain the matter dominant universe. Furthermore, the SM doesn't explain some measurement like mass of neutrino and existence of dark matter. In terms of theory, the SM is not a beautiful theory since the SM has three interactions and too many parameters which cannot defined by theoretical calculation. Therefore, the SM is not an ultimate theory of particle physics and new physics (NP) beyond the SM surely exist.

There are two approaches to search NP: the energy frontier experiments and the luminosity frontier experiments. The energy frontier experiments directly produce new particles using high energy collision, and it is sensitive to the energy scale of new physics. The luminosity frontier experiments find signatures of NP particles in intermediate states, and it is sensitive to the flavor structure of new physics. There are no signature of NP at the energy frontier experiment: LHC so far at the center-mass-system energy of 13 TeV. Thus, NP is expected to exist in higher energy region. The luminosity frontier experiment can reach to higher energy region using strong coupling modes. Therefore, we expect to find signatures of NP at the luminosity frontier experiment.

The Belle II experiment, the luminosity frontier experiment only operating today, has started collecting beam collision data, and aims to search NP beyond the SM with high statistics data of B-meson, D-meson and τ-lepton decays. One of the good probes to search NP in B-meson decays is $b \to s(d)\gamma$ process. $b \to s(d)\gamma$ process is experimentally observed in such as $B \to \rho(\to \pi\pi)\gamma$ decays and $B \to K^*(\to K\pi)\gamma$ decays. Particle identification up to $4\,\mathrm{GeV}/c$ is needed for precisely separate those two decay modes. The aerogel Ring Imaging Cherenkov (ARICH) counter has been developed to realize particle identification up to $4\,\mathrm{GeV}/c$ a the forward endcap region of the Belle II spectrometer.

The organization of this thesis is as follows: chapter 2 introduces the theoretical framework and motivation, chapter 3 summarizes the Belle II experiment including the Belle II spectrometer and the SuperKEKB accelerator, chapter 4 describes the ARICH counter, chapter 5 mentions installation and healthiness under the practical operation environment chapter 6 presents the results particle identification performance of ARICH, chapter 7 explains a study of $B \to K^{*}\gamma$ decay, and chapter 8 discusses the results of search of $B \to K^{*}\gamma$ at Belle II. Finally, chapter 9 concludes this thesis.

Chapter 2

The Standard Model and *B* physics

In this chapter, the theoretical framework of the Standard Model and *B* physics is described, and interesting physics is introduced.

2.1 The Standard Model

The Standard Model (SM) of particle physics is experimentally established by the observation of Higgs boson at the ATLAS experiment [4] and the CMS experiment [5] in 2012 [6, 7] at LHC accelerator [8]. The summary of the SM particles are shown in Figure 2.1. The SM is the best theory to naturally describe the results of particle physics so far.

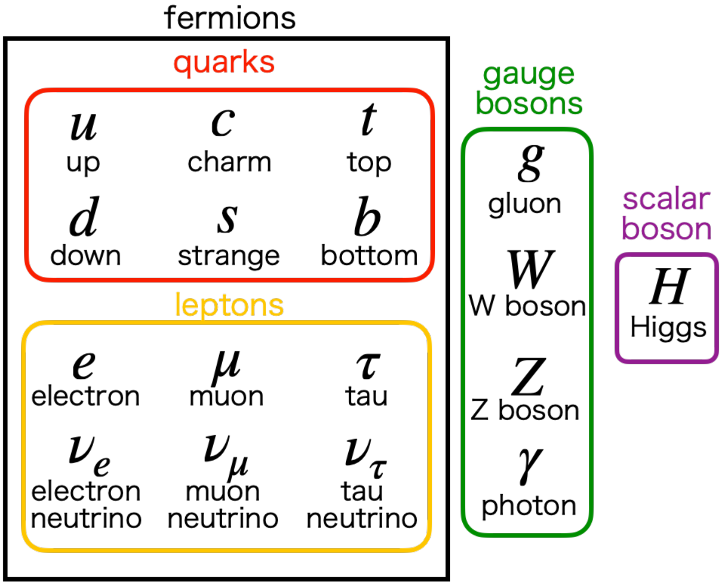

FIGURE 2.1: Summary of the SM particles.

The SM is constructed from gauge theory and the gauge group is $SU(3)_{\mathrm{C}} \times SU(2)_{\mathrm{L}} \times U(1)_{\mathrm{Y}}$. Each term of gauge group corresponds to color, weak isospin and weak hyper charge for $SU(3)_{\mathrm{C}}$, $SU(2)_{\mathrm{L}}$ and $U(1)_{\mathrm{Y}}$, respectively. Gauge field mediates interactions and it is quantized as a gauge boson. $SU(3)_{\mathrm{C}}$ mediates strong interaction and its gauge boson is gluon (g). $SU(2)_{\mathrm{L}} \times U(1)_{\mathrm{Y}}$ mediates weak and electromagnetic interactions after the spontaneous symmetry breaking. Gauge boson for weak interaction is weak boson ($Z^0, W^{\pm}$), and for electromagnetic interaction is photon (γ).

The Lagrangian of the SM can be divided into four parts:

$$\mathcal{L}_{\mathrm{SM}} = \mathcal{L}_{\mathrm{Higgs}} + \mathcal{L}_{\mathrm{fermion}} + \mathcal{L}_{\mathrm{gauge}} + \mathcal{L}_{\mathrm{Yukawa}}. \tag{2.1}$$

The Yukawa interaction of quarks with three generations is

$$\mathcal{L}_{\mathrm{Yukawa}} = -\bar{q_L} f_d d_R \phi - \bar{q_L} f_u u_R \tilde{\phi} + h.c., \tag{2.2}$$

where f_d and f_u are 3×3 matrix of Yukawa coupling constant. q_L, u_R and d_R are quark fields and they are three-dimensional vectors correspond to three generations,

$$q_L = \begin{pmatrix} q_{L1} \\ q_{L2} \\ q_{L3} \end{pmatrix}, u_R = \begin{pmatrix} u_{R1} \\ u_{R2} \\ u_{R3} \end{pmatrix}, d_R = \begin{pmatrix} d_{R1} \\ d_{R2} \\ d_{R3} \end{pmatrix}. \tag{2.3}$$

ϕ is Higgs field. Considering mixing transformation of three generations, the quark fields can be rewritten as

$$q_L \to U_{qL} q_L, \quad u_R \to U_{uR} u_R, \quad d_R \to U_{dR} d_R, \tag{2.4}$$

where U_{qL}, U_{uR}, U_{dR} are 3×3 unitary matrix. Applying this transformation, Equation 2.2 can be rephrased as

$$\mathcal{L} = -\bar{q_L} U_{qL}^{\dagger} f_d U_{dR} d_R \phi - \bar{q_L} U_{qL}^{\dagger} f_u U_{uR} u_R \tilde{\phi} + h.c. \tag{2.5}$$

By replacing Higgs field with the vacuum state,

$$\mathcal{L} = -\bar{u_L} G_d d_R - \bar{d_L} G_u u_R + h.c. \tag{2.6}$$

where u_L and d_R are element of q_L for $I_3 = +1/2, -1/2$, respectively. Moreover,

$$G_{u,d} = \frac{v}{\sqrt{2}} f_{u,d} \tag{2.7}$$

is called "mass matrix" for quark with charge $+2/3$ and $-1/3$. $f_{u,d}$ is generally complex number, thus, mass matrix is also complex matrix. This can be diagonalized with two unitary matrix as follow:

$$G_u = V_{uL}^{\dagger} M_u V_{uR}, \quad G_d = V_{dL}^{\dagger} M_d V_{dR}, \tag{2.8}$$

where $M_{u,d}$ are diagonal matrixes and expressed as

$$M_u = \begin{pmatrix} m_u & & \\ & m_c & \\ & & m_t \end{pmatrix}, M_d = \begin{pmatrix} m_d & & \\ & m_s & \\ & & m_b \end{pmatrix} \tag{2.9}$$

Furthermore, mass eigenstate of quark for left- and right- handed can be defined as

$$V_{uL}u_L = \begin{pmatrix} u_L \\ c_L \\ t_L \end{pmatrix}, V_{dR}d_R = \begin{pmatrix} d_R \\ s_R \\ t_R \end{pmatrix} \tag{2.10}$$

Charged current interaction is

$$\mathcal{L} = -\frac{g}{\sqrt{2}}\bar{u}_L\gamma^\mu d_L W^\dagger_\mu. \tag{2.11}$$

This can be rephrased with mass eigenstate

$$\mathcal{L} = -\frac{g}{\sqrt{2}}\bar{u}_L\gamma^\mu V_{uL}V^\dagger_{dL}d_L W^\dagger_\mu. \tag{2.12}$$

This is not diagonal. The unitarity matrix $V_{uL}V^\dagger_{dL}$ in the Equation 2.12 is called the Cabibbo-Kobayashi-Maskawa (CKM) matrix.

2.1.1 The CKM matrix

One of the important consequence of the SM is CP violation arisen in quark sector. This is induced by the CKM matrix [3, 9]. It denotes the relation between mass eigenstates (d, s, b) and weak interaction eigenstates (d', s', b'). Weak interaction eigenstates mixture three mass eigenstates by the 3×3 matrix V_{CKM} which is defined as follows:

$$\begin{pmatrix} d' \\ s' \\ b' \end{pmatrix} = V_{\text{CKM}} \begin{pmatrix} d \\ s \\ b \end{pmatrix} = \begin{pmatrix} V_{ud} & V_{us} & V_{ub} \\ V_{cd} & V_{cs} & V_{cb} \\ V_{td} & V_{ts} & V_{tb} \end{pmatrix} \begin{pmatrix} d \\ s \\ b \end{pmatrix}. \tag{2.13}$$

Because the CKM matrix is unitarity matrix, the product of the CKM matrix and its Hermitian matrix $V^\dagger_{\text{CKM}}$ equals to unit matrix as follows:

$$V_{\text{CKM}}V^\dagger_{\text{CKM}} = V^\dagger_{\text{CKM}}V_{\text{CKM}} = \begin{pmatrix} 1 & 0 & 0 \\ 0 & 1 & 0 \\ 0 & 0 & 1 \end{pmatrix}. \tag{2.14}$$

Non-diagonal components of Equation 2.14 derive the following six equalities:

$$\begin{aligned}
V_{ud}V^*_{cd} + V_{us}V^*_{cs} + V_{ub}V^*_{cb} &= 0, && (2.15)\\
V_{ud}V^*_{us} + V_{cd}V^*_{cs} + V_{td}V^*_{ts} &= 0, && (2.16)\\
V_{cd}V^*_{td} + V_{cs}V^*_{ts} + V_{cb}V^*_{tb} &= 0, && (2.17)\\
V_{us}V^*_{ub} + V_{cs}V^*_{cb} + V_{ts}V^*_{tb} &= 0, && (2.18)\\
V_{ud}V^*_{td} + V_{us}V^*_{ts} + V_{ub}V^*_{tb} &= 0, && (2.19)\\
V_{ud}V^*_{ub} + V_{cd}V^*_{cb} + V_{td}V^*_{tb} &= 0. && (2.20)
\end{aligned}$$

These equalities donate six triangles in the complex plane, which are called unitarity triangles. Areas of unitarity triangles equal the magnitude of CP violation and their are same for all six triangles. Each term of those equations donate each side of the unitarity triangle.

The other expression of CKM matrix which is called the Wolfenstein parameterization [10] is useful to understand the shapes of unitarity triangles. It has only four parameters: A, λ, ρ, and η. Using the expression, the CKM matrix is rephrased as

$$V_{\mathrm{CKM}} = \begin{pmatrix} 1-\frac{1}{2}\lambda^2 & \lambda & A\lambda^3(\rho - i\eta) \\ -\lambda & 1-\frac{1}{2}\lambda^2 & A\lambda^2 \\ A\lambda^3(1-\rho-i\eta) & -A\lambda^2 & 1 \end{pmatrix} + \mathcal{O}(\lambda^4). \tag{2.21}$$

The complex phase at corner of the matrix can induce CP violation. Four parameters are measured [11]:

$$\begin{aligned} A &= 0.8235^{+0.0056}_{-0.0145}, \\ \lambda &= 0.223837^{+0.000251}_{-0.000060}, \\ \bar{\rho} &= 0.1569^{+0.0102}_{-0.0061}, \\ \bar{\eta} &= 0.3499^{+0.0079}_{-0.0065}. \end{aligned}$$

$\bar{\rho}$ and $\bar{\eta}$ are rephrased as

$$\bar{\rho} + i\bar{\eta} = \frac{V_{ud}V_{ub}^*}{V_{cd}V_{cb}^*}, \tag{2.22}$$

$$\bar{\rho} = \rho(1-\lambda^2/2 + \mathcal{O}(\lambda^4)), \tag{2.23}$$

$$\bar{\eta} = \eta(1-\lambda^2/2 + \mathcal{O}(\lambda^4)). \tag{2.24}$$

Since λ is small, diagonal components of the matrix is dominant. It means that mixing of same generation is dominant.

Unitarity triangles are useful to verify the Kobayashi-Maskawa theory in the SM since they must be completely closed in the SM. Therefore, it suggests NP if unitarity triangles are not closed. Here, considering unitarity triangles at each generational transition from six equations (Equation 2.15 - 2.20). The order of λ is as follows:

- 1st $\longleftrightarrow$ 2nd (Equation 2.15 and 2.16): $\mathcal{O}(\lambda) + \mathcal{O}(\lambda) + \mathcal{O}(\lambda^5)$
- 2nd $\longleftrightarrow$ 3rd (Equation 2.18 and 2.17): $\mathcal{O}(\lambda^4) + \mathcal{O}(\lambda^2) + \mathcal{O}(\lambda^2)$
- 1st $\longleftrightarrow$ 3rd (Equation 2.19 and 2.20): $\mathcal{O}(\lambda^3) + \mathcal{O}(\lambda^3) + \mathcal{O}(\lambda^3)$

The unitarity triangles related to transition between first and second generation are flattest triangle. On the contrary, transition between first and third generation donate sharpest triangles since all terms are same order of λ and lengths of all sides are comparable. The most commonly used unitarity triangle is the one built from Equation 2.20 and it is shown in Figure 2.2. The three angles defined as follows:

$$\phi_1 = \beta \quad = \quad \arg\left(-\frac{V_{cd}V_{cb}^*}{V_{td}V_{tb}^*}\right), \tag{2.25}$$

$$\phi_2 = \alpha \quad = \quad \arg\left(-\frac{V_{td}V_{tb}^*}{V_{ud}V_{ub}^*}\right), \tag{2.26}$$

$$\phi_3 = \gamma \quad = \quad \arg\left(-\frac{V_{ud}V_{ub}^*}{V_{cd}V_{cb}^*}\right). \tag{2.27}$$

Sides and angles of the unitarity triangle are measured by various measurements. The constrains in the $(\bar{\rho}, \bar{\eta})$ plane is shown in Figure 2.3. The unitarity triangle is closed so far and there is no signature of NP in various constrains on the unitarity triangle.

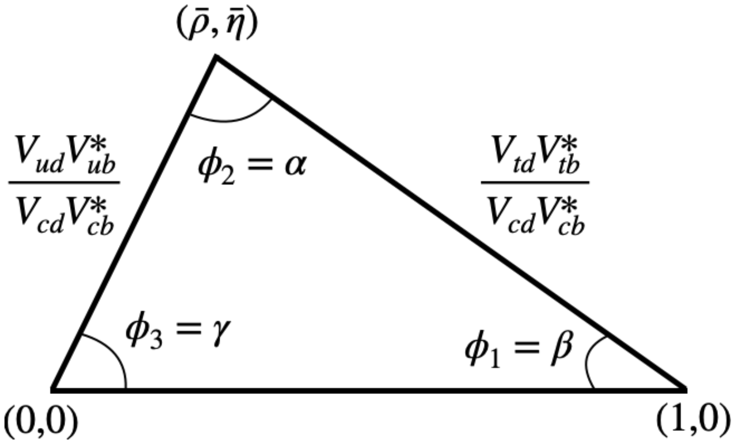

FIGURE 2.2: The unitarity triangle corresponds to Equation 2.20. Each side is divided by $V_{cd}V_{cb}^*$.

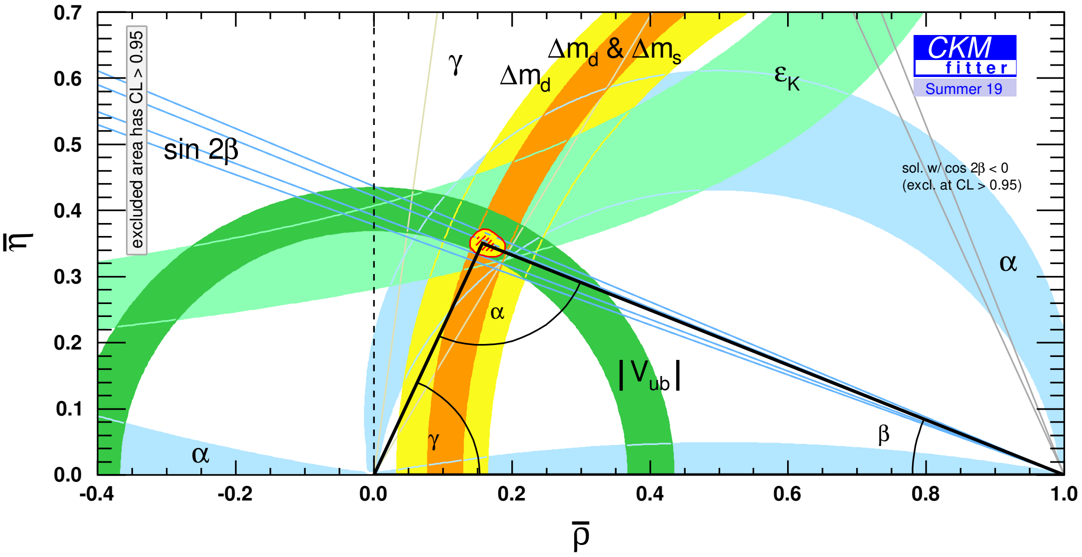

FIGURE 2.3: Constrains in the $(\bar{\rho}, \bar{\eta})$ plane [11]. The red hashed region of the global combination corresponds to 68% CL.

2.1.2 Problems in the SM

The SM describes many results of the particle physics so far. However, there are some observations which cannot be explained by the SM:

- Non-zero neutrino mass
  - Mass of neutrino is assumed to be zero in the SM. However, non-zero neutrino mass is proved by observing neutrino oscillation phenomena [12].
- no candidates of dark matter
  - Through observations in astrophysics [13], dark matter should exist in the universe. However, there are no candidate particles in the SM.
- no gravity
  - The SM includes only strong, weak and electromagnetic interactions. However, there are one additional interaction for gravity.

Therefore, the SM is not an ultimate goal of the particle physics and new physics (NP) beyond the SM surely exist.

2.2 B physics

One of the good probe to search NP is decays of B-meson which contains b quark. b quark is the heaviest quark that can be produced hadron and decays into light quarks. This decays correspond to un-dominant part of the CKM matrix and its contribution is small. In addition, all sides and angles of the unitarity triangle can be measured by B-meson decays. Therefore, it is expected to search small contribution from NP by comparing with the prediction of the SM.

2.2.1 B factory experiment

The Bfactory experiment generates $B\bar{B}$ pairs through decays of $\Upsilon(4S)$, the fourth primary excited state of $b\bar{b}$ resonance, produced by annihilation of e^+e^-. The energy of electron beam and positron beam is tuned to be 10.58 GeV, which corresponds to the mass of $\Upsilon(4S)$, in the center mass system.

The CP violation in the B-meson system can be observed by measuring specific B-meson decay processes. Here, we consider the decays from both B^0 and $\bar{B^0}$ into CP eigenstate such as $J/\psi K^0_S$. It occurs through the tree diagram as shown in Figure 2.4. Before decay into $J/\psi K^0_S$, B^0 meson and $\bar{B^0}$ meson can be coherently changed to each other by $B^0 - \bar{B^0}$ mixing as shown in Figure 2.5.

Decaying into the same state via two different processes, interference due to $B^0 - \bar{B^0}$ mixing is anticipated, and the time dependent interference between B^0 decay and $\bar{B^0}$ decay into CP eigenstate give rise to the CP violation through complex phase in the mixing and decay amplitudes. This effect can be measured as the time dependent asymmetry between B^0 meson and $\bar{B^0}$

meson, which is written as follows:

$$A_{CP}(\Delta t) = \frac{\Gamma(\bar{B}^0 \to J/\psi K_S^0) - \Gamma(B^0 \to J/\psi K_S^0)}{\Gamma(\bar{B}^0 \to J/\psi K_S^0) - \Gamma(B^0 \to J/\psi K_S^0)} \tag{2.28}$$

$$= \sin 2\phi_1 \sin \Delta m \Delta t, \tag{2.29}$$

where Γ is the decay fraction, Δm is the mass difference between two B^0 mass eigenstates (B_H and B_L), and ϕ_1 is one of the angle of the unitarity triangle.

The Belle experiment and the Babar experiment [14] observed CP asymmetry in B-meson system [15, 16] in 2002.

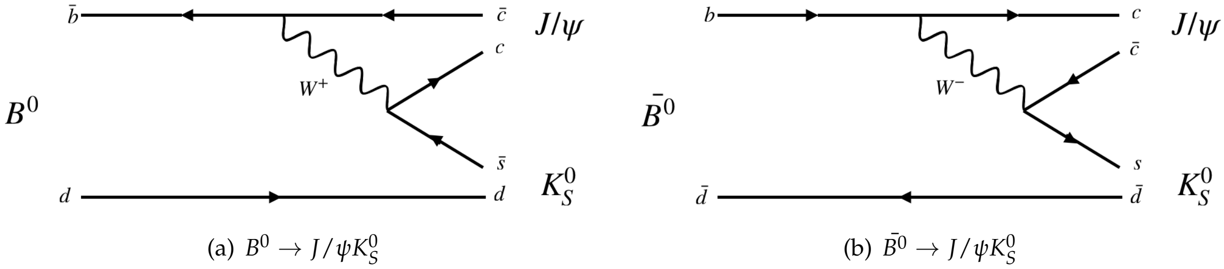

(a) $B^0 \to J/\psi K_S^0$ (b) $\bar{B}^0 \to J/\psi K_S^0$

FIGURE 2.4: The Feynman diagram of (a) $B^0 \to J/\psi K_S^0$ decay and (b) $\bar{B}^0 \to J/\psi K_S^0$ decay.

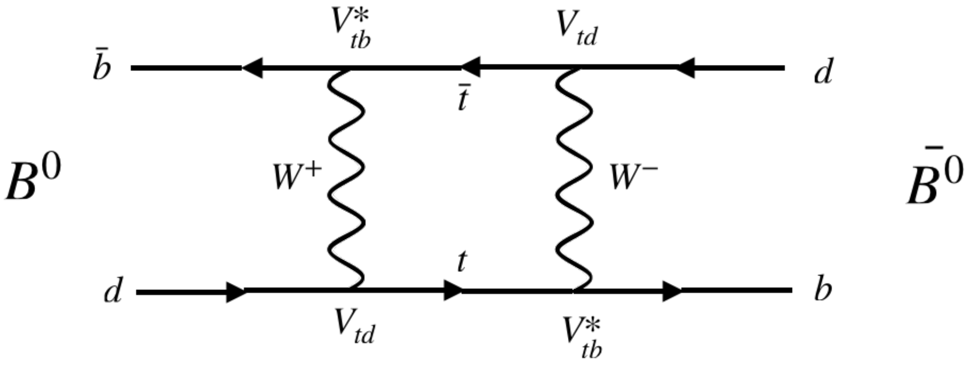

FIGURE 2.5: The Feynman diagram of $B^0 - \bar{B}^0$ mixing.

2.3 Radiative penguin decay

Flavor changing neutral current (FCNC) is forbidden in the SM at the leading order process that is expressed by a tree diagram. It only occurs through the next leading order that can be expressed by a loop diagram. Most major diagram is one-loop diagram via a W-boson and an up type quark (top quark is dominant). The radiative decay with flavor change is clear FCNC process and two FCNC processes, $b \to s\gamma$ and $b \to d\gamma$, are possible in B-meson as shown in Figure 2.6. This process is sensitive to NP since the decay is relatively clean and the SM can predict its decay with low uncertainty, while NP particles such as charged Higgs boson and supersymmetric particles can contribute in the loop as a virtual particle.

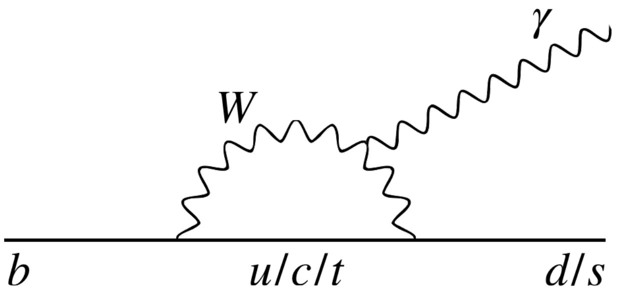

FIGURE 2.6: Feynman diagram of $b \to s(d)\gamma$ process.

2.3.1 $b \to s\gamma$ decays

One of the exclusive decay process of $b \to s\gamma$ transition is $B \to K^*\gamma$ decay. $B \to K^*\gamma$ is first observed at the CLEO experiment [17] with 1377 pb^{-1} integrated luminosity [18]. They searched $B \to K^*\gamma$ using the following three decay modes:

- $B^0 \to K^{*0}(\to K^+\pi^-)\gamma$
- $B^+ \to K^{*+}(\to K^+\pi^0)\gamma$
- $B^+ \to K^{*+}(\to K^0_S\pi^+)\gamma$

Assuming the branching ratio of the charged and the neutral decay mode are same, the average branching ratio is obtained to be $(4.5 \pm 1.5 \pm 0.9) \times 10^{-5}$.

The Belle experiment [19] provides the latest and the most precise results of $B \to K^*\gamma$ measurement including $B^0 \to K^{*0}(\to K^0_S\pi^0)\gamma$ [20]. The results of the combined branching ratios $\mathcal{B}(B^0 \to K^{*0}\gamma)$ and $\mathcal{B}(B^+ \to K^{*+}\gamma)$, direct CP asymmetries $A_{CP}(B^0 \to K^{*0}\gamma)$ and $A_{CP}(B^+ \to K^{*+}\gamma)$, isospin asymmetry Δ_{0+}, the difference between and average of direct CP asymmetries between charged and neutral Δ_{CP} and $\bar{A_{CP}}$ are

$$\begin{aligned}
\mathcal{B}(B^0 \to K^{*0}\gamma) &= (3.96 \pm 0.07 \pm 0.14) \times 10^{-5}, \\
\mathcal{B}(B^+ \to K^{*+}\gamma) &= (3.76 \pm 0.10 \pm 0.12) \times 10^{-5}, \\
A_{CP}(B^0 \to K^{*0}\gamma) &= (-1.3 \pm 1.7 \pm 0.4)\%, \\
A_{CP}(B^+ \to K^{*+}\gamma) &= (+1.1 \pm 2.3 \pm 0.3)\%, \\
\Delta_{0+} &= (+6.2 \pm 1.5 \pm 0.6 \pm 1.2)\%, \\
\Delta A_{CP} &= (+2.4 \pm 2.8 \pm 0.5)\%, \\
\bar{A}_{CP} &= (-0.1 \pm 1.4 \pm 0.3)\%,
\end{aligned}$$

where the first and second uncertainty are statistical and systematic, respectively, and the third uncertainty of Δ_{0+} is due to uncertainty of the ratio of decay constants f_{+-}/f_{00}. Those results are the most precise measurements in the world. It is the first evidence for isospin violation in $B \to K^*\gamma$ with a significance of $3.1\,\sigma$. The dominant error of A_{CP} is statistical uncertainty. The Belle II experiment can reduce the statistical error using much higher statistics.

2.3.2 $b \to d\gamma$ decays

Exclusive $b \to d\gamma$ process, $B \to \rho\gamma$ and $B \to \omega\gamma$, has been observed by the Belle experiment [21] and the Babar experiment [22]. The latest measurement at the Belle experiment provides the branching fractions, isospin asymmetry and CP asymmetry using $B^+ \to \rho^+\gamma$, $B^0 \to \rho^0\gamma$ and $B^0 \to \omega\gamma$ decays as follows [23]:

$$\begin{aligned}
\mathcal{B}(B^+ \to \rho^+\gamma) &= (8.7^{+2.9+0.9}_{-2.7-1.1}) \times 10^{-7}, \\
\mathcal{B}(B^0 \to \rho^0\gamma) &= (7.8^{+1.7+0.9}_{-1.6-1.0}) \times 10^{-7}, \\
\mathcal{B}(B^0 \to \omega\gamma) &= (4.0^{+1.9}_{-1.7} \pm 1.3) \times 10^{-7}, \\
A_{CP}(B^+ \to \rho^+\gamma) &= (-0.11 \pm 0.32 \pm 0.09)\%, \\
\Delta_{\rho\gamma} &= (-0.48^{+0.21+0.08}_{-0.19-0.09})\%,
\end{aligned}$$

where the first and second error are statistical and systematic, respectively. Those results agreed well with the previous measurement and the SM expectation. However, uncertainty is large due to low statistics and measurement using high statistics data can improve this result.

2.4 New physics search

One of the most promising candidate of NP is the Supersymmetry (SUSY). It introduces a symmetry between bosons and fermions. The model extended SM to include SUSY is called the Minimal Supersymmetric SM (MSSM). However, it has too many parameters and some model with constrained parameters is considered.

The minimal Super-Gravity (mSUGRA) has only five parameters: m_0, $m_{1/2}$, A, $\tan\beta$, and μ. m_0 is mass of scalar particle in the GUT scale, $m_{1/2}$ is mass of gaugino, A is trilinear coupling constant, $\tan\beta$ is fraction of the two Higgs vacuum expectation, and μ is the mixing parameter of Higgs. The isospin asymmetry of $B \to K^*\gamma$ has relation to mSUGRA parameters space [24, 25]. The theoretical calculation for mSUGRA is shown in Figure 2.7. The 95 % confidence levels of world average and latest measurement [26] to $m_{1/2}$ and $\tan\beta$ are also shown. Originally, isospin asymmetry can take non-zero value even in the SM due to local 4-quark operations, the chrome-magnetic dipole operator, and the charm penguin [27]. Thus, it is not a direct sign of NP if isospin violation is found. However, it can constrain the mSUGRA parameter space. Uncertainty of isospin asymmetry is expected to be reduced by Belle II and strict constrains of those parameters are expected.

Other models are Minimal Flavor Violation (MFV) [28] and extended-MFV (EMFV) [29]. Figure 2.8 shows constrains on $\Delta(\rho\gamma) - R(\rho\gamma/K^*\gamma)$ and $A_{CP}(\rho\gamma) - R(\rho\gamma/K^*\gamma)$ planes. Latest measurement has large uncertainty due to insufficient statistics. More precise measurement by Belle II with high statistics data can reduce and is expected to verify the the signature of NP.

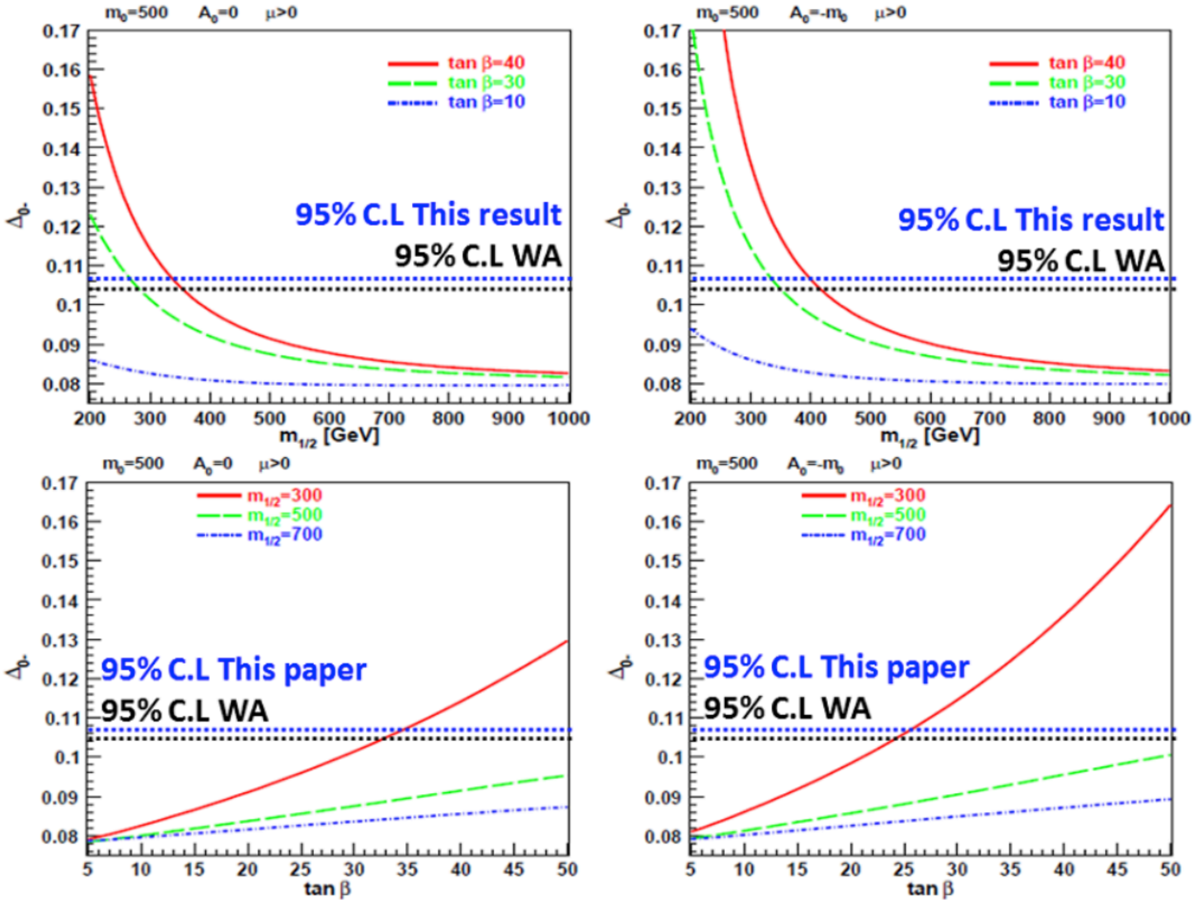

FIGURE 2.7: The relation between isospin asymmetry and $m_{1/2}$ or $\tan\beta$ with $A = 0$ and $A = -m_0$[26].

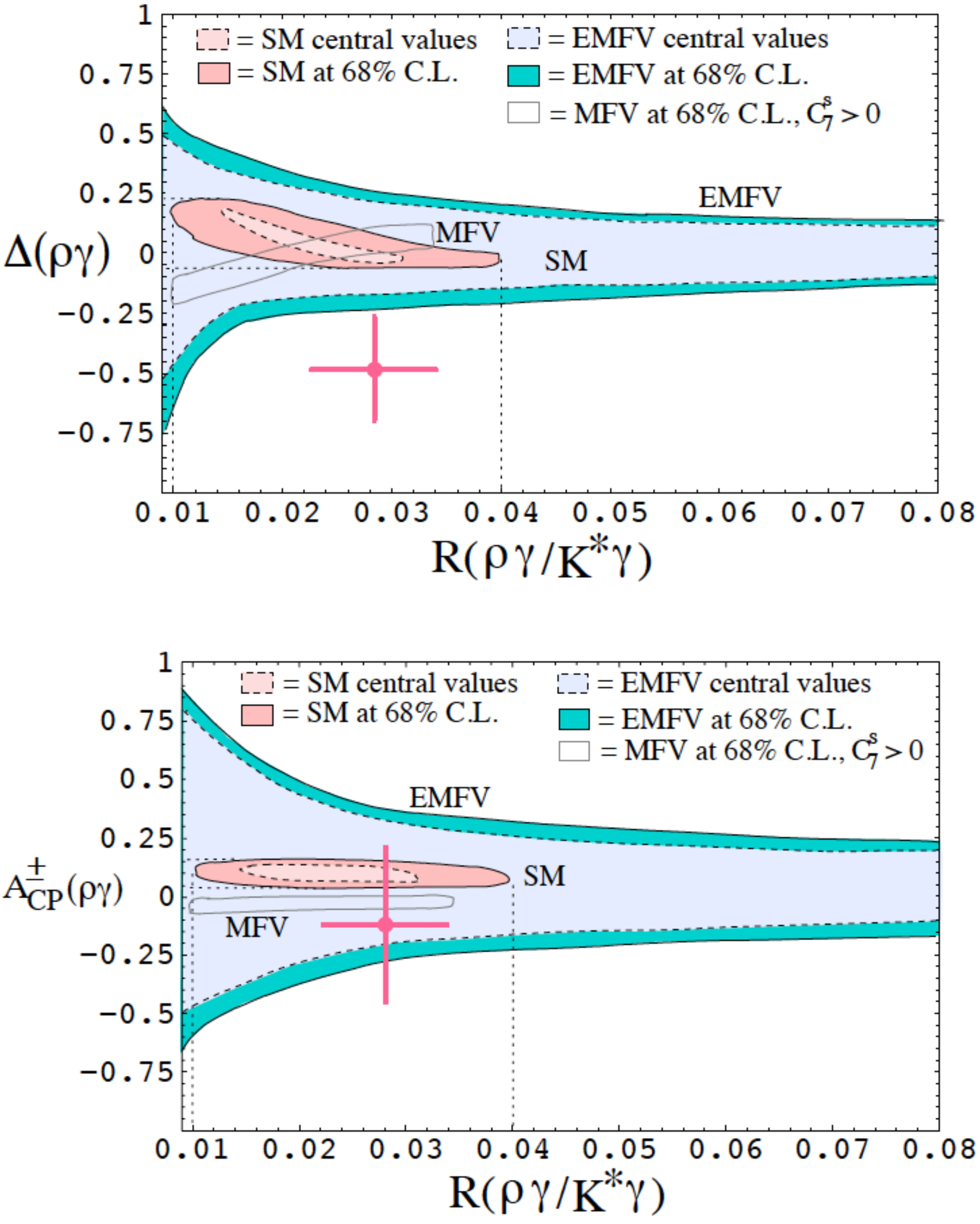

FIGURE 2.8: Correlation between $R(\rho\gamma/K^*\gamma)$ and $\Delta(\rho\gamma)$ (top) or A_{CP} (bottom) in the SM and the MFV and EMFV [30]. Dots are results of latest measurement [31].

Chapter 3

The Belle II experiment

In this chapter, the SuperKEKB accelerator and the Belle II spectrometer for the Belle II experiment are described.

3.1 The SuperKEKB accelerator

The SuperKEKB accelerator is an asymmetric energy e^+e^- collider located at High Energy Accelerator Organization (KEK) in Tsukuba, Japan, which is upgraded from the KEKB accelerator [32, 33]. The schematic view of the SuperKEKB accelerator with main components is shown in Figure 3.1.

The number of events of a physics process is written as the following formula [34]:

$$N = \int_0^T L\sigma dt, \tag{3.1}$$

where L is the luminosity, σ is the cross section of the given physics process, and T is the experiment period. To increase the number of events of a physics process within the given experimental period, σ and T are given parameters and L is only the parameter that can be increased by technical effort. The luminosity is given by [35]:

$$L = \frac{\gamma_\pm}{2er_e}\left(\frac{I_\pm \xi_{y\pm}}{\beta_y^*}\right)\left(\frac{R_L}{R_{\xi_y}}\right), \tag{3.2}$$

where γ, e, and r_e are the Lorentz factor, the elementary charge, and the electron classical radius, respectively. "+" denotes positrons beam and "–" denotes electron beam. R_L and R_{ξ_y} represent reduction factors for the luminosity and the vertical beam-beam parameter, respectively. The ratio of those parameters is usually not far from unity. Therefore, the luminosity is mainly determined by three parameters: the total beam current (I), the vertical beam-beam parameter (ξ_y), and the vertical beta function at the IP (β_y^*). Table 3.1 shows those three values, beam energy, crossing angle, and luminosity of SuperKEKB for designed value and KEKB for achieved value [34, 36]. Beam currents are two times larger, ξ_y are almost the same, and β_y^* is reduced by a factor of 1/20. Therefore, we expect the luminosity of SuperKEKB is 40 times higher than KEKB, namely, $80 \times 10^{34}\mathrm{cm}^{-2}\mathrm{s}^{-1}$. The luminosity projection of the SuperKEKB accelerator is shown in Figure 3.2. As the primary goal of the Belle II experiment, we aim to collect the integrated luminosity of 50 ab^{-1} which is 50 times larger than KEKB.

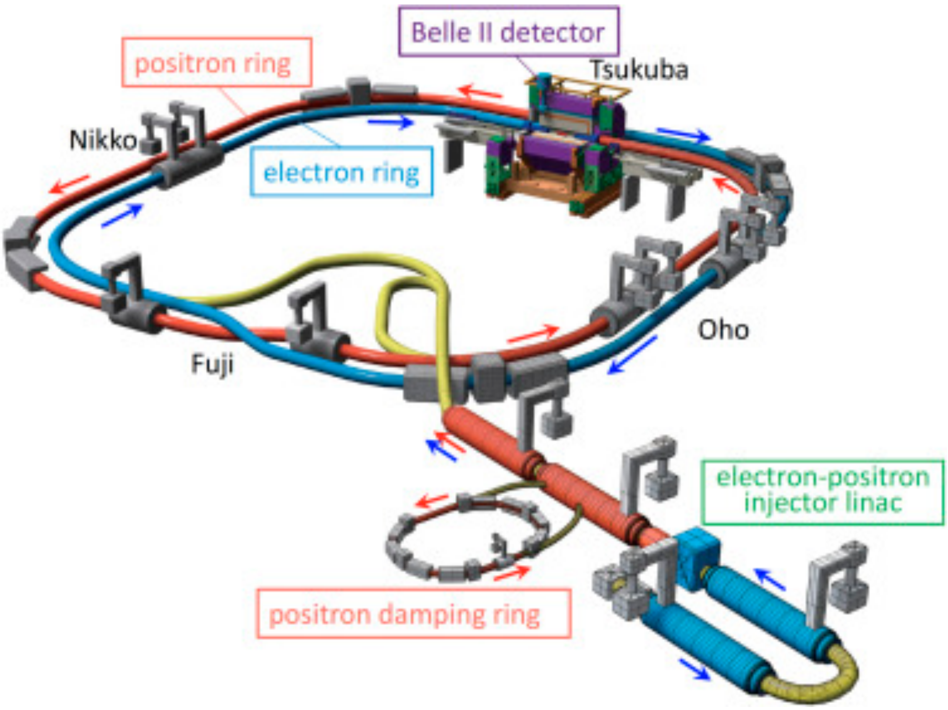

FIGURE 3.1: Schematic view of the SuperKEKB accelerator [37].

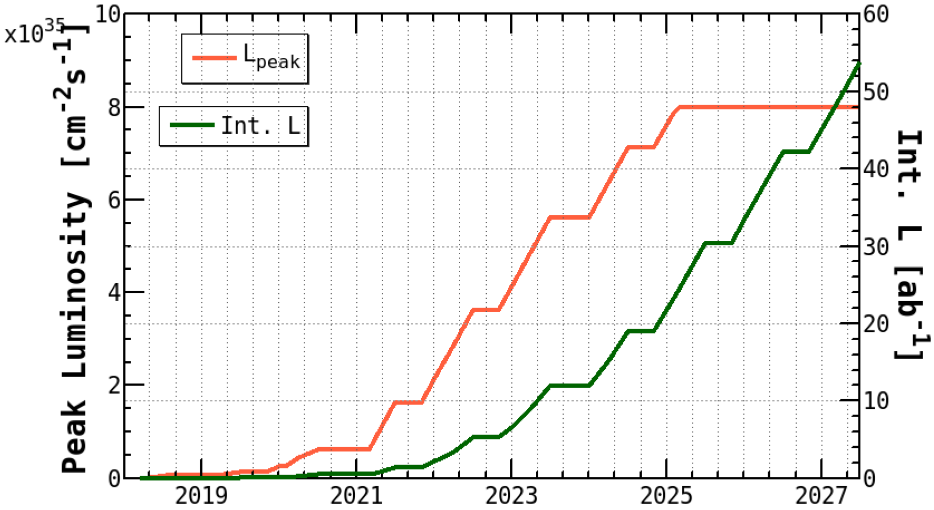

FIGURE 3.2: The luminosity projection of the SuperKEKB accelerator [38].

3.2 The Belle II spectrometer

The Belle II spectrometer is required to have the capability to take data with 40 times higher luminosity and under 10 to 20 times higher background rate [35]. The higher background rate causes an increase of number of fake hit and radiation damage. Performance of the Belle II is required to be equivalent to or better than Belle even under the higher background. The Belle II spectrometer is required to satisfy the following general requirements [39]:

- Excellent vertex resolution ($\sim 50\,\mu$m).

TABLE 3.1: The machine parameters of SuperKEKB [34] and KEK [36]

	KEKB achieved	SuperKEKB
Energy (e^+/e^-) [GeV]	3.5/8.0	4.0/7.0
Beam current (e^+/e^-) [A]	1.64/1.19	3.6/2.6
β_y^* at IP (e^+/e^-) [mm]	5.9/5.9	0.27/0.30
ξ_y (e^+/e^-)	0.129/0.09	0.088/0.081
Crossing angle [mrad]	22	83
Luminosity [10^{34}cm^{-2}s^{-1}]	2.11	80

- Good reconstruction efficiency for charged particles and photons.
- Very good momentum resolution over the whole kinematic range of the experiment (up to $\sim 8\,\mathrm{GeV/c}$).
- Precise measurements of photon energy.
- Highly efficient particle identification system to separate pions, kaons, protons, electrons, and muons over the full kinematic range of the experiment.
- Cover the almost full solid angle.
- Fast and efficient trigger system, as well as a data acquisition system.

The Belle II spectrometer has a limitation of space to fit superconducting solenoid of Belle, and it is divided into several sub-detectors. The schematic view of the Belle II spectrometer is shown in Figure 3.3. The design of each sub-detectors of the Belle II spectrometer is summarized in Table 3.2.

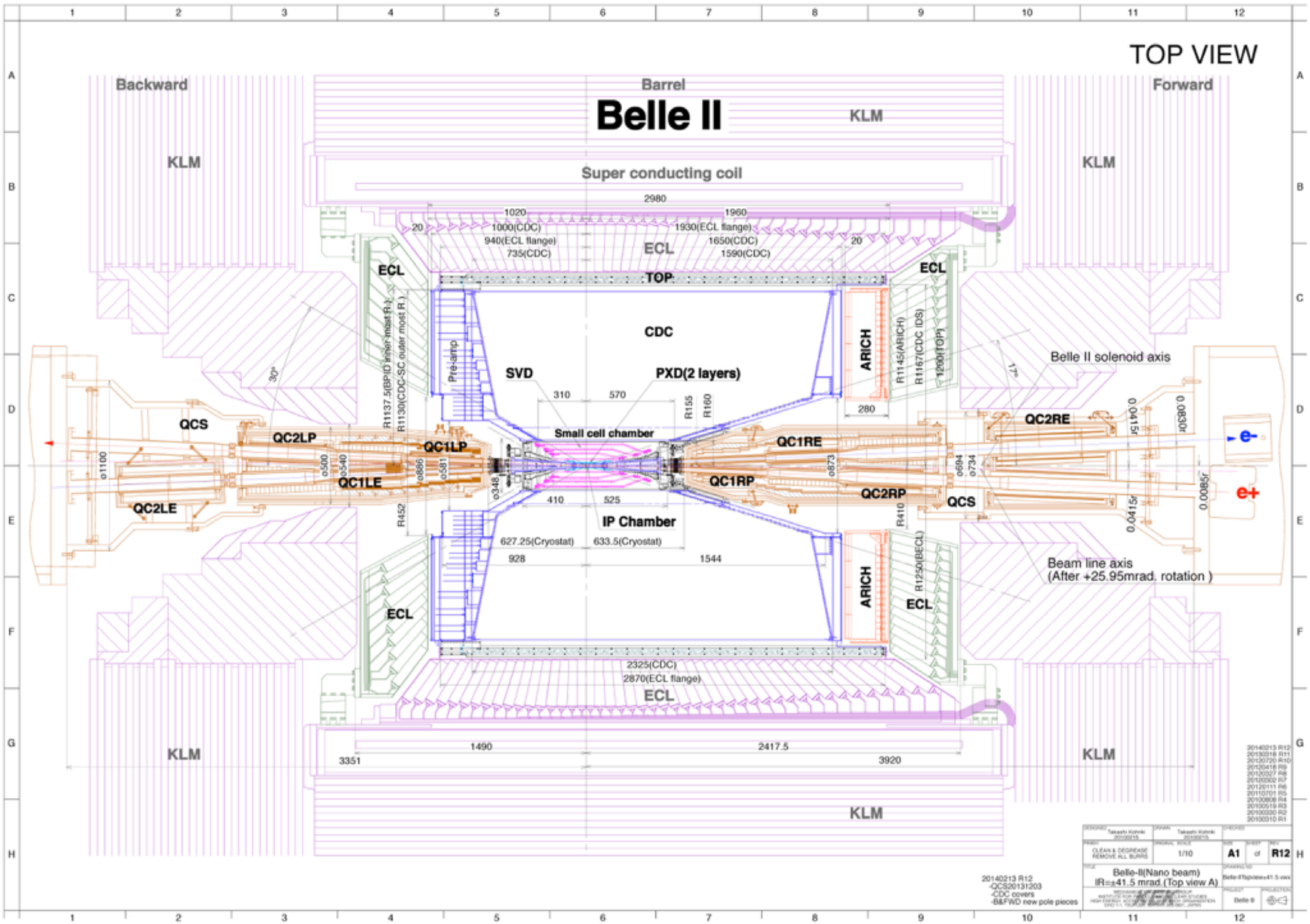

FIGURE 3.3: Horizontal sectional view of the Belle II spectrometer [40].

TABLE 3.2: Summary of the detector components; FWD and BWD stand for forward and backward end-caps [40].

Purpose	Name	Component	Configuration	Readout channel count
Beam pipe		Beryllium	Cylindrical, inner radius 10 mm, 10 µm Au, 0.6 mm Be, 1 mm paraffin, 0.4 mm Be	
Tracking	PXD	Silicon Pixel (DEPFET)	Two layers, L1 at radius 14 mm, L2 at 22 mm Sensor size by layer: 12.5 $\times$ (L1 44.8, L2 61.44) mm^2 Pixel size by layer: 50 $\times$ (L1a 55, L1b 60, L2a 70, L2b 85) µm^2	7.7 M
	SVD Silicon strip	Silicon strip (double sided)	Rectangular and trapezoidal, strip pitch: 50(p)/160(n) - 75(p)/240(n) µm, with one floating intermediate strip; four layers at radius: 39, 80, 104, 135 mm	245 k
	CDC	Drift Chamber	small cell, large cell, 56 layers	14k
Particle ID	TOP	RICH with quartz radiator (DIRC)	Barrel: 16 segments in ϕ at $r \sim 120$ cm, 275 cm long, 2 cm thick quartz bars with 4×4 channel MCP PMTs	8k
	ARICH	RICH with aerogel radiator	FWD end-cap: 2×2 cm thick focusing radiators with different n, HAPD photodetectors	60k
Calorimetry	ECL	CsI(Tl)	Barrel: $r = 125 - 162$cm End-caps: at $z = -102$ cm and $z = 196$ cm	6624 (Barrel), 1152 (FWD), 960 (BWD)
Muon ID	KLM	barrel: RPCs and scintillator strips	2 layers with scintillator strips and 13 layers with 2 RPCs	θ 16k, ϕ 16 k
	KLM	end-cap: scintillator strips	14 (12) layers of [7-10]$\times$ 40 mm^2 strips in forward (backword) region	17k

3.2.1 Vertex detector: VXD

The vertex detector is constructed from two components, Pixel Detector (PXD) and Silicon Vertex Detector (SVD), with six layers around the beam pipe (Figure 3.4). The sensor of the PXD, the inner two layers, is based on the DEPleted p-channel Field Effect Transistor (DEPFET) technology [41, 42] at $r = 14\,\mathrm{mm}$ and $r = 22\,\mathrm{mm}$. The SVD consist of four layers at $r = 39\,\mathrm{mm}$, 80 mm, 104 mm, and 135 mm, and the sensors are Double-Sided Silicon micro-strip Detectors (DSSDs). The main role of the Belle II vertex detector is to reconstruct the B-decay vertices from decay products of B-meson. The capability of vertex reconstruction is improved comparing to Belle since the outermost vertex detector layer of Belle was at a radius of 88 mm[43]. Each layer is required to have polar angle acceptance between 17° and 150°.

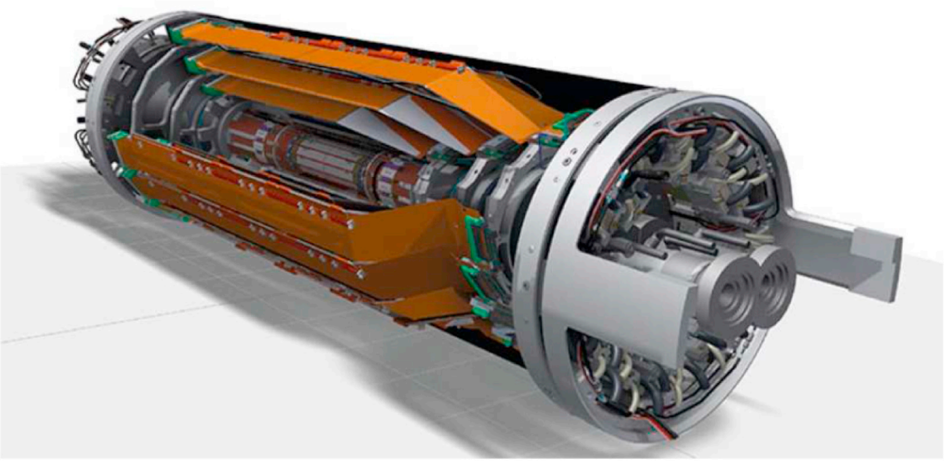

FIGURE 3.4: The picture of VXD [40].

3.2.2 Central drift chamber: CDC

The CDC is a large volume gas drift chamber with small drift cells. Compared to Belle, it extends to a larger radius from 880 mm to 1130 mm by upgrading the thinner PID device in the barrel region [40]. Besides, smaller drift cells than Belle is used to cope with high event rate with higher background level. A gas mixture is 50% helium and 50% ethane with an average drift velocity of 3.3 cm/μs.

The CDC reconstructs the tracks of charged particles to determine its momentum and provides particle identification for low momentum region using ionization energy loss in the CDC volume. Furthermore, it issues trigger information for charged particles.

3.2.3 Particle identification systems: TOP and ARICH

Two Ring Imaging Cherenkov (RICH) counters have been developed for Belle II: Time of Propagation (TOP) counter and Aerogel Ring Imaging Cherenkov (ARICH) counter. Both detectors discriminate between charged particles especially between charged pions and kaons at wide momentum range, which cannot be performed by other sub-systems.

TOP consists of 16 modules, and each module is composed of two quartz bars, a spherical mirror on one side, optical prism on the other side, and MCP (Micro-Channel Plate) PMT photon detector [44]. TOP reconstructs the ring image of the Cherenkov photons emitted in the quartz radiator by the time of arrival and detected position at MCP PMT. The TOP counter also measures the time of flight of a charged particle. Thus, TOP has required a time resolution of about 100 ps to separate the ring image of particles, and it is realized by MCP PMT.

The ARICH counter uses the angular distribution of Cherenkov photons emitted in silica aerogel radiator. The photons are detected as ring image at Hybrid Avalanche Photo Detector (HAPD). The detail of the ARICH counter is described in chapter 4.

3.2.4 Electromagnetic calorimeter: ECL

The Electromagnetic Calorimeter (ECL) is used for measuring direction and energy of γ-rays with a wide energy range, and is also used for identifying electrons from hadrons. The ECL uses 8736 crystals, thallium doped cesium iodide CsI(Tl) crystal, for the barrel, and both the end-cap region in total [45]. Belle II expects the higher backgrounds, and the overlap of pulses is increased since CsI(Tl) crystal has long decay time [40]. To cope with the pile-up of output waveforms under high background environment, sampling analysis is performed by replacing the readout electronics [46]. However, the forward region expects a much higher background, and it degrades the performance due to pile-up events even if replaced with new readout electronics. Besides, radiation damage also gets worse performance by reduction of light yield. To resolve this, replacement with faster and radiation tolerant pure CsI is under study [47]. The light yield of pure CsI is ten times smaller, and further reduction of noise from photon sensors and readout electronics is required.

3.2.5 K-long muon detector: KLM

KLM is composed of a sandwich of iron plates and detector plates. Glass-electrode resistive plate chambers (RPCs) are used for Belle KLM, but the higher background is expected for the end-cap region and innermost layers in the barrel region [40]. Belle II replaces those regions by layers of plastic scintillator strips which has a capability for the high rate.

K_L makes hadronic interactions and decays in KLM and leaves some cluster of hits. Comparing track information from CDC, KLM identifies K_L. KLM is also used to identify muons from pions. A muon can pass through KLM with a clear trail of hits overall layers while a pion stops in the middle of layers due to hadronic interactions.

3.2.6 Trigger system

The trigger system selects events of interest while rejecting a huge background. It is comprised of the level 1 (L1) trigger and the higher level trigger (HLT). Compared to Belle, the trigger system of Belle II is equipped with a new L1 trigger menu which allow us to search for new particle at the energy scale of GeV. One can analyze such interesting physics process by the new triggers of $e^+e^- \to \gamma +$ nothing or $e^+e^- \to \gamma A(A \to \gamma\gamma)$, where A represents an Axion-Like-Particle [40]. The Belle II trigger system will maintain good efficiency and low systematics for 1-prong versus 1-prong $\tau^+\tau^-$ events. The L1 trigger is required in the following items:

- high (close to 100%) efficiency (redundancy) for hadronic events from $\Upsilon(4D) \to B\bar{B}$ and $e^+e^- \to q\bar{q}$.
- high efficiency for low multiplicity physics.
- a maximum average trigger rate of 30 kHz.
- a fixed latency of about 5 µs.
- a timing precision of less than 10 ns.
- a minimum two-event separation of 200 ns.
- a trigger configuration that is flexible and robust.

3.2.7 Data acquisition (DAQ) system

The Belle II DAQ system handles readout up to 30 kHz online. The overall data flow is shown in Figure 3.5. Data from each sub-detectors except PXD are sent from electronics of sub-detectors to the Common Platform of Pipe-line Readouts (COPPERs) via Belle2Link which is the common network framework of Belle II. The PXD data is read out by ONSEN (Online Select Node) since it has a huge data size. PXD data of interest is merged to the data from other sub-detectors after HLT. The data sizes of each sub-detectors are summarized in Table 3.3.

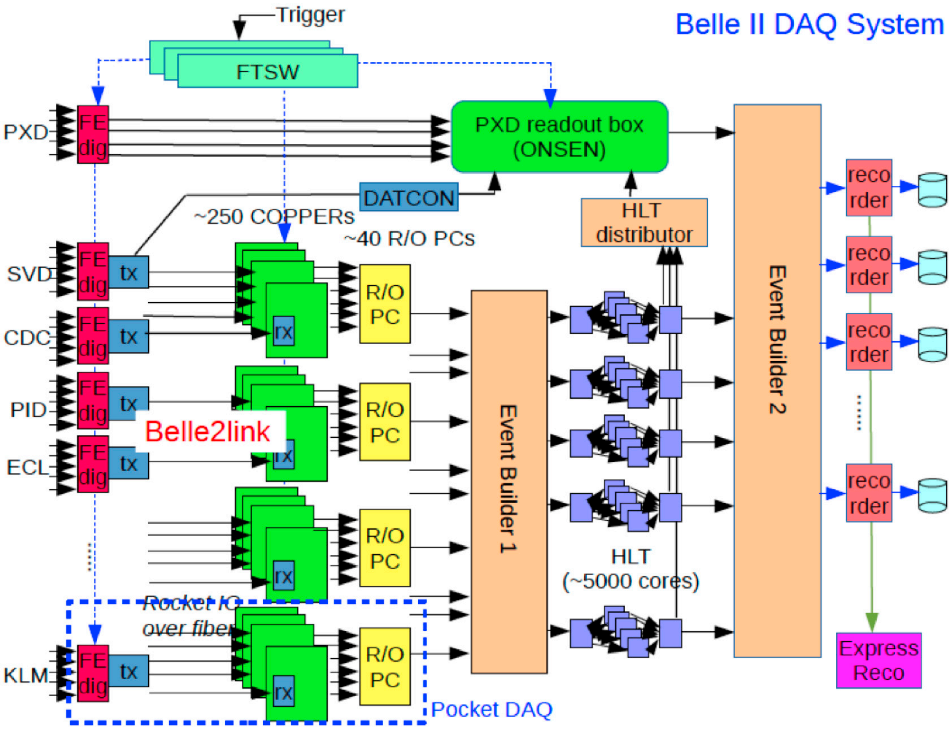

FIGURE 3.5: Data flow of the overall Belle II DAQ system [40].

TABLE 3.3: Summary of data size of each sub-detectors [35].

sub-system	# channel	Occupancy [%]	# link	/link [MB/s]	# CPR	event size [kB]	total [MB/s]	/CPR [MB/s]
PXD	8	2	40	455		800	1820	
SVD	223744	1.7 (5.5)	48	8.9(33.8)	48	14.9	428	8.9(33.8)
CDC	14336	10	302	0.6	76	6	175	2.3
TOP	8192	2.5	64	1.5	16	3.2	96	8
ARICH	60480	1.5	72	1.1	18	2.8	84	4.2
ECL	8736	33	52	7.7	26	12	360	15
B-KLM	19008	1	16	9.7	4	2	60	10
E-KLM	16800	2	16	35.8	4	1.4	42	4.7
TRG	-	-	19	-	10	-	-	-

Chapter 4

The Aerogel RICH counter

In this chapter, the principle of the RICH counter, and the design of the Belle II ARICH counter and its data acquisition and control system are described.

4.1 Cherenkov counter

4.1.1 Cherenkov light

The velocity of a massive particle can't exceed the speed of light in the vacuum. However, the speed of light in a material having refractive index $n(>1)$ is reduced to $\frac{c}{n}$, and velocity of a particle can exceed the speed of light in material. When a charged particle passes through a material, it induces the local electromagnetic field and molecules near the charged particle are polarized. The molecules are returned to the state of equilibrium after pass through the charged particle, and the electromagnetic field is released coherently. If the velocity of the charged particle does not exceed the light speed in the material, the electromagnetic field is interfered and photons are not emitted. On the contrary, the velocity of the charged particle is exceeded the light speed in the material, the electromagnetic field is amplified and photons are emitted [48, 49]. The schematic view of the Cherenkov radiation is shown in Figure 4.1.

The emission angle of the Cherenkov photons is defined as

$$\cos\theta_C = \frac{\frac{c}{n}\Delta t}{v\Delta t} = \frac{1}{n\beta}, \tag{4.1}$$

where θ_C is an emission angle of Cherenkov photon, n is refractive index of the material and β is ratio of velocity of the charged particle and light speed. Here, β can be expressed as

$$\beta = \frac{p}{E} = \frac{p}{\sqrt{(m)^2 + p^2}}, \tag{4.2}$$

where p is momentum, E is energy and m is mass of particle. Therefore, Equation 4.1 can be rephrased by Equation 4.2 as

$$\cos\theta_C = \frac{\sqrt{(m/p)^2 + 1}}{n}. \tag{4.3}$$

The threshold momentum $p_{th}$of the particle is

$$p_{th} = \frac{m}{\sqrt{n^2 - 1}}.. \tag{4.4}$$

The threshold momentum with refractive index in the range of 1.0 to 1.5 for the electron, muon, pion, kaon, and proton are shown in Figure 4.2. The region above the line satisfy the condition of Cherenkov radiation.

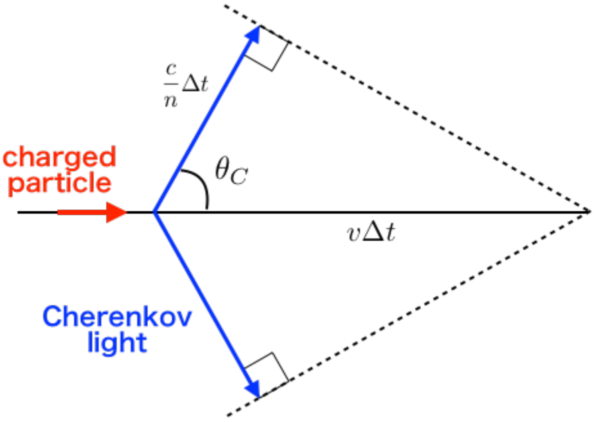

FIGURE 4.1: The schematic view of the Cherenkov photon.

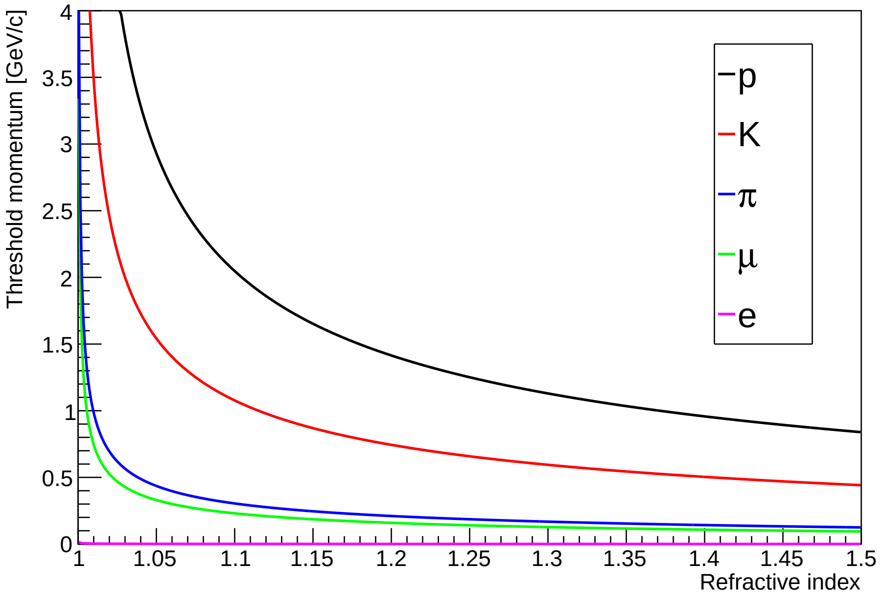

FIGURE 4.2: The relation between the momentum of the particle and refractive index.

4.1.2 PID at Belle

The particle identification (PID) at Belle was performed by Aerogel Cherenkov counter (ACC) which is a threshold type PID device [50]. Equation 4.4 indicates that the threshold momentum of Cherenkov radiation differs according to the mass of particles. At the Belle experiment, the refractive index is arranged by the polar angle from the interaction point as shown in Figure 4.3. The threshold momentum to emit the Cherenkov photons for pions and kaons versus the refractive index in the range of 1.0 to 1.05 is shown in Figure 4.4. The end-cap region uses 1.030

as a refractive index since the PID at the end-cap region does not have TOF counter, and ACC is required to cover low momentum region where the dE/dx from CDC does not work Therefore, the momentum region that is capable to identify a particle is limited to be below 2.0 GeV/c. The overall performance of charged particle identification had enough performance at the Belle experiment [51]. If we focused on the performance of the forward end-cap ACC only, the distribution of K efficiency and π fake rate is shown in Figure 4.5 [52]. A drop of K efficiency at 2.0 GeV is clearly seen.

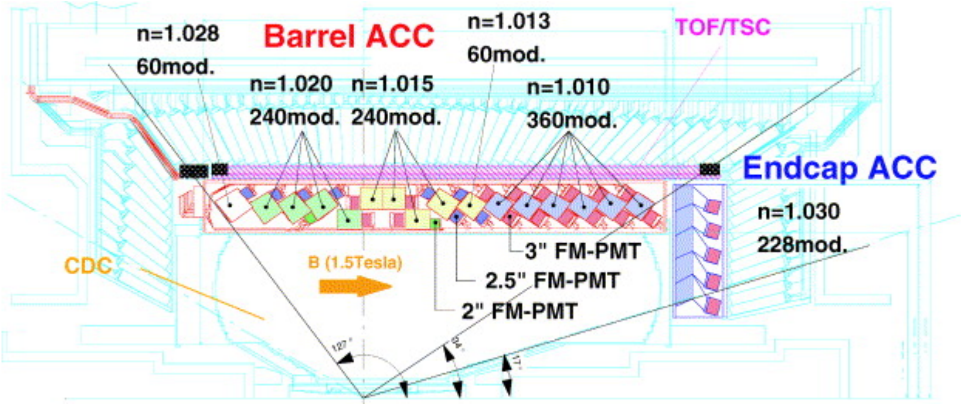

FIGURE 4.3: The arrangement of the ACC at Belle [19].

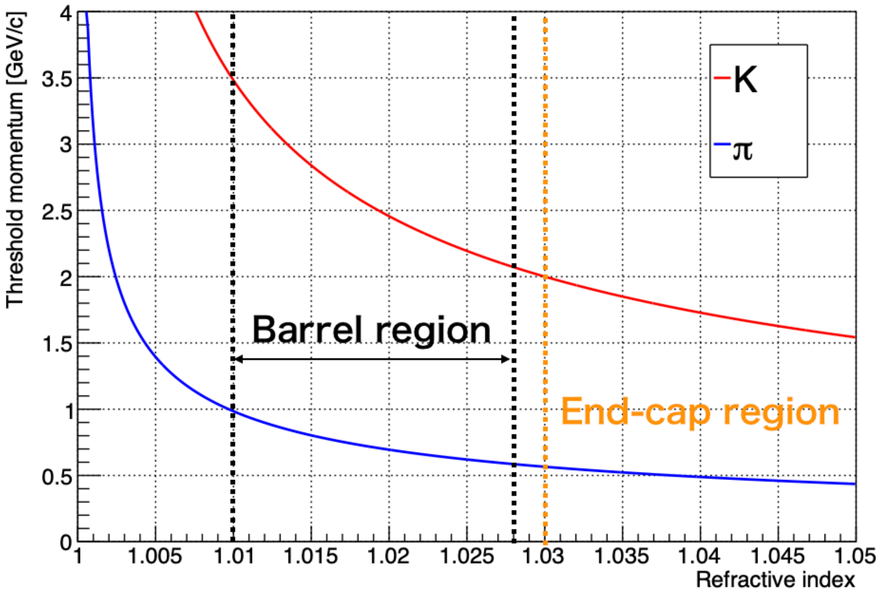

FIGURE 4.4: The threshold momentum to emit Cherenkov photon for the range of the ACC at Belle.

4.1.3 Requirement for end-cap PID for Belle II

In the Belle II experiment, identification of charged particles with higher momenta up to 4 GeV/c is required to search for new physics in the processes such as $B \to \rho(\to \pi\pi)\gamma$ and $B \to K^{*}(\to$

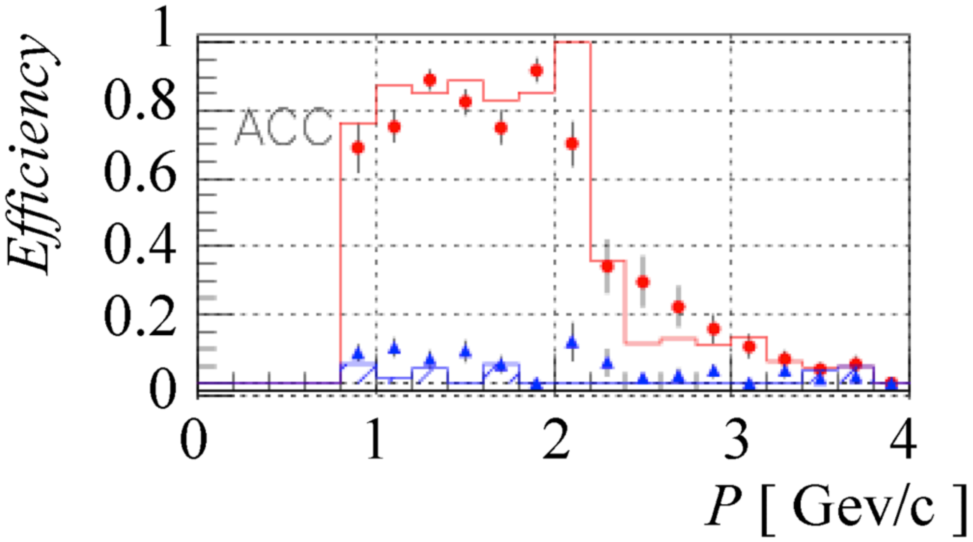

FIGURE 4.5: K efficiency and π fake rate in the forward end-cap region at Belle as a function of momenta.

$K\pi)\gamma$ [53–55]. From the simulation study of such physics modes, Belle II aims to identify kaons and pions with 4σ separation, which roughly corresponds to an efficiency to be well above 90 % and a misidentification probability to be well below 10 %. Including this requirement, following items are required for the end-cap PID device of Belle II:

- Constructed in the limited scape
- Charged K/π separation of $4\,\sigma$ level up to $4\,\mathrm{GeV}/c$
- Readout to be tolerable up to 30 kHz
- Radiation hardness throughout the 10 years operation of Belle II

To fulfill those requirements, the proximity focusing RICH counter called the Aerogel RICH (ARICH) counter is newly developed for Belle II.

4.2 Principle of Belle II ARICH

The principle of the particle identification of ARICH is shown in Figure 4.6. ARICH uses Cherenkov photons emitted in the radiator when the particle velocity exceeds light speed in the radiator. Emitted photons are detected by the photon detector and the emission angles of Cherenkov photons are measured. The following equation indicates the relation between the emission angle of Cherenkov photon and the particle mass.

$$\cos\theta = \frac{\sqrt{(m/p)^2 + 1}}{n}, \tag{4.5}$$

where θ is an emission angle of Cherenkov photon, m is a mass of the particle, p is a momentum of the particle and n is the refractive index of the silica aerogel. The momentum of the particle is measured by CDC, and the refractive index is a known value here based on our design. Therefore, the mass of the particle can be identified by measuring the angle of Cherenkov photons.

The distribution of the emission angle of Cherenkov photons with a refractive index of 1.5 as a function of the momentum in the range from 0.0 GeV/c to 4.0 GeV/c is shown in Figure 4.7. The Cherenkov angles for pion and kaon are 308 mrad and 285 mrad at 4 GeV/c, respectively. The difference in the Cherenkov angle between pion and kaon is 23 mrad.

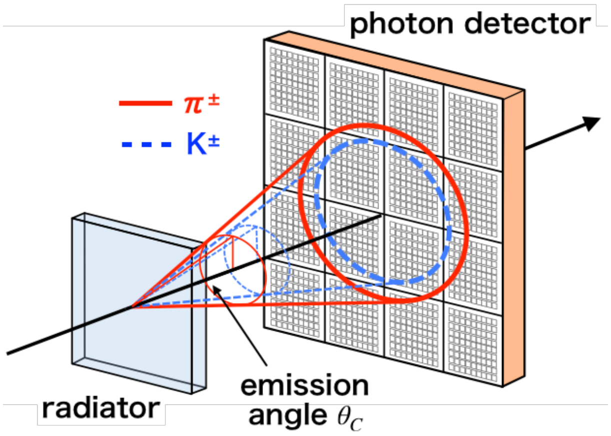

FIGURE 4.6: The principle of the particle identification of the ARICH counter.

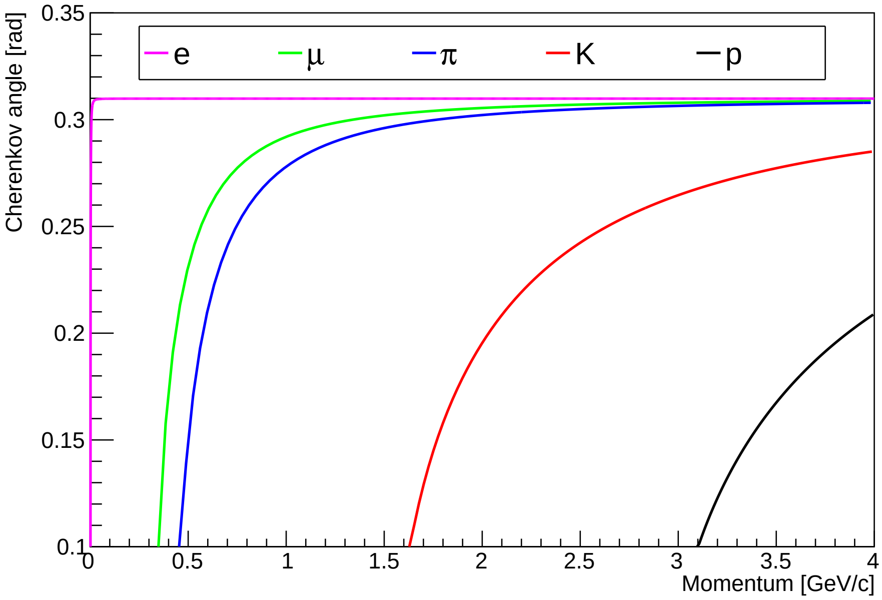

FIGURE 4.7: Cherenkov angle as a function of momentum with refractive index of $n = 1.5$

4.3 Design of Belle II ARICH

The ARICH counter is comprised of three main components: the silica aerogel radiators, the HAPDs, and the readout electronics. All three components were newly developed for the Belle

TABLE 4.1: The refractive indices of major material.

Material	Refractive index
air	1.0003
carbon dioxide	1.0004
silica aerogel	1.003 – 1.26
water	1.33
quartz	1.5

II ARICH counter. Details are described in the following sections.

The shape of ARICH is a rectangular toroid with an outside radius of 1140 mm, an inside radius of 420 mm, and a length of 280 mm. Figure 4.8 shows the arrangement of the components of ARICH along the beamline. The components along the beamline are a 40 mm thick radiator, an expansion space of 160 mm, a 50 mm thick photon detector, and a 30 mm thick readout electronics.

Figure 4.9 shows the schematic view of the structure of ARICH. The silica aerogel radiator is comprised of 124 pairs of wedge-shaped tiles arranged in four concentric rings with 22, 28, 34, and 40 pairs. The HAPDs are arranged in seven concentric rings with 42, 48, 54, 60, 66, 72, and 78 detectors, 420 HAPDs in total.

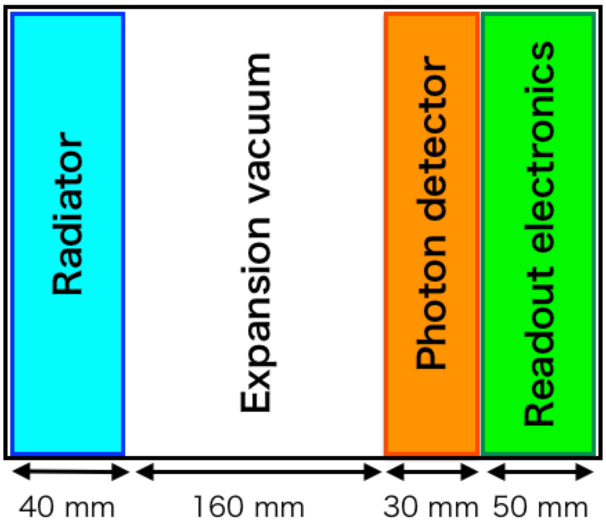

FIGURE 4.8: The arrangement of the components of ARICH.

4.3.1 The radiator

The radiator is required to have large transmission length and suitable refractive index. The refractive index is required to make the ring radius to be a few decimeters, emitting enough the number of photons, and avoiding total reflection at the boundary between radiator and air. The range of refractive index which fulfills the above requirement is 1.01–1.1. The refractive indices of typical materials are summarized in Table 4.1.

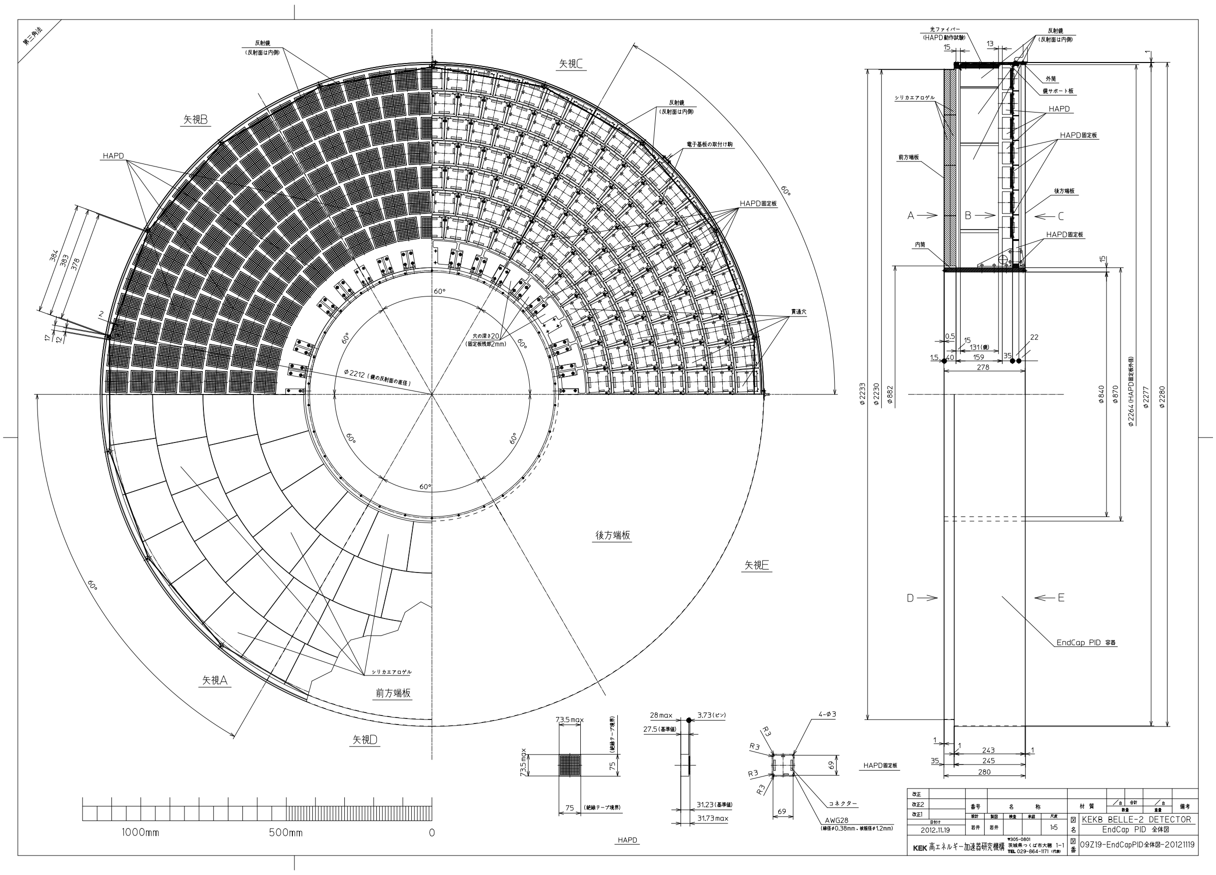

FIGURE 4.9: The schematic view of the structure of ARICH.

The silica aerogel can satisfy the refractive index between 1.003–1.26, and one can control the value of the refractive index at its production [56]. Therefore, the silica aerogel is the most suitable material of the radiator of ARICH.

The choice of the refractive index of silica aerogel has to be made with taking both the number of emitted Cherenkov photons and transmission length into account. The number of emitted Cherenkov photons N_{ph} with a wavelength λ is expressed as follows [57]:

$$\frac{d^2N_{\mathrm{ph}}}{d\lambda dx} = \frac{2\pi\alpha z^2}{\lambda^2}(1 - \frac{1}{\beta^2(n(\lambda))^2}) = \frac{2\pi\alpha z^2}{\lambda^2}\sin^2\theta_C(\lambda), \tag{4.6}$$

where α is the fine structure constant, λ is the wavelength of the photon, z is a charge of the incident particle, $n(\lambda)$ is the refractive index for given wavelength of the photon. A larger refractive index can make larger Cherenkov angle and produce more Cherenkov photons.

In general, transmission decreases in proportion to the refractive index. The low transmission length causes loss of the emitted photons, and larger transmission length is required. The dependence of transmission length on the refractive index is shown in Figure 4.10. The transmission length is found to be maximum at around the refractive index of 1.03, and the transmission length is still sufficiently high (>20 mm) at the refractive index of 1.05. Therefore, ARICH chooses 1.05 as a refractive index of the radiator.

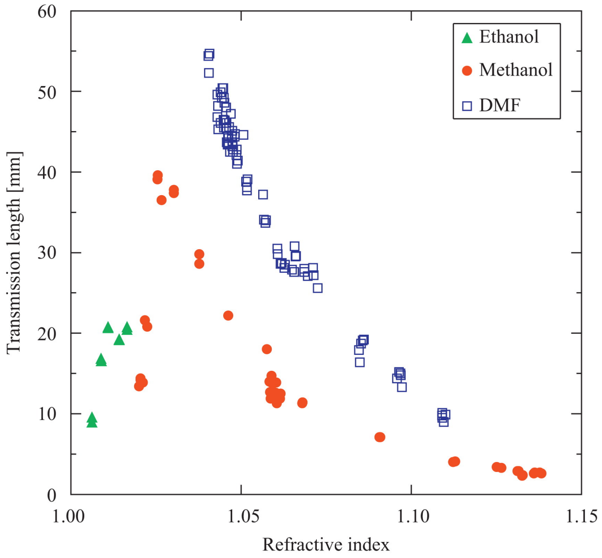

FIGURE 4.10: Transmission length as a function of refractive indices at 400 nm of injected photons [58].

One of the important parameters of the ARICH performance is the Cherenkov angle resolution of a track σ_{track}, and it is defined as

$$\sigma_{\text{track}} = \frac{\sigma_\theta}{\sqrt{N_{\text{p.e.}}}}, \tag{4.7}$$

where σ_θ is the Cherenkov angle resolution, and $N_{\text{p.e.}}$ is the number of detected photons. The number of detected photons can be increased with thickness, however, the resolution of Cherenkov angle distribution is also deteriorated with the thickness because of the increase of the uncertainty of the emission point. The dependence of σ_{track} as a function of thickness is shown in Figure 4.13. The optimum thickness is found to be 20 mm.

A dual-layer scheme is adopted to improve angle resolution without reducing the number of detected Cherenkov photons [59–61]. By optimizing the two different refractive indices, Cherenkov photons are projected on the photon detector plane squeezed to a smaller ring image as shown in Figure 4.12. We choose refractive indices of 1.045 and 1.055 for the upstream and the downstream aerogel tile, respectively. The threshold momentums to emit the Cherenkov photons are 0.44 GeV/c for pions and 1.54 GeV/c for kaons with a refractive index of 1.05.

The ARICH counter uses large-area silica aerogel tiles with a long transmission length [62–64]. The picture of the aerogel tile is shown in Figure 4.11. The refractive indices and transmission lengths of produced silica aerogel tiles are summarized in Table 4.2. The difference of refractive indices between the upstream and the downstream has to be matched to maximize the overlapping of the ring image. The difference of refractive indices in installed tile pairs is between 0.0095 and 0.0104, while our requirement range is between 0.008 and 0.012.

4.3.2 Photon detector

Photon detector of ARICH is required to have following conditions;

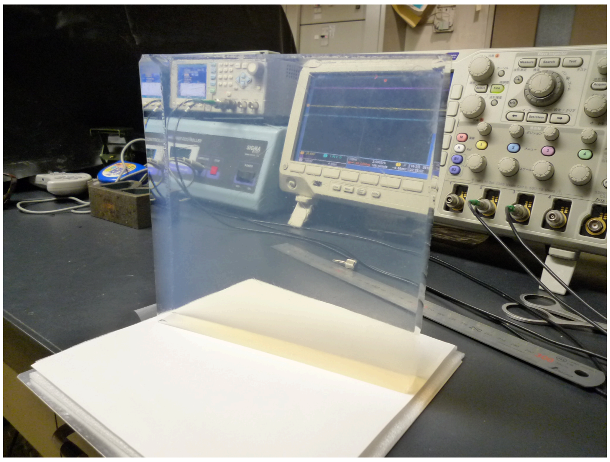

FIGURE 4.11: The picture of aerogel tile.

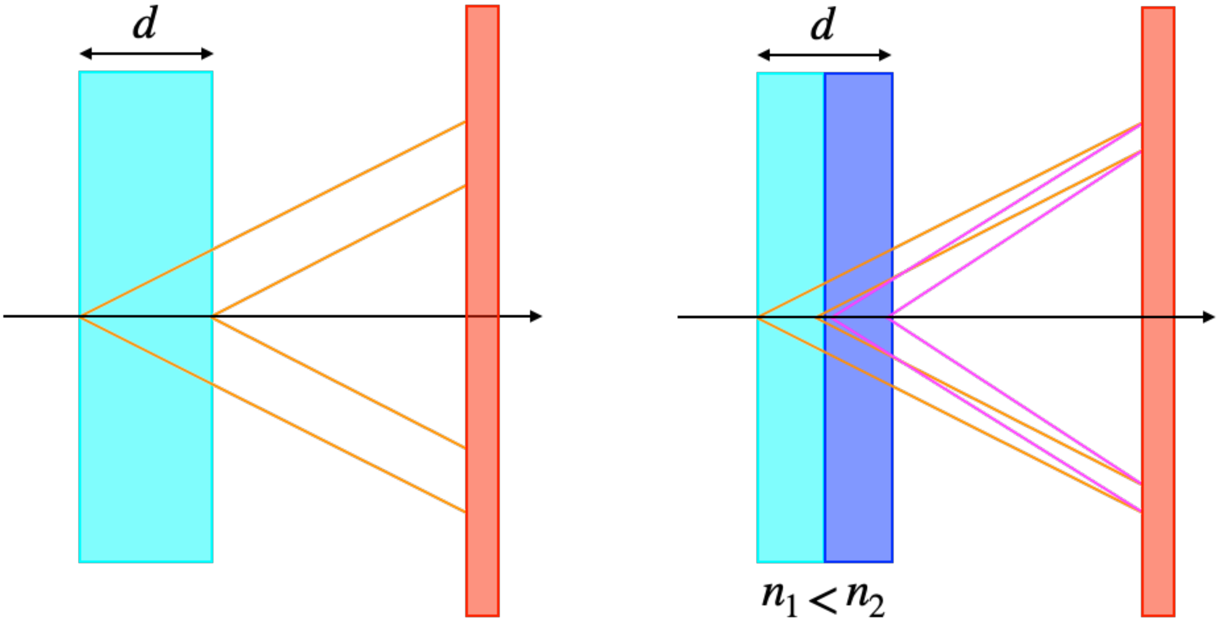

(a) single layer scheme

(b) dual layer scheme

FIGURE 4.12: The conceptual diagram of the radiator design. (a) single layer scheme and (b) dual layer scheme.

- capable of single photon detection with high position resolution to be less than 5 mm
- operational in the high magnetic field ($B = 1.5$ T)
- the radiation hardness throughout the 10 years operation of Belle II

The HAPD which has been developed with Hamamatsu Photonics K.K. fulfills our requirements as a photon detector [65–67]. The specification of the HAPD is summarized in Table 4.3. An HAPD is composed of a quartz window with a photo-cathode, a vacuum tube, and four Avalanche Photo Diode (APD) chips. The mechanical structure of HAPD is shown in Figure 4.14. Each APD chip has 6×6 pixels of an area of $4.9 \times 4.9\,\mathrm{mm}^2$, and an HAPD has 144 channels in total. The photon detection of the HAPD is realized by two mechanisms: bombardment of a

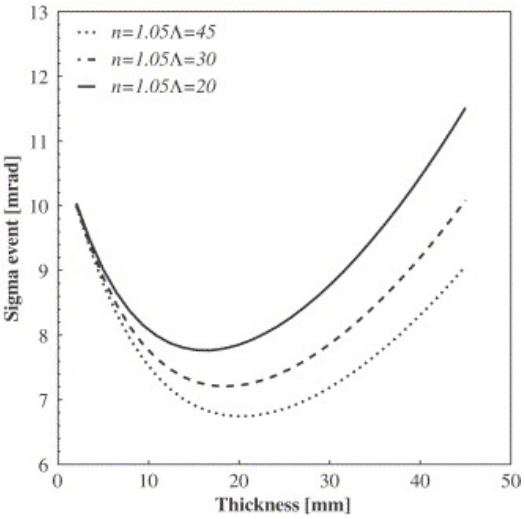

FIGURE 4.13: The resolution of the Cherenkov angle distribution as a function of thickness of aerogel tiles [59].

TABLE 4.2: The refractive indices and transmission lengths of produced silica aerogel tiles.

Target refractive index	1.045	1.055
Refractive index	1.0451 ± 0.0007	1.0547 ± 0.0007
Transmission length at 400 nm	47.3 ± 3.1mm	36.0 ± 2.7mm

photo-electron (Figure 4.14-(a)) and avalanche amplification in the APD chip (Figure 4.14-(a)). The photo-electrons are accelerated in the high electric field by applying a negative high voltage, and it produces about 1800 electron-hole pairs in the APD. The electrons produce about 40 electron-hole pairs in the depletion region by applying a reverse bias voltage. As a result, the total gain of the HAPD is about 72000. Three kinds of power supply are needed to control an HAPD: a negative high voltage for photo-electron acceleration (HV×1: $-7$to $- 8$kV), reverse bias voltages for each APD (Bias×4: around 350 V), and a guard voltage common to APD (Guard×1: 175 V). Therefore, six power supply inputs are required to control an HAPD.

Figure 4.15 shows one to two-dimensional distribution of the average quantum efficiency at 400 nm of all the installed HAPDs. The mean value of the quantum efficiency of the installed HAPDs is 32.2%. They are distributed randomly on the photon detector plane to minimize the position dependence of detection efficiency for the Cherenkov light. The performance of HAPDs in the Belle II operation is described in section 5.2

4.3.3 Readout electronics

Readout electronics consist of Front End Boards (FEBs) and Merger Boards (MBs) [68, 69]. The pictures of the FEB and the MB are shown in Figure 4.16 and Figure 4.17. The FEB is directly attached to an HAPD and has four Application Specific Integrated Circuit (ASIC) chips which are called SA03 [70]. An ASIC chip (SA03) amplifies, shapes, and discriminates 36 signals coming

TABLE 4.3: The specification of the HAPD.

Size	$73 \times 73 \times 28\,\mathrm{mm}^3$
Number of APD chips	$2 \times 2 = 4$ chips
Number of channels	$12 \times 12 = 144$ ch
Channel size	$4.9 \times 4.9\mathrm{mm}^2$
Effective area	65 %
Photo-cathode material	Bialkali
Quantum efficiency	$\sim$28% at 400 nm
Bombardment gain	$\sim$1800
Avalanche gain	$\sim$40
Total gain	72000
Capacitance	80 pF

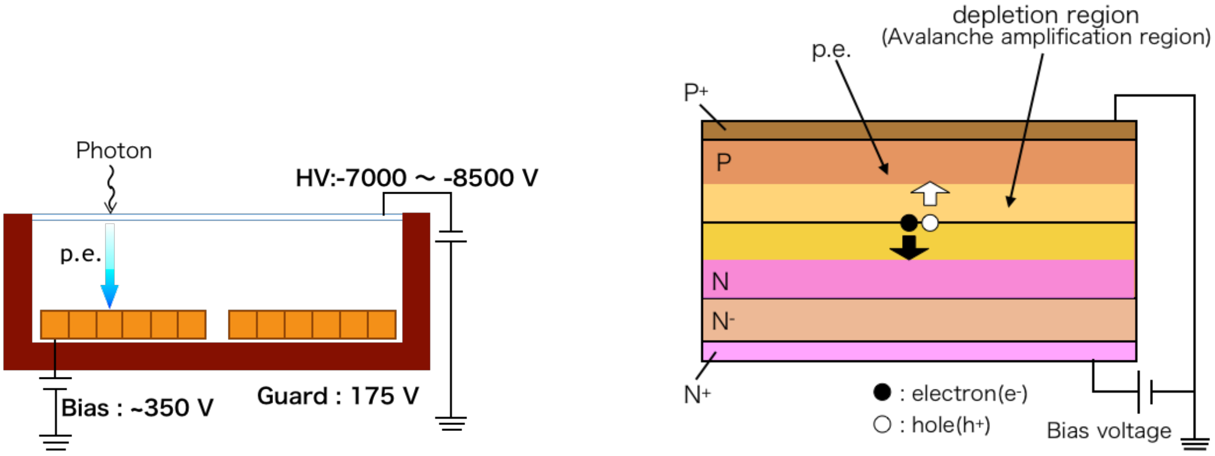

(a) Overall structure of HAPD

(b) APD structure

FIGURE 4.14: The mechanical structure of HAPD. (a) overall structure of HAPD and (b) APD structure in HAPD.

from a quarter of an HAPD as shown in Figure 4.18. ARICH measures the ring image and we collect only hit information. Up to six FEBs are connected to one MB, and a MB serializes the data from FEBs and suppresses the data of no-hit channels to reduce the data size. Then, the MB sends merged data to the back-end Belle II central data acquisition system. The data flow in the ARICH readout electronics is shown in Figure 4.19.

Each MB has two RJ45 connections for trigger and Joint Test Action Group (JTAG), and an optical fiber connector for data acquisition and configuration of the FEBs that are set via the MBs. Both FEBs and MBs employ a field programmable gate array (FPGA) which is responsible for communication between the boards and back-end data acquisition electronics. Spartan-6 and Vertex-5 are used for the FEB and the MB, respectively. We use 420 FEBs and 72 MBs, and handle 60480 channels in total.

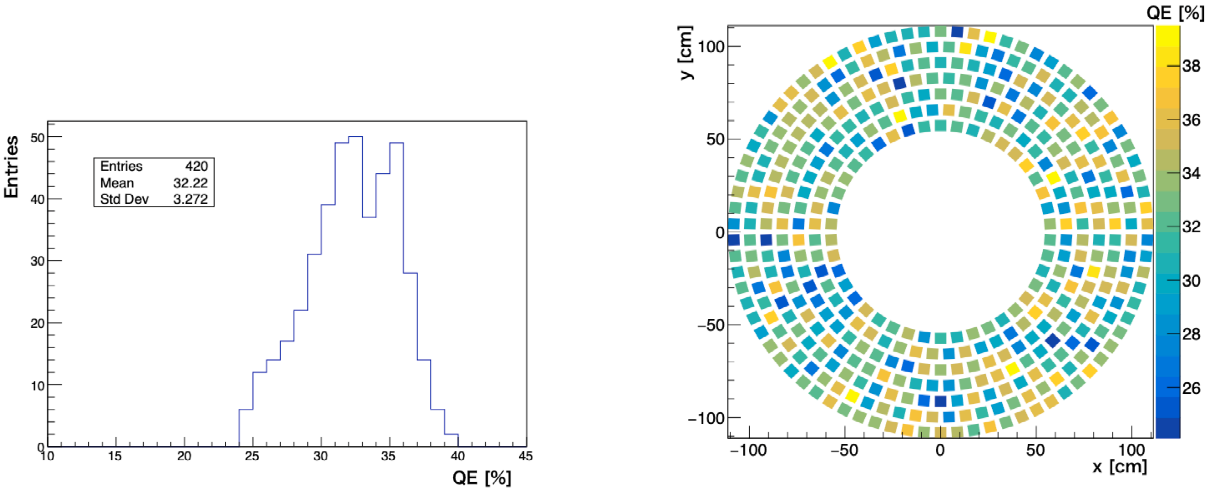

(a) One-dimensional distribution

(b) Two-dimensional distribution

FIGURE 4.15: One (a) or two (b) dimensional distribution of quantum efficiency of installed HAPDs. The quantum efficiency for each HAPD is arranged over the photo sensitive area.

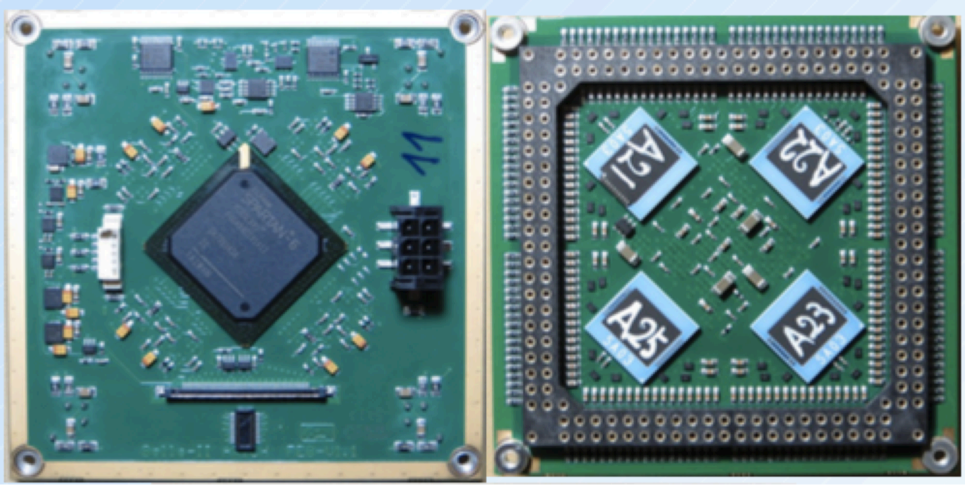

FIGURE 4.16: The picture of Front End Board.

4.4 Control systems

4.4.1 Development of the high voltage power supply system

Six power supply inputs are required to control an HAPD. As we use 420 HAPDs for Belle II ARICH, high voltage power supply system of ARICH is required to have the capability to handle 2520 power supply inputs. In addition, the following functionalities are required: sequential operation of three kinds of voltages, interface to a network to other Belle II subsystems, a database containing the configuration, and graphical user interface (GUI). I have developed power supply system including control software for ARICH.

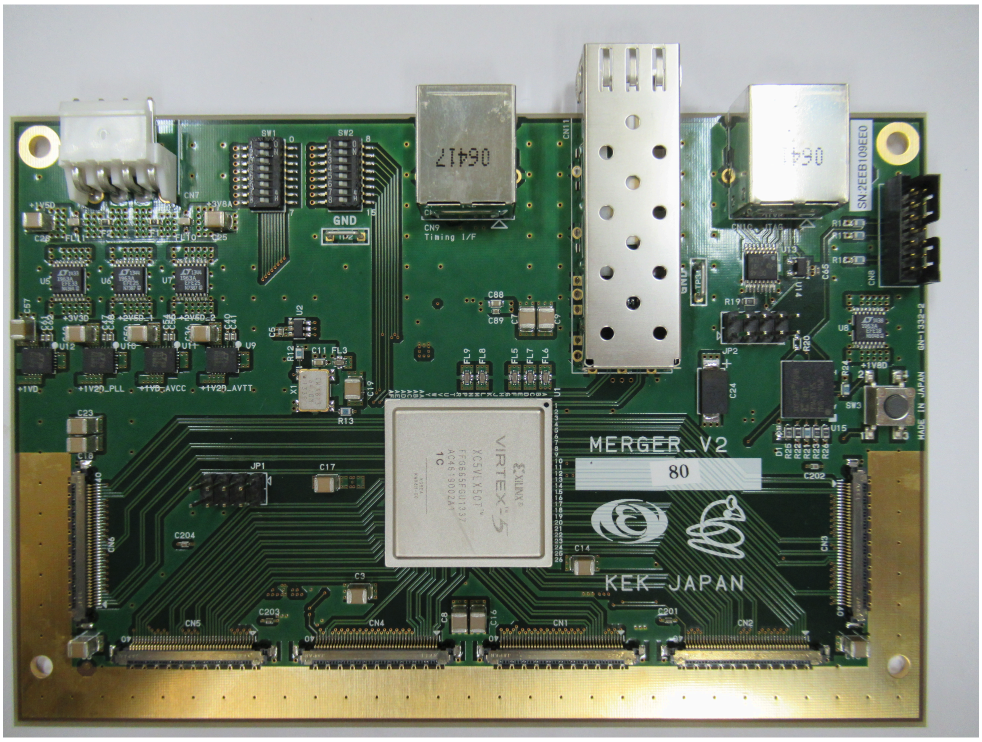

FIGURE 4.17: The picture of Merger Board.

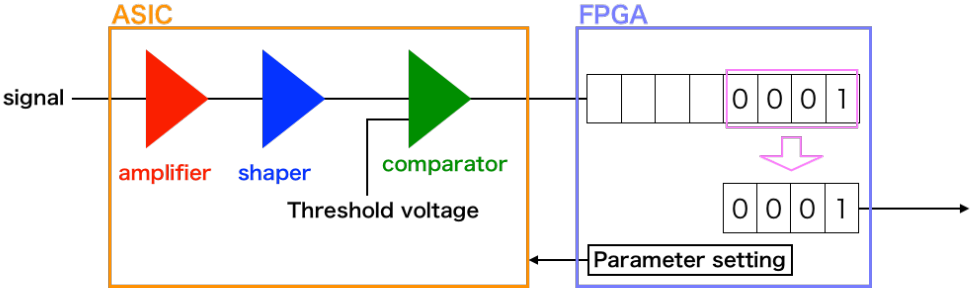

FIGURE 4.18: Data flow in Front End Board.

Development of the power supply

Requirements for high voltage power supply are shown in Table 4.4. We divide a HV into two voltages using registers: one is applied to the photo-cathode of the HAPD and the other is applied to the inner ring of the HAPD. The latter one is applied because we found some flash over events under high magnetic field environment, and we also fond that suppling around a half of HV will reduce such events by stabilizing the electric field in the vacuum tube of the HAPD and by getting rid of charges collected at the middle ring [67]. The candidate of the minimum register is two $1\,\mathrm{G\Omega}$ registers in serial, thus maximum current is $9 \times 10^3/2 \times 10^9 = 4.5\,\mu\mathrm{A}$. Requiring factor 10 margin, $45\,\mu\mathrm{A}$ or more is required as maximum current for HV. The currents of bias may increase due to the increase of leakage current of APD that is mainly caused by neutron irradiation. To check the radiation hardness of HAPDs, we perform a neutron irradiation test at the neutron beam line (BL10) of J-PARK MLF.[53, 54] After the irradiation test that correspond to the 10 years operation of the Belle II experiment, the typical maximum

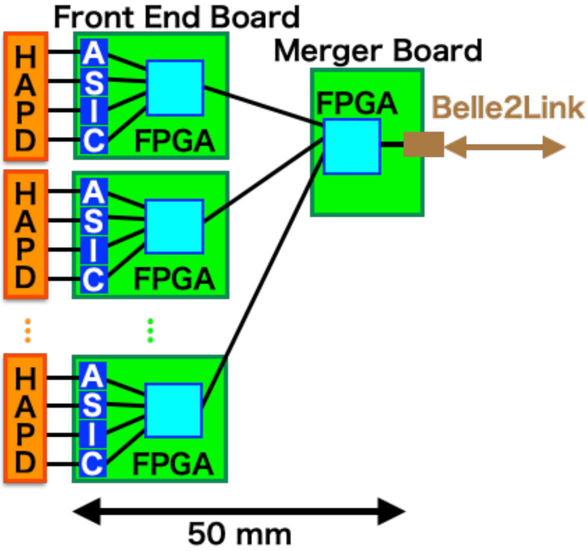

FIGURE 4.19: Data flow in ARICH readout electronics.

TABLE 4.4: Requirement of high voltage power supply

items	HV	Bias	Guard
Maximum output voltage	$-9000\,\mathrm{V}$	$500\,\mathrm{V}$	$250\,\mathrm{V}$
Maximum output current	$45\,\mu\mathrm{A}$	$500\,\mu\mathrm{A}$	$50\,\mu\mathrm{A}$
Precision of setting voltage	0.3 %	0.3 %	0.3 %
Ripple voltage	$250\,\mathrm{mV}(\mathrm{p}-\mathrm{p})$	$30\,\mathrm{mV}(\mathrm{p}-\mathrm{p})$	$30\,\mathrm{mV}(\mathrm{p}-\mathrm{p})$
Stability	500 ppm/H	100 ppm/H	100 ppm/H
Temperature dependency	500 ppm/°C	100 ppm/°C	100 ppm/°C
Offset voltage	$<5\,\mathrm{V}$	$0.2\,\mathrm{V}$	$0.2\,\mathrm{V}$

leakage current of bias is $36\,\mu\mathrm{A}$. Requiring factor 10 margin, $360\,\mu\mathrm{A}$ or more is required as maximum current for bias. The stability of output voltage is required to be kept so that the variation of gain to be less than 1 %. The average gradient of the gain measured with randomly selected samples for HV at around $-8.5\,\mathrm{kV}$ is 310 /kV. As a result, the change of voltage that corresponds to 1 % gain change is 0.7 %. Requiring a factor 10 margin, 700 ppm or better is required as stability for HV. For bias, 130 ppm or better is required as stability.

We have tested a prototype power supply from CAEN [71]. The specification of the power supply is shown in Table 4.5. We found issues in the trip function and the interlock function. The trip function and the interlock function are safety functions to protect devices from abnormally applied voltages. The trip function suspends applying voltage if the monitored voltage or current exceeds a threshold voltage or current. For the Bias-Guard module, we found the voltage unexpectedly continues to increase even it exceeds the threshold voltage. The interlock function suspends applying voltage when the NIM signal is input. After interlock is executed, those channels cannot be turned on until receiving a clear signal. However, for the HV module, an interlocked channel can be turned on before receiving a clear signal. Both issues are fed back to CAEN and are fixed by improving CAEN's firmware and the hardware update.

TABLE 4.5: Specification of CAEN HV power supply module.

	HV	Bias-Guard
Model number	A1590	A7042P
Maximum output voltage	$-9000\,\mathrm{V}$	$500\,\mathrm{V}$
Maximum output current	$50\,\mu\mathrm{A}$	$500\,\mu\mathrm{A}$
Used number of slots	2	1
Number of channels	16	48
Number of modules	28	45

Finally, we evaluate the stability by applying a voltage to the HAPD. The results of the stability of two weeks are shown in Figure 4.21. All voltages fulfilled the requirement of stability. We finally conclude those power supplies are capable of operating Belle II ARICH, and we adopt those power supplies for Belle II ARICH.

Development of the control software

The control software of ARICH high voltage has been developed together with power supply. The conceptual image of ARICH high voltage control system is shown in Figure 4.21. The "ARICH HV control software" is the main program to manage power supplies of the HAPDs [72, 73]. The PC for running the program has two network connections; one is going to the power supply and the other is going to the Belle II global network. The communication between the PC and the power supply is implemented using a CAEN HV Wrapper which packs communication protocol to the crate devices into TCP. Thus, the program gets (sets) the parameters from (to) power supply such as demanding voltage, voltage or current limit, and monitored value and so on. The communication is based on the Belle II DAQ software framework, and it realizes us to access to the real time information of any other systems in the Belle II DAQ network such as accelerator and the run control system. Hence, we can protect photon sensors from accidental incidence such as a magnet quench, and we perform an effective operation and keep a good quality of data. Parameters for power supply such as setting voltages are stored into a relational database of PostgresSQL [74], and the interface is also implemented in the Belle II DAQ software library.

We also developed a graphical user interface (GUI) using Control System Studio [75] which based on an integrated development environment of eclipse [76]. The GUI of ARICH high voltage control system is shown in Figure 4.22. It has functions to control several parameters such as demanding voltage, the speed of ramping up and down, and voltage and current limit for individual channels. In addition, the integrated operation is also implemented for the transition of all the channels to the nominal voltage or turned off state or intermediate voltage[1].

4.4.2 Monitor system

The performance of photon detection directly affects that of particle identification of ARICH. To monitor the performance of photon detection by HAPDs during the physics data taking at the

---

[1] During beam injection, the background become high and photon sensors may be damaged. Lower voltage protects photon sensors while suppressing the ramp-up time after the injection.

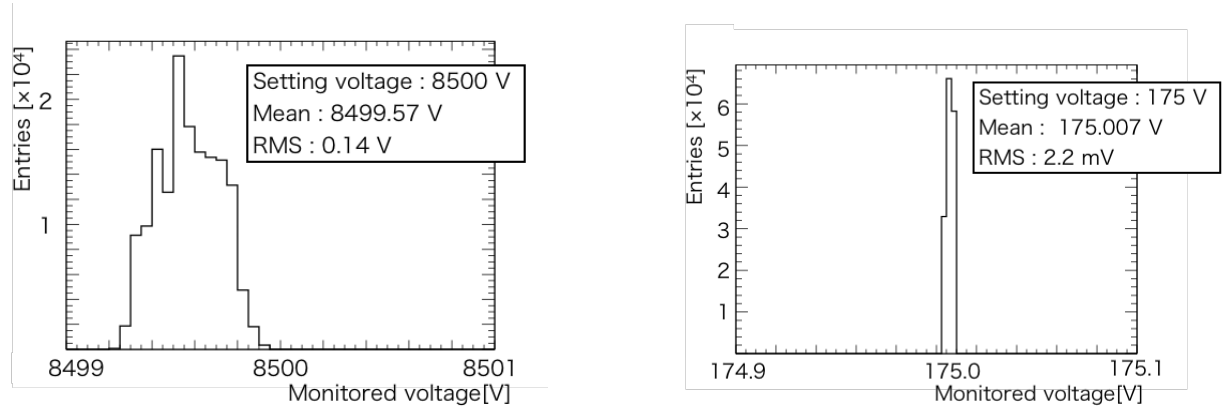

(a) HV (b) Guard

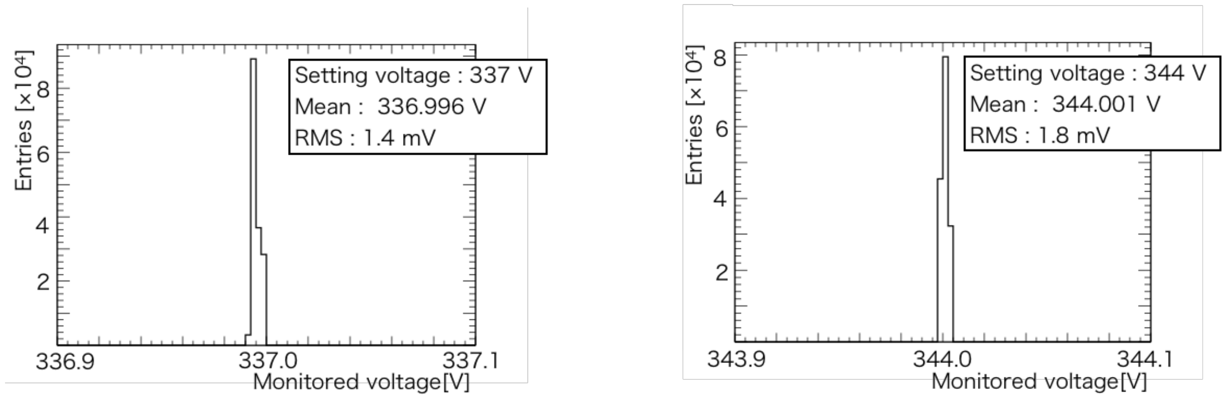

(c) Bias-A (d) Bias-B

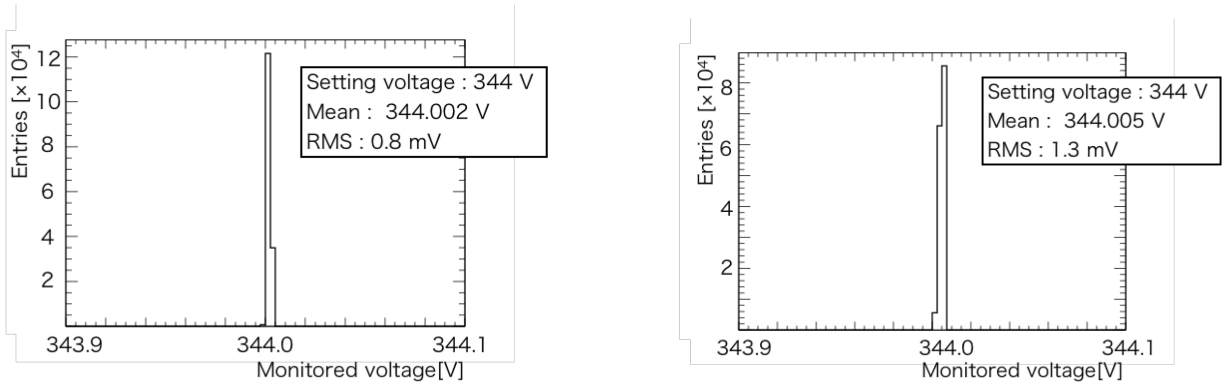

(e) Bias-C (f) Bias-D

FIGURE 4.20: The distributions of monitored voltage for two weeks. (a) HV, (b) Guard, (c) Bias-A, (d) Bias-B, (e) Bias-C and (f) Bias-D.

Belle II experiment, the LED-based monitor system is installed [77].

The conceptual image of the monitor system is shown in Figure 4.23. The LED light is used to examine the performance of the HAPDs. LEDs are located in the electronics hut of Belle II and the LED light is delivered via long optical fiber since there is only limited space around the Belle II spectrometer. ARICH has 90 holes in the support structure of the HAPD plane to install optical fibers to illuminate all the HAPDs. Photons are emitted toward aerogel tiles, and a part of photons are reflected by Rayleigh scattering in the aerogel. The scattered photons which enter

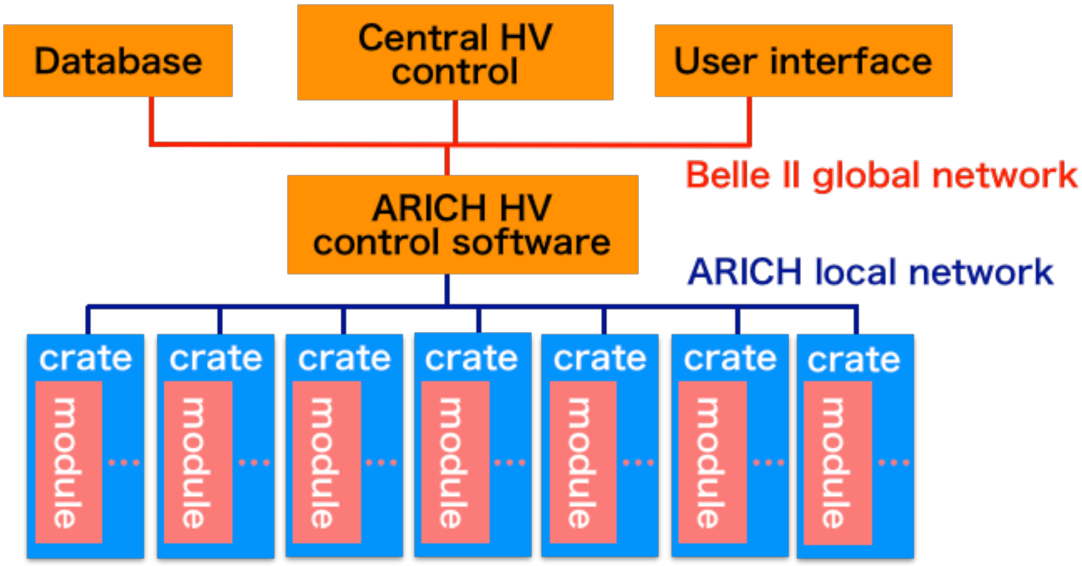

FIGURE 4.21: The conceptual map of network configuration of HV.

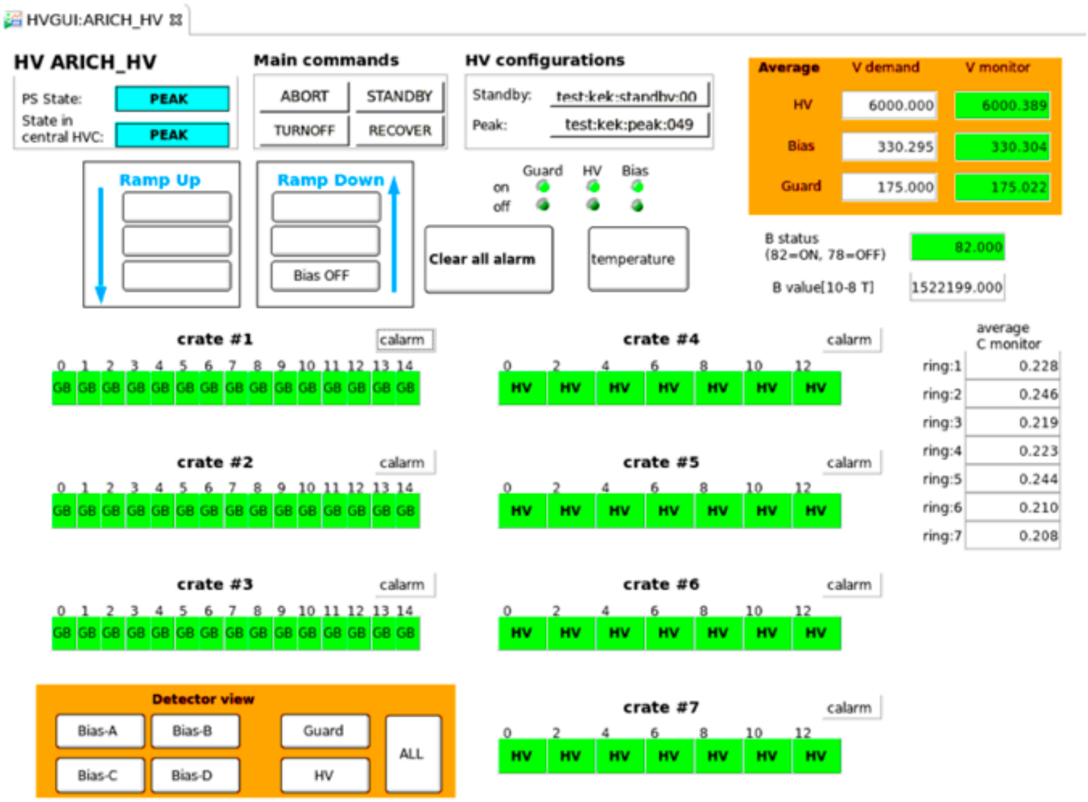

PS State: PEAK
State in central HVC: PEAK

Standby: test:kek:standby:00
Peak: test:kek:peak:049

Average	V demand	V monitor
HV	6000.000	6000.389
Bias	330.295	330.304
Guard	175.000	175.022

B status (82=ON, 78=OFF) 82.000
B value[10-8 T] 1522199.000

	average C monitor
ring:1	0.228
ring:2	0.246
ring:3	0.219
ring:4	0.223
ring:5	0.244
ring:6	0.210
ring:7	0.208

FIGURE 4.22: The snap shot of GUI for ARICH high voltage control system.

the windows of the HAPDs are detected and the performance of HAPD is examined.

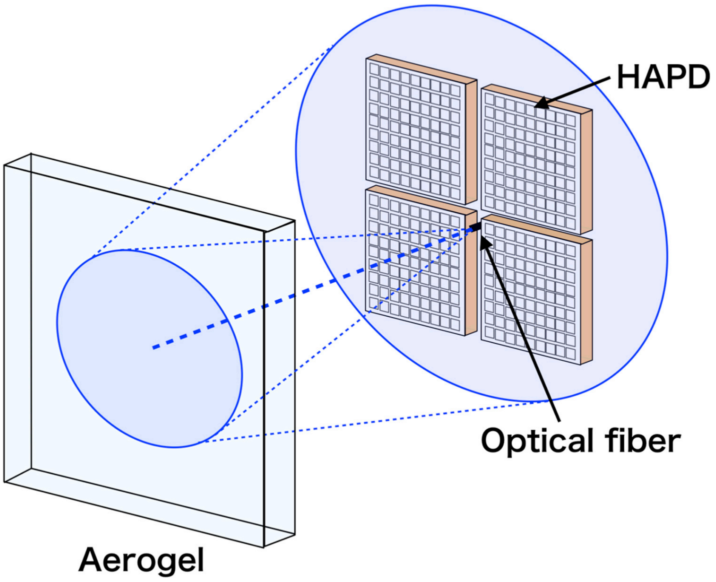

FIGURE 4.23: The conceptual image of the monitor system [77].

TABLE 4.6: Power usage of readout electronics corresponds to one MB and six FEBs.

Voltage	Board	Current [A]
+1.5 V	MB	1
+3.8 V	MB	1
+3.8 V	FEB	0.35
+2.0 V	FEB	1
−2.0 V	FEB	1.1

4.4.3 Low voltage power supply system

To operate readout electronics, we apply low voltage of typically 5 V. For ARICH case, a FEB requires +3.8 V, +2.0 V, and −2.0 volt, a MB needs +3.8 V and +1.5 V as input voltages. Since +3.8 V is common, we supply four types of voltage to operate readout electronics. In contrast to the high voltage system, one doesn't have to optimize the voltage board by board for the low voltage system. A low voltage power supply can be shared by many boards to reduce the cost and the complexity of the system. The power usage of readout electronics is summarized in Table 4.6. The maximum current of the power supply module is required to be 5 A and we commonly apply the low voltage to three MBs and 18 FEB from a low voltage output. We adopt a low voltage power supply module that is developed by ISEG. One module has eight output channels and twelve modules are used in total.

4.4.4 Data acquisition system

Belle II uses the common data acquisition (DAQ) system for all sub-detectors except PXD as written in subsection 3.2.7. The trigger signal is generated by collecting signals from CDC, ECL, TOP, and KLM. The trigger signal is distributed to the front-end electronics of ARICH by the front-end timing Switch (FTSW) module. Data from a MB is first sent to a High Speed Link

Board (HSLB) put on the COPPER board via Belle2Link. One COPPER board has four HSLBs and processes them. After adding header and footer, the data is sent to readout PC which builds an event with other sub-detectors. Each COPPER board has two network ports: data flow and slow control. Slow control such as parameter setting is performed via the COPPER board. Since ARICH uses 72 MBs, 18 COPPER boards and six readout PC are used in total.

Chapter 5

Installation and operation of ARICH

In this chapter, the installation of ARICH is described, and the verification of the healthiness of the photosensors in the Belle II spectrometer also described.

5.1 Installation

The structure of ARICH is mainly consists of two parts: the aerogel structure and the HAPD structure.

5.1.1 Aerogel

The aerogel structure is shown in Figure 5.1(a). All aerogel tiles were cut by water jet machining for four shapes that correspond to the place of cells depend on the radius. Before installing aerogel tiles, a black paper that prevents reflection on the wall of the structure is installed to each cell. Aerogel tiles were installed in the order of upstream one and downstream one. All tiles are fixed by fiber strings gluing for each cell as shown in Figure 5.1(b).

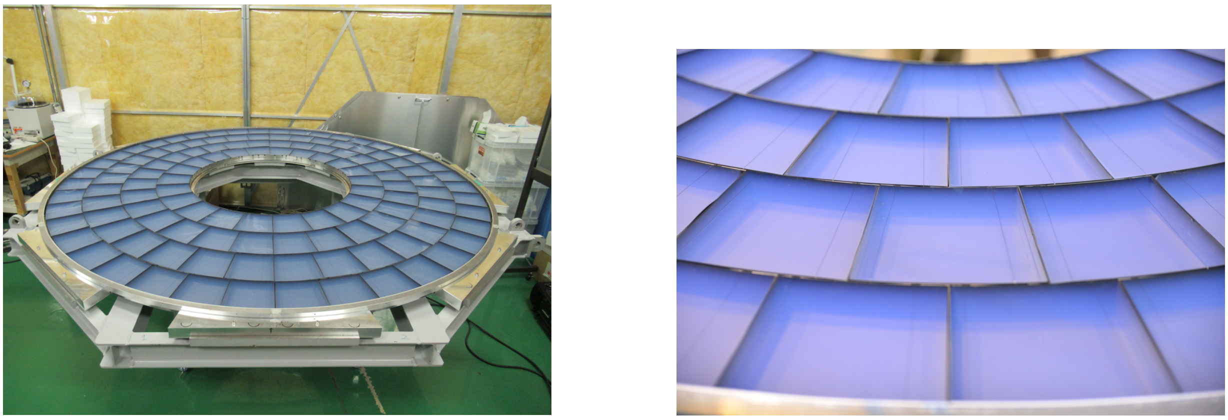

(a) The aerogel structure

(b) Zoomed

FIGURE 5.1: The picture of the aerogel structure (a) and zoomed picture (b).

5.1.2 HAPD and readout electronics

HAPD is directly attached to the socket of a FEB and the photo-cathode and the middle ring is connected to HV-divider board via short cables. HV-divider divides HV into two voltage using the register as discussed in subsection 4.4.1. All output pins of an HAPD are connected to the socket of a FEB, and the voltages of Bias and Guard of the HAPD are supplied via a FEB. A FEB has a connector for Bias-Guard input. HV input line of HAPD is connected a HV-divider board. The HAPD assembled with FEB and HV-divider board and it is called the "HAPD module" is shown in Figure 5.2(a). MB with cables to connect FEBs is shown in Figure 5.2(b).

HAPD modules were mounted to the HAPD structure shown in Figure 5.3(a). HAPD structure works as a common ground of ARICH. HV-divider boards were mounted to the back of the structure. MBs were also mounted to further back of the structure. A part of mounted HAPD modules and MB is shown in Figure 5.3(b).

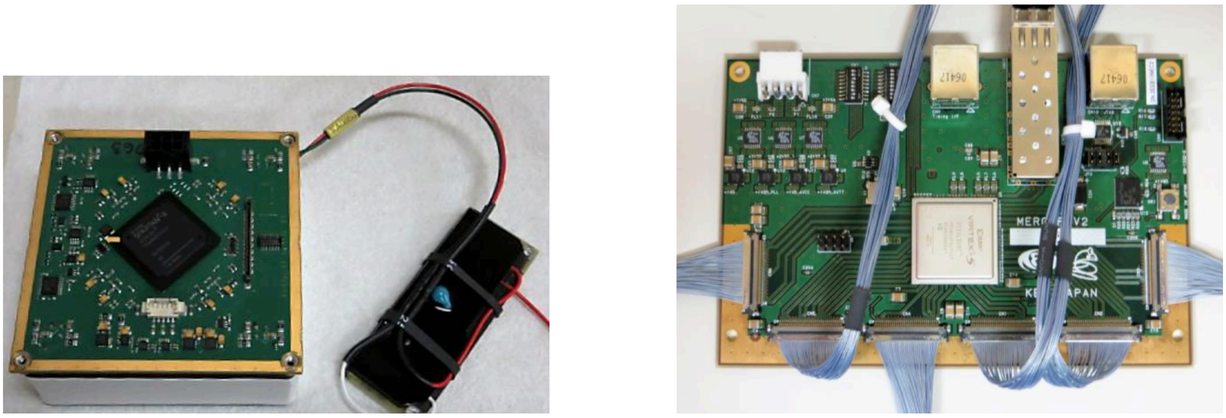
(a) HAPD module (b) MB

FIGURE 5.2: Pictures of (a) HAPD module and (b) MB.

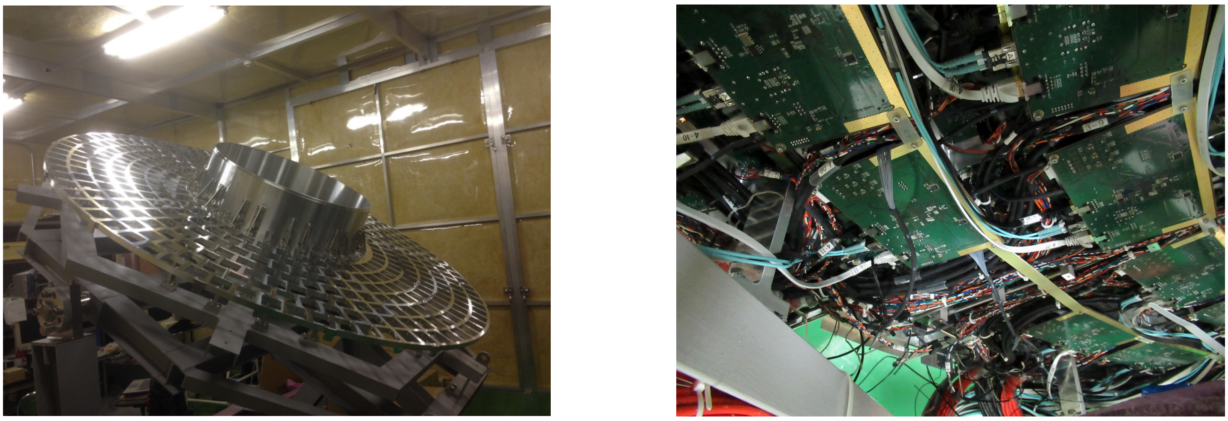
(a) The HAPD structure (b) Installed

FIGURE 5.3: Pictures of (a) the HAPD structure and (b) installed.

5.1.3 Cables

The conceptual image of cable connections is shown in Figure 5.4. Power supplies and COPPER boards are installed in the electronics hut which is located at a side of the Belle II spectrometer. FTSWs are installed to the access space of the Belle II spectrometer since it handles trigger signal and shorter length of cable is required. In addition, connections near ARICH is required so that one can locally construct and test the ARICH counter and then one can transport ARICH by crane when installing ARICH to the Belle II spectrometer. Details of each component are explained in the following section.

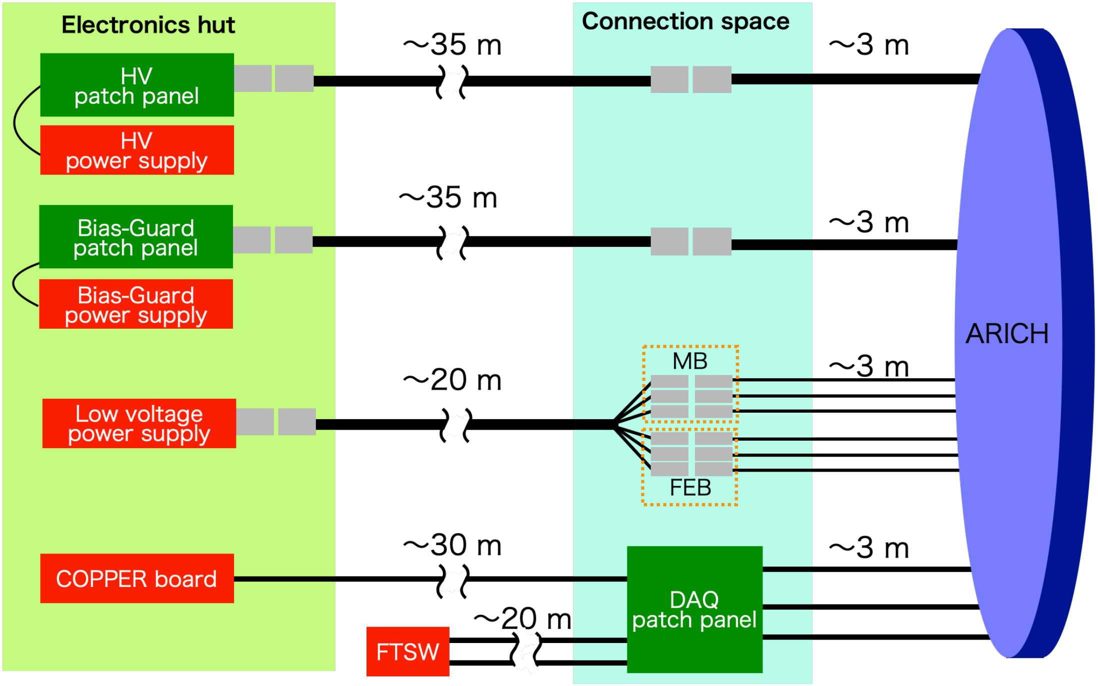

FIGURE 5.4: Conceptual image of cable installation.

Cables from high voltage power supply

We use two types of cables that correspond to the power supply of Bias-Guard and HV. A Bias-Guard cable has 48 lines with an outer sheath. It covers nine HAPDs, one spare line, and two ground lines. Therefore, 48 Bias-Guard cables are used in total. Five lines of Bias-Guard cable were braided for each HAPD. Crimped pins are put into the connector and it is inserted to the connector of FEB. The connector has an additional hole to insert ground pin. Two connectors in one Bias-Guard cable is also inserted the ground pin. The ground is common for all lines since the ground is electrically connected via the HAPD structure.

For HV cable, high insulation is required to avoid the dielectric breakdown at the operation of $-9000\,\mathrm{V}$ in the limited space of the cable path. It requires high hermeticity and we adopt coaxial cables for each line and bundle them by a cable tie. An HV cable bundle consists of 19 coaxial cables and one cable is spare. Connecter has 21 pins, remained two pins are connected to the cable sheath. Therefore, 24 HV cables are used in total. I had considered how to process the HV cables especially the connection to the HV-divider board. The sheath of HV cable is too thick and too firm to route the cable in the limited space and we remove all materials outside of insulator for the cable section that goes inside ARICH. The outer conductor which works as grounds of the cable is connected to the HAPD structure. The tip of HV cables has to be carefully sealed to avoid dielectric breakdown at the operation of $-9000\,\mathrm{V}$. It is covered by a heat-shrinkable tube after crimping the pins for both the female and the male side. Once the pins are connected, we cover them with another heat-shrinkable tube to fix and insulate.

The high voltages are delivered via $30 - 40\,\mathrm{m}$ long cables to connection space. All the cables are basically the same as above but connectors are considered. Connection space near ARICH is quite limited and one can just connect male and female connector. The mapping of the $30 - 40\,\mathrm{m}$ long cable, therefore, is required to be matched to that of the HAPDs. The connectors of the other end of the cable are not directly connected to power supplies since the mapping between the power supply and cable are not consistent. We have prepared a patch panel for each high voltage power supply crates. It manages the mapping between the power supply and cables and converts the connector to handle simply.

All the cables and patch panels were tested by applying maximum voltage individually before installation. I confirmed that it has no problem to use ARICH.

Cables from low voltage power supply

To reduce the space usage, a low voltage of six FEBs connected to the same MB is supplied from one cable and low voltage is distributed at just behind the board. Therefore, the tip of low voltage cable for FEB has a simple circuit to distribute low voltages and grounds to six FEBs. For MB, one cable is used for one MB. Four pins connectors and six pins connectors are used for MB and FEB, respectively. Half of the pins are used for ground for each voltage. Since low voltage is commonly applied for three MBs and up to 18 FEB, it is delivered with one cable to connection space. The cable is divided into six cables; three of them are used for MBs and remaining cables are used for FEBs. Therefore, one low voltage module connects two low voltage cables. In addition, low voltage power supplies are installed at the nearest place in the electronics hut in order to reduce cable length. The length of long cable is about 20 m, which is shorter than high voltage cable to reduce the effect of voltage drop.

DAQ

One MB uses two LAN cables for trigger and JTAG, and an optical cable for data flow and slow control. Category seven LAN cable is used for a trigger signal and category six LAN cable is used for JTAG. We use the DAQ patch panel which contains 24 ethernet relay connectors and 12 optical relay connectors for the connection space and it corresponds to one-sixth of ARICH. Optical cables are connected to COPPER boards located in the electronics hut. LAN cables are connected to FTSW located at the access space of the Belle II spectrometer.

5.1.4 Test after the assembly of ARICH

To confirm if the assembly of the ARICH counter components is successfully done, various tests were performed. Before combing the aerogel structure and HAPD structure, HAPDs had been exposed to the room light and high voltages cannot be applied. Therefore, only the DAQ test was performed before combing the structure. Since we could prepare a limited number of low voltage power supplies at this time, the DAQ test was performed part by part. Applying low voltage to electronics and reading the register, we checked the connection between MB and FEB.

Also changing the parameter and reading dummy data made by test pulse in FEB, we verify that slow control and data flow were also working correctly. We found problems with occasional poor connections, misconnections, and failure of data sent, and so on. Those problems had been solved by re-connection and re-initialization. Finally, we verify that all the DAQ was working as expected.

After combining the aerogel structure and HAPD structure, light tightness can be kept for HAPDs and high voltages can be applied. Since DAQ had been already tested, the test of HAPDs with applying high voltage was important after combing the structure. At the test of HAPDs with high voltage, we used the practical high voltage system with one-sixth of ARICH. We checked the mapping of connection especially bias voltage, since values of bias voltages are optimized for each channels and swapped connection may damage APD by overvoltage. For safety, we apply only 50 V which is sufficiently lower than the breakdown voltage of APDs but is sufficiently large to make depletion layer for APDs. We apply voltage to a part of APD in an HAPD. Since the noise level is changed by applying a bias voltage, we can check which APD is applied by checking the pattern of reduction of the noise level. We found that three pairs are swapped and fixed by re-connection, and all the mapping of connection was verified. We also checked the signal coming from photons by applying all high voltages. Since entire ARICH structure is just shaded with a black sheet, light tightness was not perfect and some photons comes in and we check that signal. During ramping up the voltage, several channels were tripped due to large leakage currents. A part of them was due to bad insulation of a cable line or bad electrical contact at a connecter, and it was fixed by company and re-connection work. However, two guards and two biases could not be fixed. Those channels indicated the same HAPD even changing connections, therefore, we conclude those channels were broken. The fraction of those channels are found to be 0.6 % of the area of ARICH, which sufficiently small. We concluded that the construction of ARICH is properly completed and is ready to be installed into the Belle II spectrometer.

5.2 Operation of ARICH after installation

After ARICH was installed into the Belle II spectrometer, we performed the test of HAPDs and checked if they are working properly in the practical environment.

5.2.1 Method of HAPD performance evaluation

To evaluate the performance of HAPD under the Belle II operation, the monitor system is used. The hit distribution obtained by the monitor system is shown in Figure 5.5. The average number of hits while LED off and on are 2.7×10^{-5} hits/ch/trigger and 0.18 hits/ch/trigger, respectively. The blank part in Figure 5.5 are related to unused HAPD due to high voltage power supply troubles (cables and patch panel etc.), troubles in HAPD (broken APD and circuit etc.), and troubles in the readout electronics.

Since ARICH uses only hit information, we perform a so called “threshold scan” to obtain pulse height information. The conceptual picture of the threshold scan is shown in Figure 5.6.

We measure the hit rate while changing threshold voltage, and the distribution of hit rate as a function of the threshold voltage is used to evaluate the performance. For the noise, the distribution is represented as Gaussian, and the mean and sigma represent offset and noise level, respectively. For the ideal signal, the distribution shows a rectangular shape, the width of the distribution corresponds to the pulse height. The real signal is the convolution of noise and the ideal signal. The shape represents the complementary error function for shoulder and Gaussian for the peak. The difference of the threshold voltage between shoulder and mean corresponds pulse height of 1 p.e.

The fitting example of a threshold scan for the practical signal is shown in Figure 5.7. The distribution is fitted for noise and shoulder, separately. The fitting function for noise is one Gaussian plus first-order polynomial, and that for the shoulder is the complementary error function. The noise level, the offset, and the pulse height are determined by the sigma of Gaussian, mean fo Gaussian and difference between the mean of Gaussian and complementary error function, respectively.

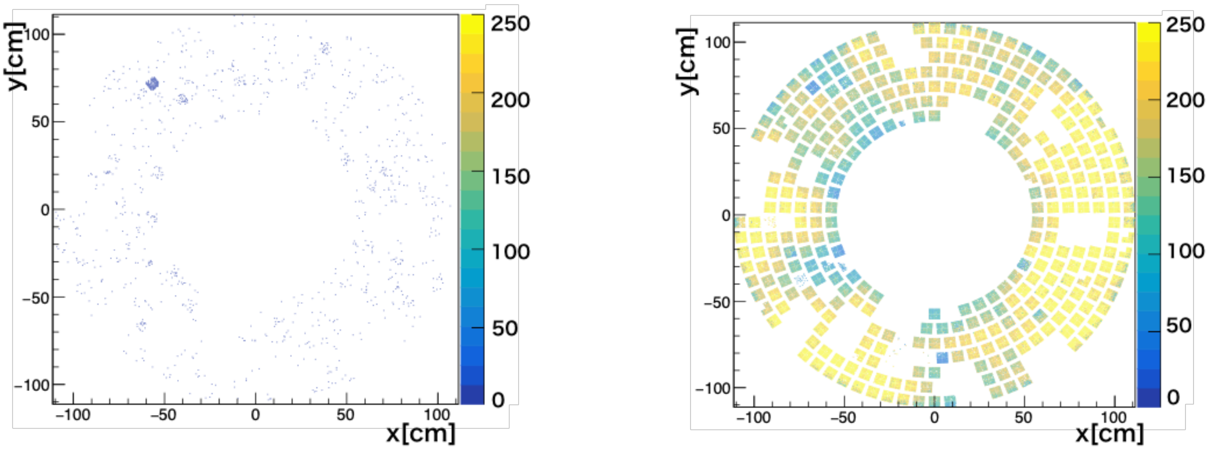

(a) LED off

(b) LED on

FIGURE 5.5: The hit distribution using LED monitor system. (a) LED off and (b) LED on.

5.2.2 Healthiness of HAPDs

The healthiness of HAPDs in the Belle II spectrometer is verified during the beam commissioning period of the Belle II experiment [78]. It is evaluated by measuring noise level, offset value, pulse height, and signal-to-noise ratio. The leakage current in the APD chip is an indicator of HAPD healthiness. The noise level is expected to decrease by applying reverse bias voltage since the depletion region is generated. The distribution of the noise level with and without the bias voltage is shown in Figure 5.8(a). The mean value of both distributions is 6.5 mV and 13.4 mV for with and without applying a bias voltage, respectively. The reduction of the noise level by applying bias voltage is clearly seen. The alignment of the offset value is important since ARICH use the same threshold voltage for all channels, and the variation of the offset value is required to be less than the noise level. The distribution of the offset value is shown in Figure 5.8(b). The distribution of the pulse height is shown in Figure 5.8(c). The signal-to-noise ratio is defined as

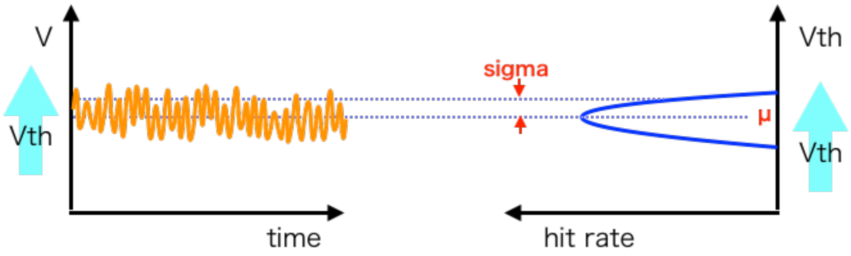

(a) noise

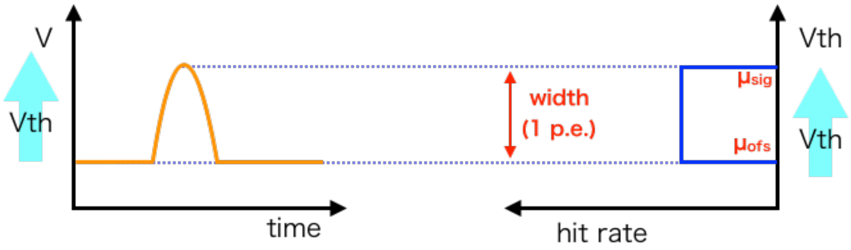

(b) ideal signal

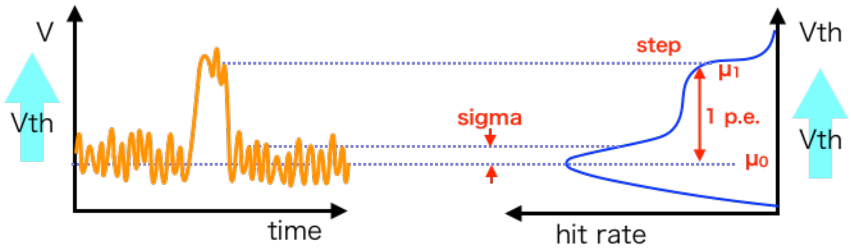

(c) practical signal

FIGURE 5.6: The conceptual picture of threshold scan (a) noise, (b) ideal signal and (c) practical signal.

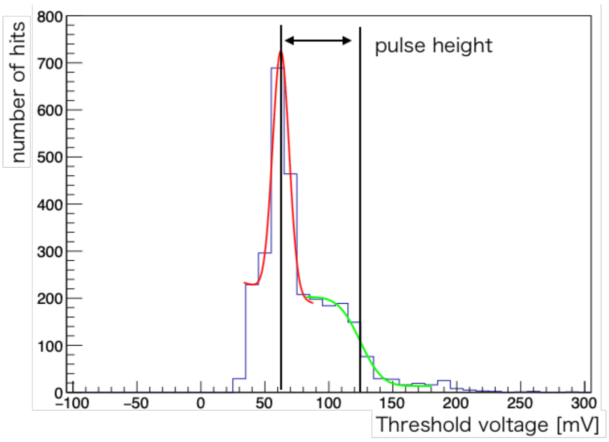

FIGURE 5.7: The example of fitting to the threshold scan. Red line is Gaussian for noise, green line is error function and the difference between the noise and error function is pulse height for 1 p.e.

the ratio of pulse height to noise level. It is required to sufficiently large. The distribution of signal-to-noise ratio is shown in Figure 5.8(d).

The results of the basic performance of HAPDs are summarized in Table 5.1. The sigma value

TABLE 5.1: Basic performance of HAPDs.

	Mean	Sigma
Offset [mV]	61.7	2.3
Noise [mV]	6.5	0.67
pulse height [mV]	67.1	9.1
signal-to-noise ratio	10.3	1.8

of the offset value is 2.3 mV, and it is smaller than the noise level. The mean value of signal-to-noise ratio is 10.3, and 99 % of channels can distinguish signal from noise with 3σ. Thus, the pulse height is sufficiently larger than the noise level.

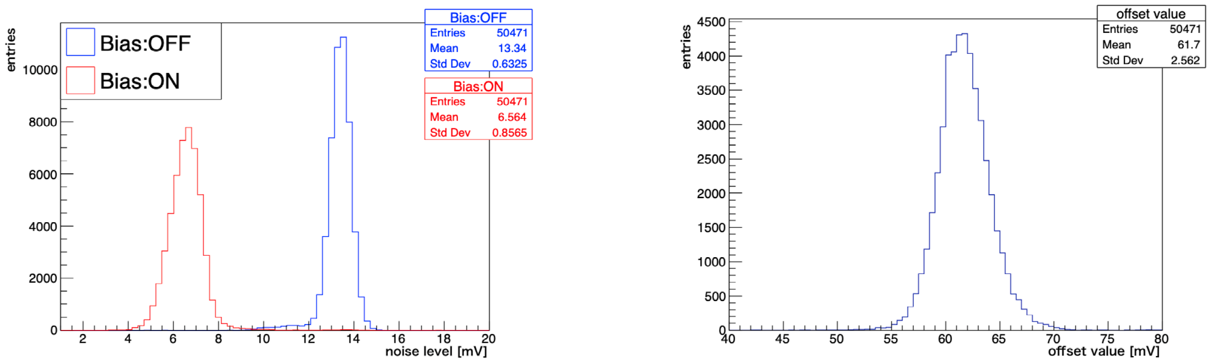

(a) noise

(b) offset

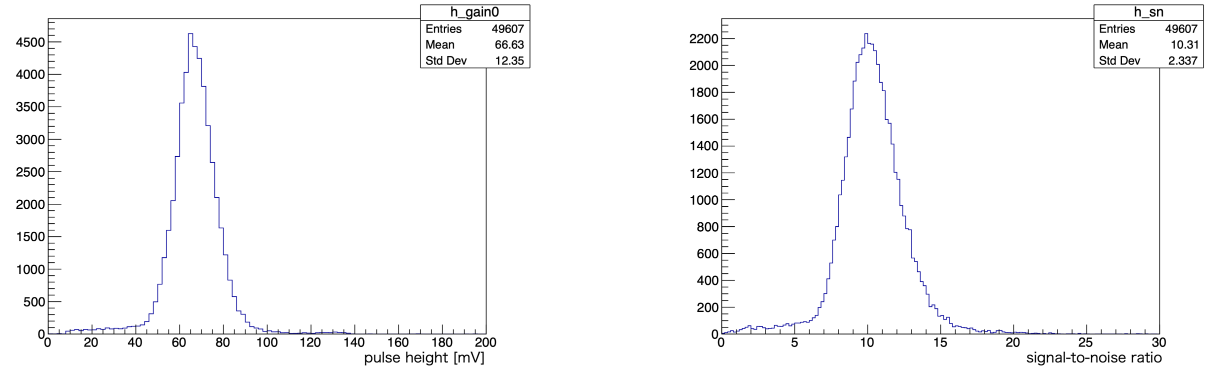

(c) pulse height

(d) signal-to-noise

FIGURE 5.8: The distributions for (a) noise, (b) offset, (c) pulse height, and (d) signal-to-noise ratio.

We found the temperature of the electronics is higher than our expectation during the first Belle II beam commissioning period. Therefore, we evaluate the performance of the HAPDs at three different temperatures: right after turning on electronics (approximately 30 °C: cooler), the intermediate temperature near the usual operation temperature (approximately 36 °C: usual), and near the temperature limit of safe operation (approximately 41 °C: warmer). The distributions of noise level, offset value, pulse height, and signal-to-noise ratio for three different temperature is shown in Figure 5.9. Note that bias voltage is applied only for pulse height measurement. The results are summarized in Table 5.2. The offset value has a small shift with

TABLE 5.2: Performance dependency of HAPDs.

	Offset [mV]	Noise [mV]	Pulse height [mV]	Signal-to-noise ratio
Cooler	61.7	13.4	69.7	10.7
Usual	60.8	15.8	65.5	8.7
Warmer	60.5	15.7	58.3	7.6

temperature changes, the noise level is increased, and the pulse height and signal-to-noise ratio is decreased with higher temperature. From signal-to-noise ratio distribution, 99 % of channels still keeps $3\,\sigma$ of separation between signal and noise. Therefore, we conclude that ARICH can be operated even near the temperature limit of HAPDs.

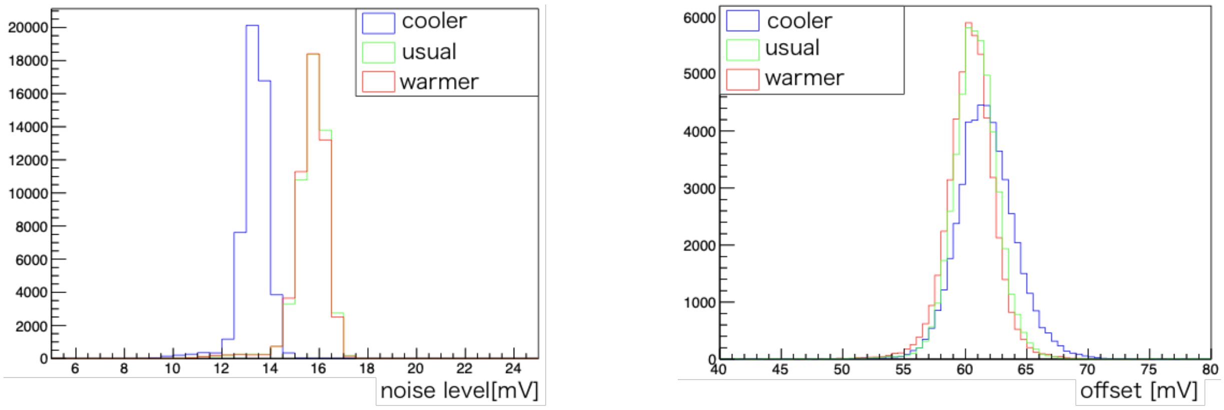

(a) noise

(b) offset

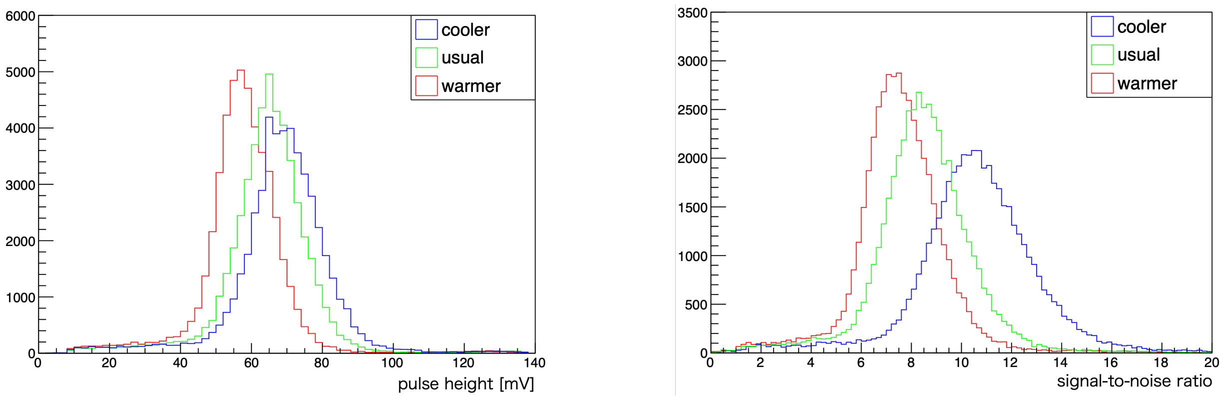

(c) pulse height

(d) signal-to-noise ratio

FIGURE 5.9: The distributions of temperature dependency. (c) noise, (b) offset, (c) pulse height, and (d) signal-to-noise ratio.

5.2.3 HAPDs in the commissioning of Belle II

We monitored the performance of the HAPDs in the beam commissioning of Belle II by measuring the trend of the signal-to-noise ratio and the fraction of dead channels. We pick up three days during the last month of operation, June 14th, June 28th, and July 17th, and compare results among them. The trends of the signal-to-noise ratio and the fraction of dead channels are shown in Figure 5.10. The signal-to-noise exceeds seven and the fraction of dead channels are below

1 %. We find that HAPDs are stable and no degradation of performance is seen during the beam commissioning period.

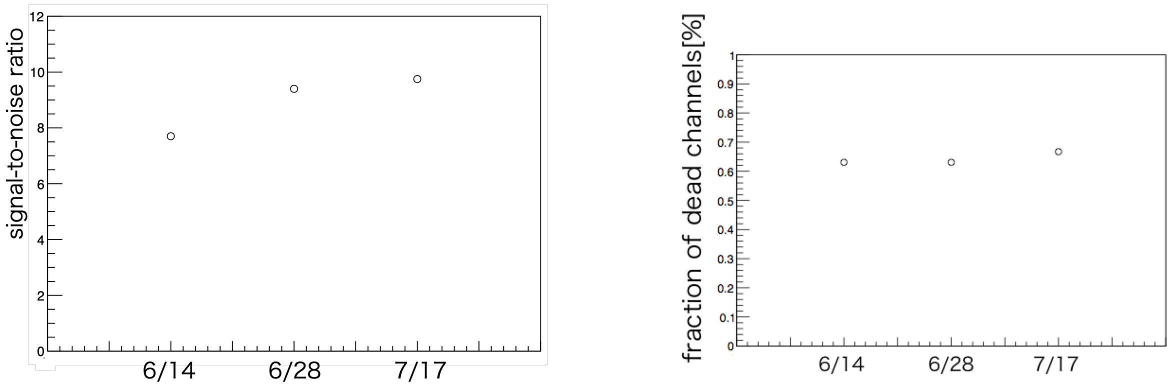

(a) signal-to-noise ratio

(b) fraction of dead channel

FIGURE 5.10: The distributions for (a) signal-to-noise ratio and (b) dead channel fraction.

Chapter 6

ARICH performance

In this chapter, the PID method of the ARICH counter is described and the PID performance using early beam collision data is evaluated [79].

6.1 PID method

Particle identification of the ARICH counter is performed based on the comparison between the observed pattern of photons and the expected pattern for given charged track parameters with an assumed particle type hypothesis. For each charged track passing through ARICH, we evaluate the value of likelihood function for six particle hypotheses: electron, muon, pion, kaon, proton, and deuteron. The likelihood function for a particle hypothesis h is defined as

$$\mathcal{L}_h = \prod_{\text{all channel}} p_{h,i}(m_{h,i}), \qquad p_{h,i}(m_{h,i}) = \frac{e^{-n_{h,i}} n_{h,i}^{m_{h,i}}}{m_{h,i}!}, \tag{6.1}$$

where the product runs over all pixels of whole ARICH counter, and $p_{h,i}(m_{h,i})$ is the probability of observing $m_{h,i}$ hits on the i-th pixel, while $n_{h,i}$ hits are being expected (for an assumed hypothesis of h) [80–82]. Since we do not discriminate multiple photons from single-photon hits in ARICH, $p_{h,i}(m_i)$ can be expressed as

$$\begin{aligned} p_{h,i}(\text{no hit}) &= e^{-n_{h,i}} && (6.2)\\ p_{h,i}(\text{hit}) &= 1 - p_{h,i}(\text{no hit}) = 1 - e^{-n_{h,i}} && (6.3) \end{aligned}$$

Using Equation 6.2 and Equation 6.3, Equation 6.1 can be rewritten as

$$\begin{aligned} \ln \mathcal{L}_h &= \sum_{\text{all channel}} \ln\{p_{h,i}(m_{h,i})\} && (6.4)\\ &= -\sum_{\text{no hit}} n_{h,i} + \sum_{\text{hit}} \ln(1 - e^{n_{h,i}}) && (6.5)\\ &= -\sum_{\text{no hit}} n_{h,i} - \sum_{\text{hit}} n_{h,i} + \sum_{\text{hit}} n_{h,i} + \sum_{\text{hit}} \ln(1 - e^{n_{h,i}}) && (6.6)\\ &= -\sum_{\text{all channel}} n_{h,i} + \sum_{\text{hit}} [n_{h,i} + \ln(1 - e^{n_{h,i}})] && (6.7)\\ \therefore \ln \mathcal{L}_h &= -N_h + \sum_{\text{hit}} [n_{h,i} + \ln(1 - e^{n_{h,i}})], && (6.8) \end{aligned}$$

where N_h is the expected total number of hits, and the sum runs only over pixels that were hit[1]. N_h is calculated from the number of emitted photons, transmission length of silica aerogel, and geometrical acceptance. $n_{h,i}$ is obtained by projecting the probability density function (PDF) which describes the expected angular distribution of Cherenkov photons and particle hypothesis, onto the photon-detector plane, and integrating over the surface of pad i. Both N_h and $n_{h,i}$ are taken into account the reconstructed photons having Cherenkov angle between 0.1 rad and 0.5 rad. We describe the construction of PDF in more detail in the next section.

Separation of kaons from pions is performed by imposing selection criteria on the likelihood ratios which are defined as

$$R_{K/\pi} = \frac{\mathcal{L}_K}{\mathcal{L}_K + \mathcal{L}_\pi}, \tag{6.9}$$

$$R_{\pi/K} = \frac{\mathcal{L}_\pi}{\mathcal{L}_K + \mathcal{L}_\pi} = 1 - R_{K/\pi}. \tag{6.10}$$

Adjusting selection criteria results in particle samples with different identification efficiency and purity.

6.1.1 Probability density function

We utilize the distribution of cosine angle between extrapolated track and a photon hit seen from the aerogel as the distribution of the PDF. This angle corresponds to the Cherenkov angle for the true Cherenkov photon.

The number of expected hits on a given channel ($n_{h,i}$) is obtained by projecting the probability density function (PDF) which describes the expected angular distribution of Cherenkov photons[2] for given track parameters and particle hypothesis onto the photon-detector plane and by integrating it over the surface of pixel i. The PDF is constructed from the following components:

(1) Cherenkov photons emitted in silica aerogel

A track extrapolated to ARICH will emit Cherenkov light in the silica aerogel if the velocity of particle excess the speed of light in the medium. The photons originated from this process will make two Gaussian peaks in the Cherenkov angle distribution, and both center at the expected Cherenkov angle. The main narrow peak describes non-scattered photons, and the other smaller and the wider peak is added to describe Rayleigh scattered photons. The magnitudes of both peaks are proportional to the expected number of emitted photons in the aerogel and the widths and fraction of each are determined by fitting the observed Cherenkov angle distributions in control samples, as described in the next paragraph. The different expected numbers of emitted photons are assigned for each different aerogel layer.

(2) Cherenkov photons emitted from quartz window of HAPDs

Cherenkov photons can also be emitted when a track passes through the quartz window of

---

[1] This greatly simplifies evaluation of Equation 6.1 since the expected number of hits only needs to be calculated for pixels having photon hits. Calculation on all the pixels of whole ARICH is unnecessary.

[2] In the track coordinate system

an HAPD. Some photons are promptly converted to photo-electrons and will make a Gaussian peak around the incident point of the track. Others are converted to photo-electrons after repeating total internal reflection in the quartz window. This latter component is separately determined in case whether the extrapolated track enters to quartz window or not, since it has a large difference. They contribute to an exponential shape combining second-order or first-order polynomial function for extrapolated track that enters quartz window or not, respectively.

(3) Random hits due to electronics noise etc.

This component does not make a significant contribution and is assumed that the distribution is uniform over the photon detector plane.

(4) Other backgrounds

This contains contributions of beam backgrounds, δ-rays emitted at inner volume and decayed particles etc. In terms of fitting, it is merged to (2) as the contribution is small and the shape of the distribution is similar to (2).

We determine each component by fitting the distribution of the Cherenkov angle, and details are described in the following sections.

6.2 PDF calibration

The PDF has to be determined precisely to represent Cherenkov angle distribution for each particle hypothesis in order to identify particles correctly. The PDF calibration using samples of real data is performed by fitting to the distribution of the Cherenkov angle. The fitting function is constructed from the following items:

Two Gaussian functions of (1)

They represent the contribution of the Cherenkov photons emitted in the silica aerogel tiles. Non-scattered photons are the major component and is described by a narrower Gaussian function, and Rayleigh scattered photons are the minor component and is described by a wider Gaussian function. The mean values of both Gaussian functions are fixed to be the same parameter. The width of the main narrow Gaussian function is fixed to be a constant, and the detail is described in subsection 6.2.1. The other four parameters are free parameters.

One constant value of (3)

Contribution of random hits described in subsection 6.2.2 treated as a fixed value.

One Gaussian function, one exponential and second-order polynomial of (2)

This function is used for the case when a track hits a quartz window. All parameters are treated as free.

One exponential and first-order polynomial of (2)

This function is used for the case when a track doesn't hit to quartz windows. All parameters are treated as free.

We obtain all free parameters by fitting the Cherenkov angle distributions that are made using real data, and those are incorporated in the PDF.

The $e^+e^- \to \mu^+\mu^-$ and $K_S^0 \to \pi^+\pi^-$ samples which correspond to an integrated luminosity of 2.62 fb^{-1} are used for the PDF calibration. The $e^+e^- \to \mu^+\mu^-$ events provide a clean sample since this process can be easily identified by requiring exactly two tracks in the event, and by identifying both tracks as muons using outer detectors (ECL and KLM). The tracks of this sample only cover high momentum range, while the K_S^0 sample is used to calibrate the PDFs for low momentum range.

6.2.1 Resolution function

The width of the Cherenkov angle, which corresponds to that of the main narrow Gaussian, depends on the tracking resolution. The tracking resolution strongly depends on the momentum. Therefore, we implement the width of the Cherenkov angle as a function of the momentum. To measure the width of Cherenkov angle, we use $e^+e^- \to \mu^+\mu^-$ for momentum around 7 GeV/c and $K_S^0 \to \pi^+\pi^-$ for momentum below 5 GeV/c. The width of the Cherenkov angle as a function of the momentum is shown in Figure 6.1. The width contains intrinsic resolution of the Cherenkov angle $\sigma_{\mathrm{PDF}}(p)$ and the geometrical resolution σ_{pad} i.e. resolution due to pad size and incident angle of photons. The function of width $f(p)$ is defined as

$$f(p) = \sigma_{\mathrm{PDF}}(p) \oplus \sigma_{\mathrm{pad}}; \quad \sigma_{\mathrm{PDF}}(p) = \sqrt{(A/p)^2 + B^2}, \tag{6.11}$$

where A and B are parameters determined by the fitting. The $\sigma_{\mathrm{PDF}}(p)$ is motivated by the momentum dependency of angular dispersion due to multiple scattering. The average of geometrical resolution is estimated to be σ_{pad} = 6.4 mrad and is included as a constant. Then, we determine the parameters (A and B) by fitting the measured momentum dependence of the width of Cherenkov peak.

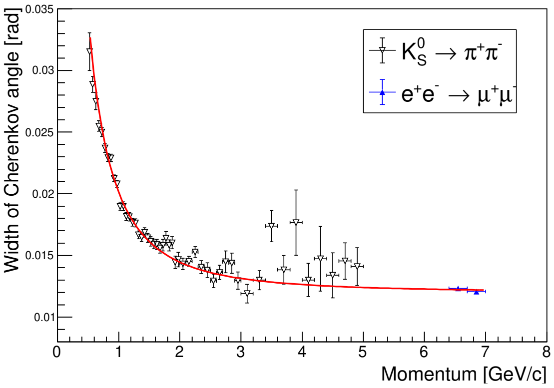

FIGURE 6.1: The width of Cherenkov peak as a function of the momentum. Red curve is fitting curve.

6.2.2 Random noise

Our time window is 126 ns and we record four bits which corresponding to the timing inside the time window, and from which we can estimate the rate of off-timing events. Since the contribution of random hits to the overall background is relatively small, we assume the rate of those to be the same for all pixels. Fig. 6.2 shows the distribution of the number of random hits per event for all pixels of the detector, along with the average value which is used in the PDF. As a result, the number of random hits per event for all pixels is calculated to be 1.4×10^{-4}.

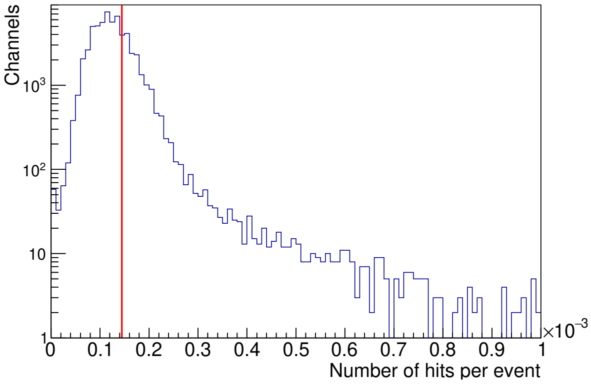

FIGURE 6.2: Distribution of the number of hits per event per channel. Red line is average value which is implemented in the PDF.

6.2.3 Remaining components

The rest of the PDF parameters are calibrated by fit using $e^+e^- \to \mu^+\mu^-$ samples. The fitting function is summarized in Table 6.1. The fitting is performed for the case when track extrapolated to HAPD quartz window or not, separately. The both distributions with the fitting function are shown in Figure 6.3 and the determined values are also summarized in Table 6.1. The fitting is performed well, and the remaining parameters are determined.

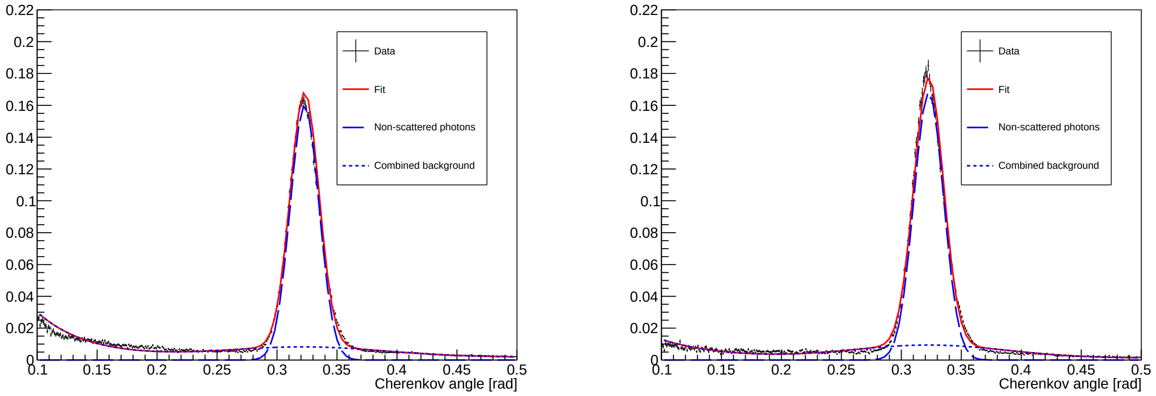

(a) Window hit

(b) No window hit

FIGURE 6.3: The fitting results for (a) track enters to quartz window or (b) not.

TABLE 6.1: The fitting function and the determined value.

Component	Function	Parameter	Determined value	Comment
Non-scattered photons	Gaussian	Constant	0.160	
		Mean	0.323 (fixed)	
		Sigma	0.0128 (fixed)	subsection 6.2.1
Scattered photons	Gaussian	Constant	0.006	
		Mean	0.323 (fixed)	
		Sigma	0.651	
Random hits	Constant		1.4×10^{-4} (fixed)	subsection 6.2.2
Track extrapolated to HAPD window	Gaussian	Constant	1.1	
		Mean	0.0101	
		Sigma	0.0152	
	Exponential ($\exp(A+Bx)$)	A	19.5	
		B	-24.0	
	Second-order polynomial	Order 0	1.09×10^{-9}	
		Order 1	0.0109	
		Order 2	-0.0151	
Track doesn't extrapolated to HAPD window	Exponential ($\exp(A+Bx)$)	A	9.71	
		B	-19.5	
	First-order polynomial	Order 0	5.2×10^{-6}	
		Order 1	2.18×10^{-3}	

6.2.4 Comparison

The result of the PDF calibration is verified by comparing the measured distribution and expected distribution obtained by filling the histogram of reconstructed Cherenkov angles of all pixels weighted by the expected average number of hits for the pixel, as evaluated from the PDF. The results are shown in Figure 6.4 and Figure 6.5 using $e^+e^- \to \mu^+\mu^-$ sample and $K_S^0 \to \pi^+\pi^-$ sample, respectively. Figure 6.5 shows the distributions in the momentum range of 0.3 GeV/ls to 1.3 GeV/ls for $K_S^0 \to \pi^+\pi^-$ sample, section B.1 shows the distribution in the all momentum range which corresponds to the range of 0.0 GeV/c to 4.0 GeV/c. The results show that the calibration of PDF is performed well in the a wide range of momentum.

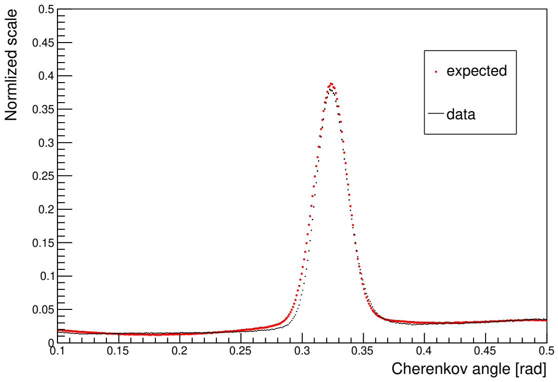

FIGURE 6.4: Comparison of Cherenkov angle distributions between data and PDF expectation using $e^+e^- \to \mu^+\mu^-$ sample. Both distributions are normalized by the number of tracks.

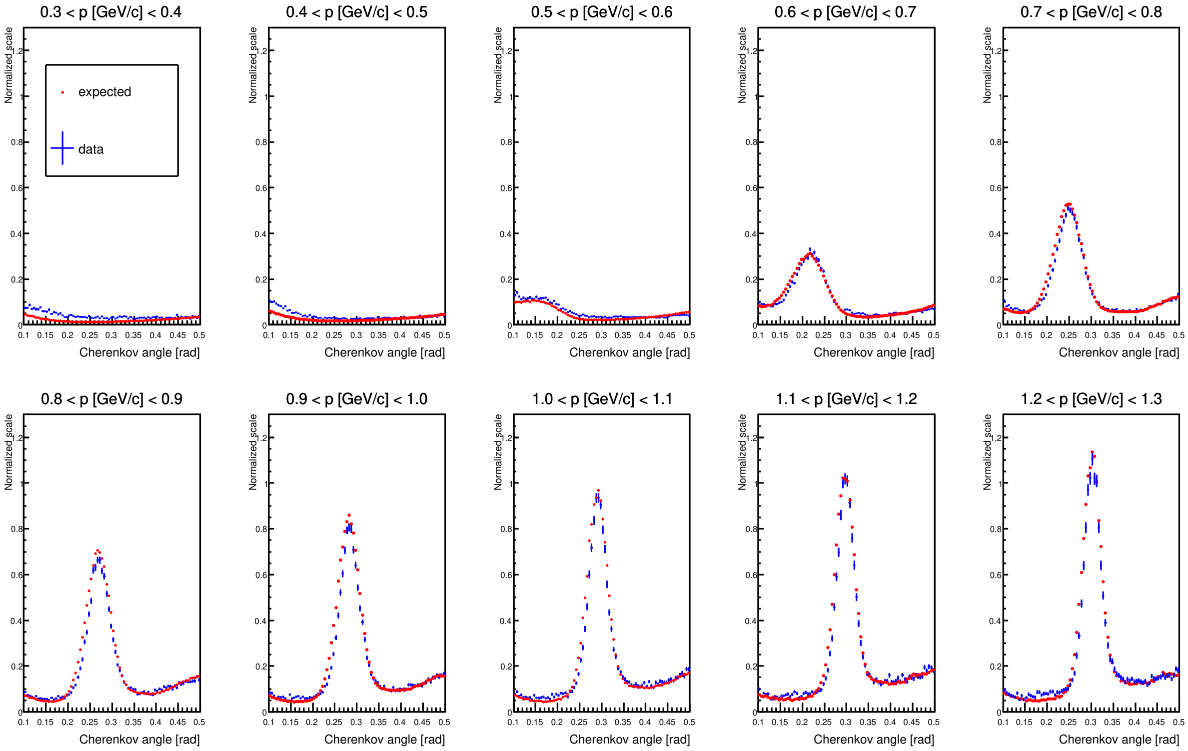

FIGURE 6.5: Comparisons of Cherenkov angle distributions between data and PDF estimation using $K_S^0 \to \pi^+\pi^-$ samples. Blue marker is data and Red marker is PDF estimation. Both are normalized by number of tracks. Each figure shows different momentum range.

6.3 Evaluation of K/π ID performance

I evaluate K/π identification performance using the control sample. The control sample is required to identify the particle without particle identification and high statistics and purity. $D^{*+} \to D^0(\to K^-\pi^+)\pi^+$ decay is used as control sample.

6.3.1 Event selection

We use D^* samples in $e^+e^- \to B\bar{B}$ and $e^+e^- \to q\bar{q}(q = u, d, s, \text{and } c)$ data which corresponds to an integrated luminosity of 5.15 fb^{-1}, and Monte Carlo (MC) simulation data with present Belle II geometry which corresponds to an integrated luminosity of 10 fb^{-1}.

We use $D^{*+} \to D^0(\to K^-\pi^+)\pi^+$ decays[3] to evaluate the particle identification performance. This decay can be reconstructed with a relatively low background level without requiring particle identification information for pion and kaon tracks from D^0 decay. A track coming from a D^0 decay is self-identified as pion (kaon) if the track have the same (opposite) charge as the “slow pion” from the D^* decay.

To reconstruct D^*, we require $|M_{D^{*+}} - M_{D^0} - 0.1454\,\text{GeV}/c^2| < 0.0015\,\text{GeV}/c^2$. To evaluate the performance of ARICH, π^+ or K^- track from D^0 decay is required to be extrapolated from

---

[3] charge-conjugated more is always implied as well

CDC to the ARICH counter region. In addition, more than one wire hits in CDC is required to keep the quality of tracks.

6.3.2 Efficiency and misidentification probability

The particle identification performance is discussed in terms of identification efficiency and the misidentification probability. Both of these are determined as a ratio of the number of reconstructed D^* decays after or before particle identification applied, i.e.:

$$K\,\text{efficiency} = \frac{\text{number of K tracks after } R_{K/\pi} > R_{\text{cut}}}{\text{number of K tracks}} \tag{6.12}$$

$$\pi\,\text{efficiency} = \frac{\text{number of } \pi \text{ tracks after } R_{\pi/K} > R_{\text{cut}}}{\text{number of } \pi \text{ tracks}} \tag{6.13}$$

$$K\,\text{misidentification probability} = \frac{\text{number of K tracks after } R_{K/\pi} < 1 - R_{\text{cut}}}{\text{number of K tracks}} \tag{6.14}$$

$$\pi\,\text{misidentification probability} = \frac{\text{number of } \pi \text{ tracks after } R_{\pi/K} < 1 - R_{\text{cut}}}{\text{number of } \pi \text{ tracks}}, \tag{6.15}$$

where R_{cut} is the criterion of the particle identification, and the number of $K(\pi)$ tracks is equivalent to the number of reconstructed D^* decays with $K(\pi)$ track that is extrapolated to ARICH. We determine the latter by performing an unbinned maximum likelihood fit of the D^0 mass distribution within the range between $1.8\,\text{GeV}/c^2$ and $1.9\,\text{GeV}/c^2$. The fit function consists of a Gaussian function as the signal and a first-order polynomial function as a background contribution. Mean and sigma of the Gaussian is fixed by using the fitting result of the distribution before applying $R_{K/\pi}$ or $R_{\pi/K}$ selection. For fitting to the distribution before applying $R_{K/\pi}$ or $R_{\pi/K}$ selection, both mean and sigma are floated. The signal yield, background yield and parameters of the first-order polynomial are floated. Using the signal yield with uncertainty after (before) identification selection criteria $A \pm \sigma_A$ ($B \pm \sigma_B$), the efficiency and misidentification probability with the uncertainty $\epsilon \pm \sigma_\epsilon$ is determined as

$$\epsilon \pm \sigma_\epsilon = \frac{A \pm \sigma_A}{B \pm \sigma_B} = \frac{A}{B} \pm \frac{1}{B}\sqrt{\epsilon^2\sigma_B^2 + \sigma_A^2 - 2\epsilon^{3/2}\sigma_A\sigma_B} \tag{6.16}$$

$R_{K/\pi}$ distributions for π and K tracks having more than $0.7\,\text{GeV}/c$ using MC and data are shown in Figure 6.6. K-like particles are concentrated around 1 and π-like particles are concentrated around 0. K tracks and π tracks are well identified as K-like and π-like particles by ARICH.

Figure 6.7 and Figure 6.8 show D^0 mass distribution before and after applying $R_{K/\pi}(R_{\pi/K})$ requirement for $K(\pi)$ track with a fitting curve using MC and data, respectively. The height of the peak is decreased by applying $R_{\pi/K}(R_{K/\pi}) > 0.6$ for $\pi(K)$ tracks, and this reduction contribute the $\pi(K)$ inefficiency, On the other hand, the peak is remained by applying $R_{\pi/K}(R_{K/\pi}) < 0.6$ for $\pi(K)$ tracks, and this residual contributes the $\pi(K)$ misidentification probability. $K(\pi)$ efficiency and $\pi(K)$ misidentification probability using the fitting results are summarized in Table 6.2. There are about 3 % differences between data and MC for both K and π. The receiver operating characteristic (ROC) curve is shown in Figure 6.9.

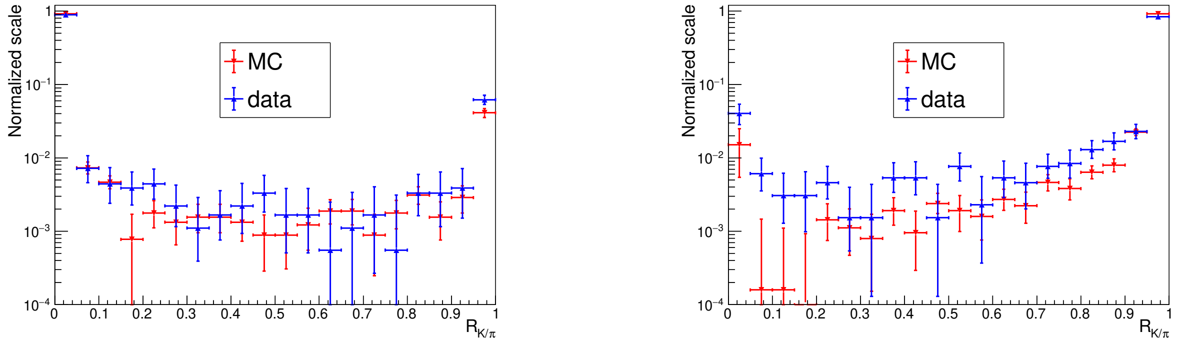

(a) π tracks

(b) K tracks

FIGURE 6.6: Comparison the distribution of $R_{K/\pi}$ between MC and data for (a) K tracks and (b) π tracks. All distributions are normalized by number of tracks.

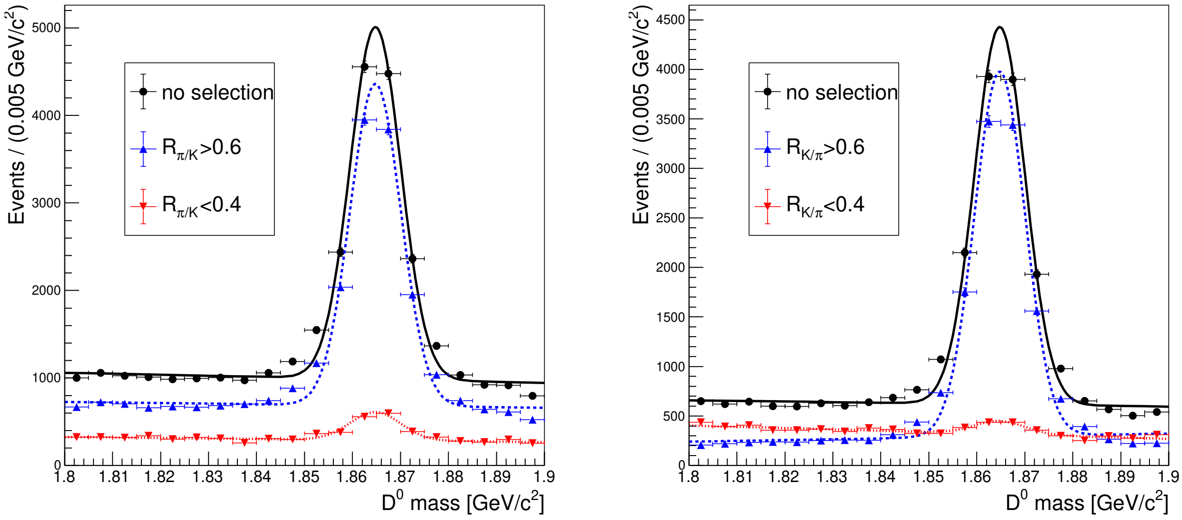

(a) π tracks (MC)

(b) K tracks (MC)

FIGURE 6.7: Distribution of D^0 mass using MC before and after applying $R_{\pi/K}(R_{K/\pi})$ cut for (a) π track and (a) K track. Black solid, blue dashed and red dotted curves are fitting curve for each D^0 mass distribution.

6.3.3 Momentum and Polar Angle Dependency

We study the dependency of the performance on the track momentum and polar angle by dividing candidates in bins of those two variables. We measure $\pi(K)$ efficiency and $K(\pi)$ misidentification probability with $R_{\text{cut}} = 0.6$ in each bin, and the results are shown in Figure 6.10 and Figure 6.11. They show good identification performance even at high momentum region and at large polar angle region (where many Cherenkov photons are reconstructed with mirror reflection). Those results demonstrate that the performance of ARICH as a particle identification device is good and as is expectated for all acceptance regions.

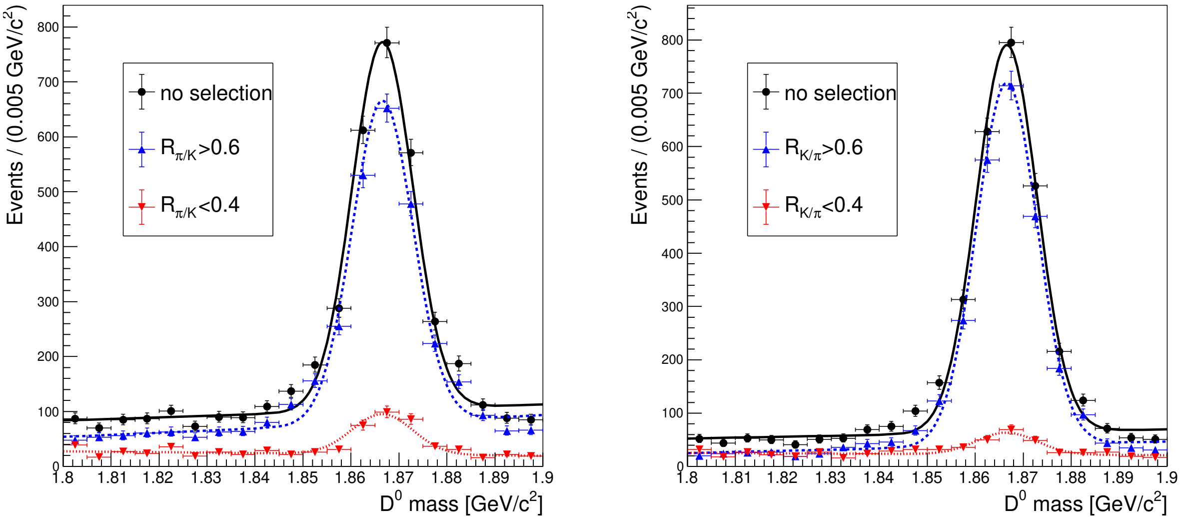

(a) π tracks (Data)

(b) K tracks (Data)

FIGURE 6.8: Distribution of D^0 mass using data before and after applying $R_{\pi/K}(R_{K/\pi})$ cut for (a) π track and (a) K track. Black solid, blue dashed and red dotted curves are fitting curve for each D^0 mass distribution.

TABLE 6.2: Comparison of overall performance between data and MC.

	K eff.	π mis.	π eff.	K mis.
Data	93.5 ± 0.6 %	10.9 ± 0.9 %	87.5 ± 0.9 %	5.6 ± 0.3 %
MC	96.7 ± 0.2 %	7.9 ± 0.4 %	91.3 ± 0.3 %	3.4 ± 0.4 %

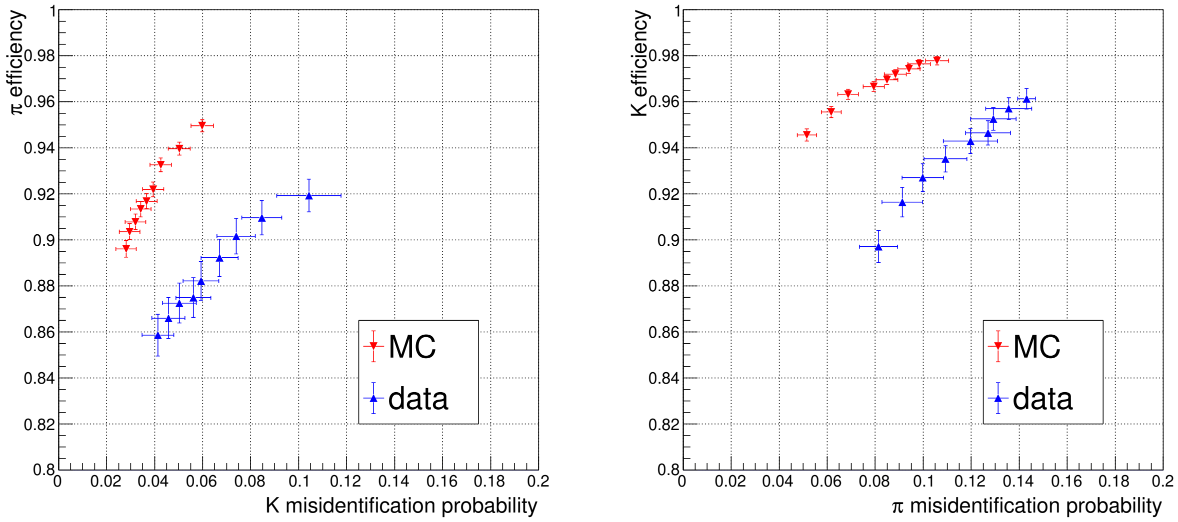

(a) π eff. versus K mis.

(b) K eff. vesus π mis.

FIGURE 6.9: ROC curve for (a)π efficiency versus K misidentification probability and (b) K efficiency versus π misidentification probability

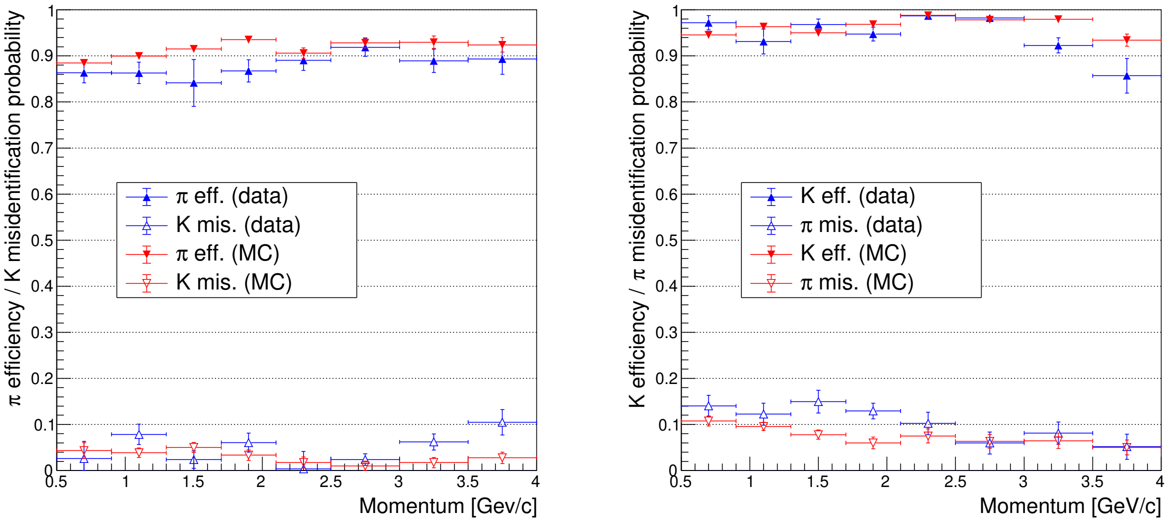

(a) π eff. and K mis.

(b) K eff. and π mis.

FIGURE 6.10: Distribution of efficiency and misidentification probability as a function of the momentum. (a)π efficiency and K misidentification probability. (b) K efficiency and π misidentification probability.

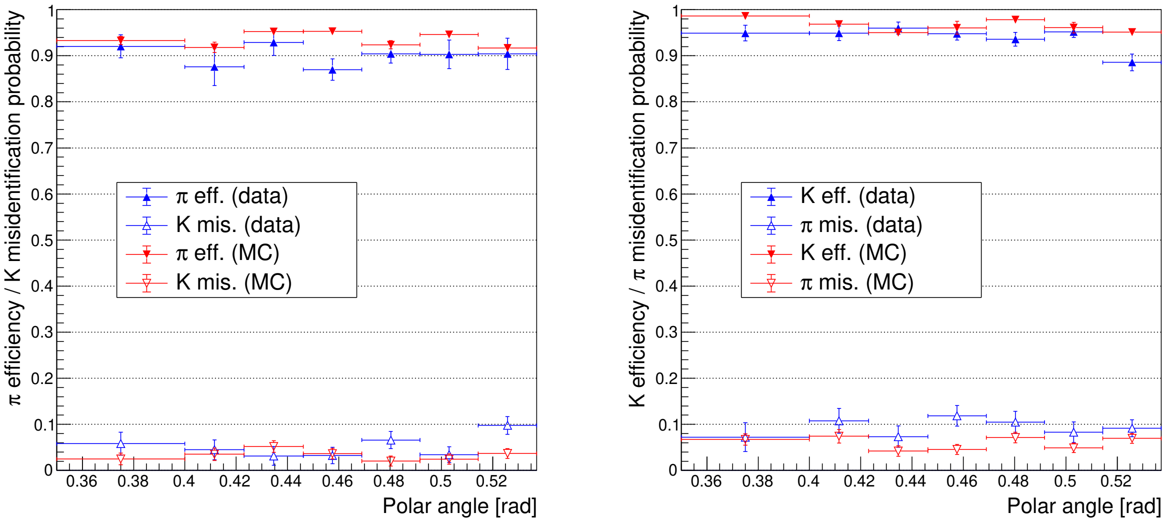

(a) π eff and K mis.

(b) K eff. and π mis.

FIGURE 6.11: Distribution of efficiency and misidentification probability as a function of the polar angle. (a)π efficiency and K misidentification probability. (b) K efficiency and π misidentification probability.

6.4 Comparison between Belle ACC and Belle II ARICH

A comparison of the PID performance between end-cap ACC (Belle) and ARICH (Belle II) is shown in Figure 6.12. The PID performance of end-cap ACC is dropped around 2.0 GeV/c. On the other hand, ARICH keeps good PID performance with momenta higher than 2.0 GeV/c which has been almost impossible at end-cap ACC. It proves that ARICH is working as a particle identification device at the end-cap region of the Belle II spectrometer as expected.

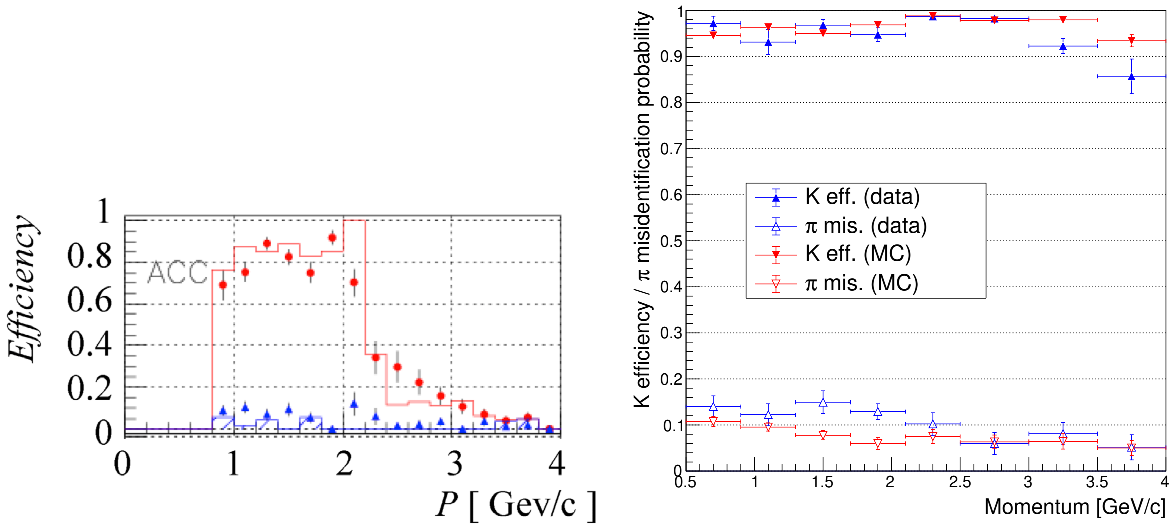

(a) end-cap ACC (b) ARICH

FIGURE 6.12: Comparison between (a) end-cap ACC and (b) ARICH for K efficiency and π misidentification probability. For (a), the lines and the markers show MC and data for K efficiency (red) and π misidentification probability (blue).

Chapter 7

A study of $B \to K^*\gamma$ decay

We search $B \to K^*\gamma$ decays using the first data set of the Belle II operation to demonstrate that the Belle II spectrometer and analysis software are properly working. The following three decay modes of $B \to K^*\gamma$ are used (charged-conjugated mode is always implied):

- $B^0 \to K^{*0}(\to K^+\pi^-)\gamma$
- $B^+ \to K^{*+}(\to K^+\pi^0)\gamma$
- $B^+ \to K^{*+}(\to K^0_S\pi^+)\gamma$

In this chapter, I describe the analysis method to search $B \to K^*\gamma$ decays at Belle II.

7.1 Event selection

The above three decay modes are reconstructed as the following flows:

Reconstruction of $B^0 \to K^{*0}(\to K^+\pi^-)\gamma$

K^{*0} candidates are reconstructed from pairs of K^+ and π^- candidates. B^0 candidates are reconstructed from pairs of K^{*0} and γ candidates.

Reconstruction of $B^+ \to K^{*+}(\to K^+\pi^0)\gamma$

K^{*+} candidates are reconstructed from pairs of K^+ and π^0 candidates. B^+ candidates are reconstructed from pairs of K^{*+} and γ candidates.

Reconstruction of $B^+ \to K^{*+}(\to K^0_S\pi^+)\gamma$

K^{*+} candidates are reconstructed from pairs of K^0_S and π^+ candidates. B^+ candidates are reconstructed from pairs of K^{*+} and γ candidates.

To reconstruct those three decay modes, we select particles: prompt γ, $\pi^\pm$, $K^\pm$, π^0, K^0_S, $K^{*0,\pm}$, and $B^{0,\pm}$. Multiple candidates can be reconstituted within an event. As multiple candidates are statistically correlated and one cannot treat them correctly, best candidate selection is performed to select one candidate in the event.

7.1.1 Selection of prompt γ candidates

To suppress $e^+e^- \to q\bar{q}(q = u, d, s, \text{and}, c)$ events and to suppress low energy photons from π^0, we require a criterion on the energies of the gamma candidates in CMS. The distribution of the energies of gamma candidates in CMS is shown in Figure 7.1(a). We require the energy to be in the range of $1.8\,\mathrm{GeV} < E^* < 3.0\,\mathrm{GeV}$. We also need to consider if a gamma candidate enters barrel ECL or end-cap ECL since the end-cap region receives a large number of gammas from beam background, and the energy spectrum of gammas becomes worse due to a large amount of material in front of the calorimeter. Figure 7.2 shows the distribution of ΔE for $B^0 \to K^{*0}(\to K^+\pi^-)\gamma$ decay obtained by the signal MC with applying all selection written in Table 7.5 except clusterReg, where definition of ΔE is written in Equation 7.2. From the fitting result, widths are $36.06 \pm 0.37\,[\mathrm{MeV}]$ and $56.98 \pm 2.0[\mathrm{MeV}]$ for the γ candidate reconstructed at barrel ECL and end-cap ECL, respectively. As a result, resolution of ΔE is directly affected by the energy resolution of gamma and we require clusterReg to be 2 (barrel) and exclude gamma candidates in end-cap.

To discriminate gamma candidates that make electromagnetic showers from hadron backgrounds that make hadron showers in ECL, we use three variables; the number of crystals in the cluster (clusterNHits), the ratio of the energy deposited in nine CsI crystals and 21 crystals (E_9/E_{21}), and the second moment of energy deposit distribution of a cluster (Second Moment). Figure 7.1(b)-(d) show distributions of clusterNHits, E_9/E_{21} and Second Moment for γ candidates from the combined MC of $B \to K^*\gamma$ signal and generic B-decay, respectively. To select gammas, we require clusterNHits ≥ 8, $E_9/E_{21} \geq 0.95$, and Second Moment ≤ 1.5.

To suppress gammas coming from π^0 and η decays, we use "π^0/η veto" package [83]. "π^0/η veto" uses invariant mass for low and high energy gamma candidate, zernikeMVA for low energy gamma candidate, polar angle for low energy gamma candidate, energy for low energy gamma candidate and distance between the track and low energy cluster. We require π^0 probability and η probability to be less than 0.87 and 0.97, respectively.

7.1.2 Charged K/π selection

For both $K^\pm$ and $\pi^\pm$ candidates, we require impact parameters $dr < 0.5\,\mathrm{cm}$, $|dz| < 2\,\mathrm{cm}$, and $nSVDHits \geq 6$ to keep quality of tracks. Furthermore, we require a PID variable that is obtained by combining informations of dE/dx of CDC, TOP, and ARICH as K probability$(K/\pi) > 0.6$ and π probability$(\pi/K) > 0.6$ for $K^\pm$ candidates and $\pi^\pm$ candidates, respectively.

7.1.3 π^0 selection

π^0 candidates are reconstructed from pairs of two γ candidates. For gamma candidates, we require $E_\gamma \geq 0.07\,\mathrm{GeV}$ for energy.

Figure 7.3 shows distributions of π^0 invariant mass from MC and real dada with a fitting curve. The fitting results are summarized in Table 7.1. The mean value of π^0 invariant mass is different from PDG value for real data, therefore, we require the difference from fitted mean value of π^0 mass to be less than $10\,\mathrm{MeV}/c^2$ for π^0 candidates. Specifically, we require the invariant mass to be in the range $0.1215 < M[\mathrm{GeV}/c^2] < 0.1415$.

Furthermore, the selection of cosine helicity angle (cosHelicityAngle, $\cos\theta_{\mathrm{hel}}$) is applied to select π^0 coming from B-meson decays. θ_{hel} is the angle between direction of a γ candidate and

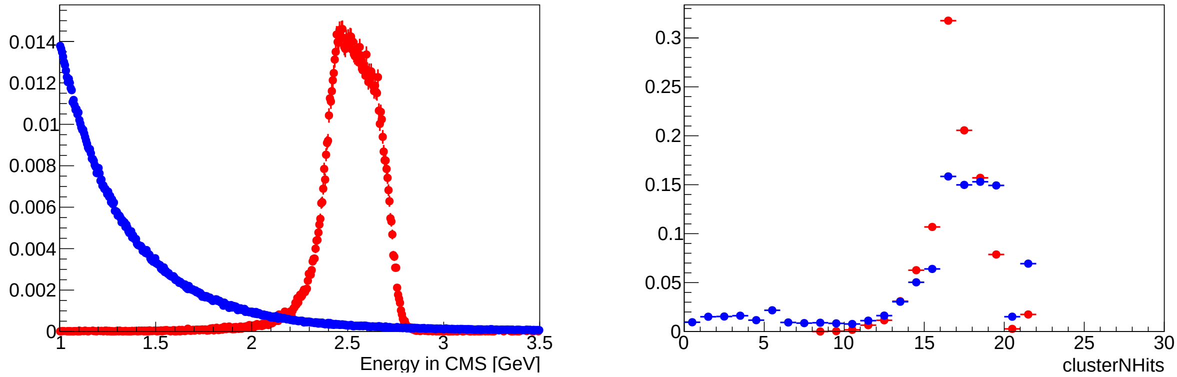

(a) Energy in CMS (b) clusterNHits

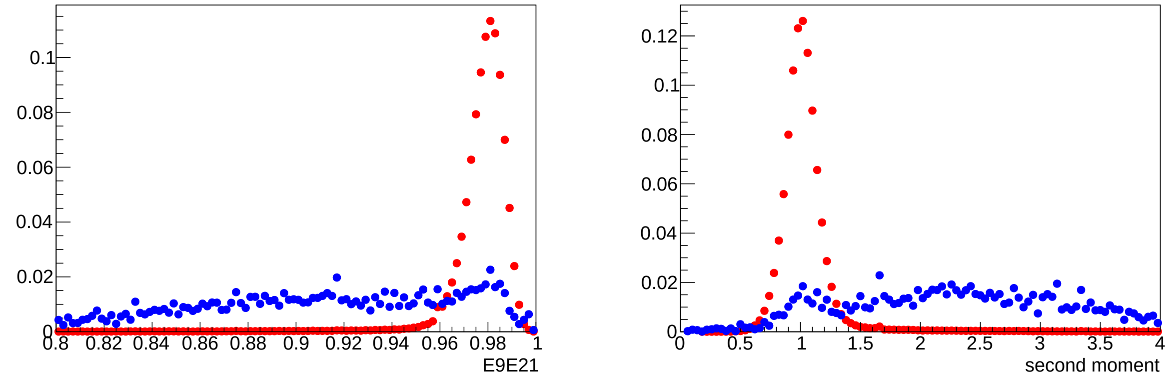

(c) E_9/E_{21} (d) Second Moment

FIGURE 7.1: Distributions of the gamma selection parameters from combined signal MC and generic MC. (a) the energy of gamma in CMS, (b) clusterNHits, (c) E_9/E_{21}, and (d) second moment. Red shows is prompt gamma from $B^0 \to K^{*0}(\to K^+\pi^-)\gamma$ decay, blue shows fake gamma. All histograms are normalized by number of entries.

the reversed direction of the K^* candidate in the $\gamma\gamma$ rest frame. Figure 7.4 shows the distribution of cosHelicityAngle of π^0 using generic MC and signal MC. π^0 is a scaler particle and the distribution of cosHelicityAngle should be flat. However, efficiency drops due to photon energy cut at around $|\cos\theta_{\text{hel}}| = 1$. On the other hand, distribution of $\cos\theta_{\text{hel}}$ is peaked at -1 and 1 for background, we require $|\cos\theta_{\text{hel}}| < 0.8$.

TABLE 7.1: Fitting result for π^0 invariant mass distribution.

	MC12	Data	PDG(2019)[84]
Mean (MeV/c^2)	132.8 ± 0.0083	131.5 ± 0.011	134.9770
Sigma (MeV/c^2)	4.9 ± 0.019	5.1 ± 0.0087	-

7.1.4 K^0_S selection

For K^0_S candidates, we require “goodBelleKShort” [85]. goodBelleKShort requires $0.4868 < M[\text{GeV}/c^2] < 0.528$ and the flag goodBelleKshort to be 1. The requirement of goodBelleKshort

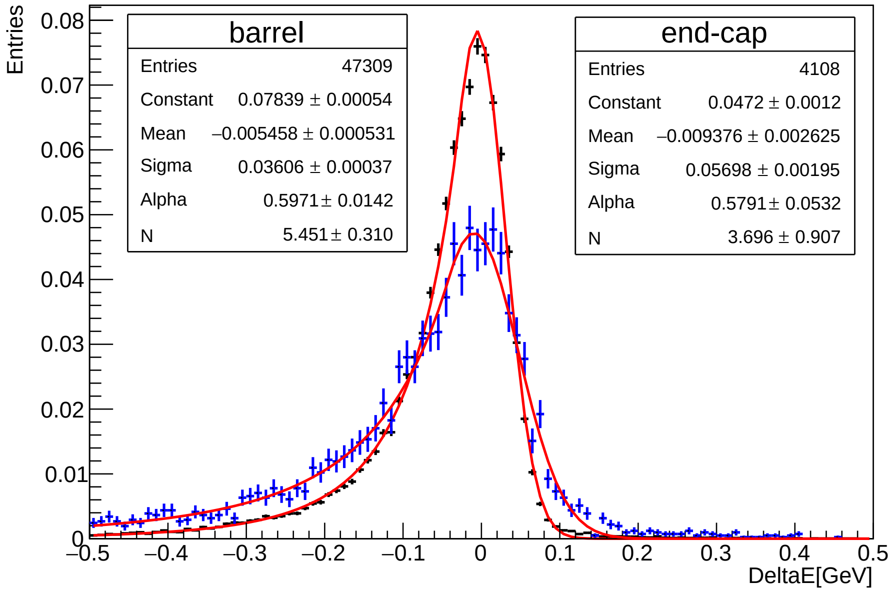

FIGURE 7.2: Distribution of ΔE for $B^0 \to K^{*0}\gamma \to K^+\pi^-\gamma$ mode from signal MC by applying all selection written in Table 7.5. Black histogram requires clusterReg to be 2 (barrel), blue histogram requires clusterReg to be 1 or 3 (end-cap). Red line for both histogram is fitting curve by crystal ball. Both histograms are normalized by number of entries.

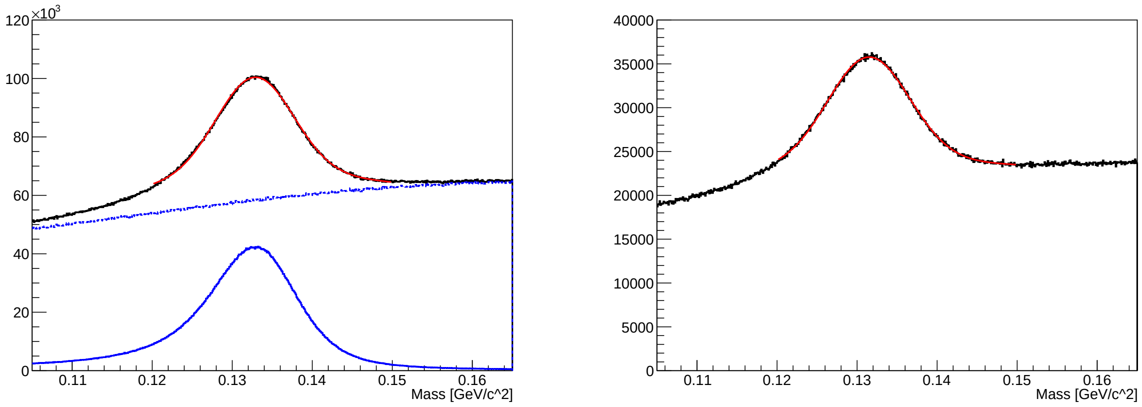

(a) generic MC

(b) data

FIGURE 7.3: Distribution of invariant mass of π^0 candidates from (a) generic MC and (b) data. We require $E_\gamma \geq 0.07\,\text{GeV}$ for energy for gamma candidates. Black histogram is all π^0 candidates, red histogram is true π^0 and blue histogram is fake π^0.

is listed in Table 7.2. goodBelleKshort uses four variables. *z_dist* is the distance between the two daughter tracks at their interception point. *dr* is the smallest approach from the IP to the two tracks in the x-y plane. $d\phi$ is the azimuthal angle between the momentum vector and the decay vertex vector of a K_S^0 candidate. *fl* is the flight length of the K_S^0 candidate in the x-y plane.

Figure 7.5 shows distributions of K_S^0 invariant mass from MC and real dada with a fitting

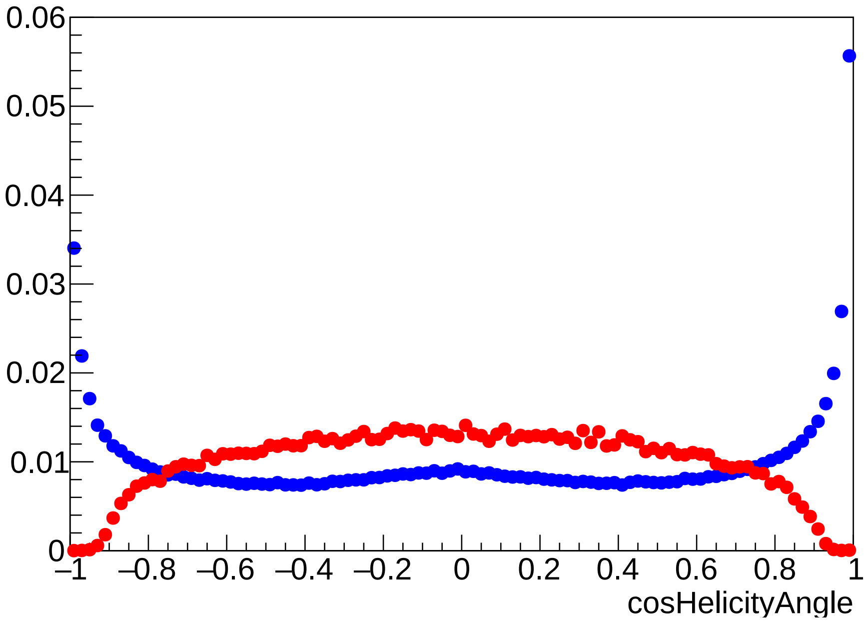

FIGURE 7.4: Distribution of cosHelicityAngle for π^0 from generic MC. We require $E_\gamma \geq 0.07\,\text{GeV}$ for energy for gamma candidates. Red histogram is true π^0, blue histogram is not π^0. Both histograms are normalized by the number of entries.

curve. The fitting results are summarized in Table 7.3. There is no large difference between fitted mean value and PDG value for K^0_S mass, therefore, we require the difference from the PDG value to be less than $10\,\text{MeV}/c^2$. Specifically, we require the invariant mass to be in the range $0.4876 < M[\text{GeV}/c^2] < 0.5076$.

TABLE 7.2: Requirement of goodBelleKshort.

Momentum[GeV/c]	z_dist	dr	$d\phi$	fl
<0.5	< 0.8	>0.05	<0.3	–
0.5 – 1.5	< 1.8	>0.03	<0.1	>0.08
>1.5	< 2.4	>0.02	<0.03	>0.22

7.1.5 Selection of K^*

K^{*0} candidates are reconstructed from pair of K^+ and π^- candidates. Figure 7.6 shows distributions of K^{*0} invariant mass from MC and real dada with a fitting curve. The fitting results are summarized in Table 7.4. There is no large difference between fitted value and PDG value for K^{*0} mass, therefore, we require the difference from PDG value to be less than $75\,\text{MeV}/c^2$. Specifically, we require the invariant mass to be in the range $0.8167 < M[\text{GeV}/c^2] < 0.9667$.

cosHelicityAngle selection is also applied to select K^* candidates coming from B-meson decays. θ_{hel} of K^* is the angle between the K direction and reversed direction of the B-meson in the $K\pi$ rest frame. Figure 7.8 shows the distribution of cosHelicityAngle of K^* using the MC of gereric B-meson decay and signal MC. K^* is coming from two body radiative decay of a scaler

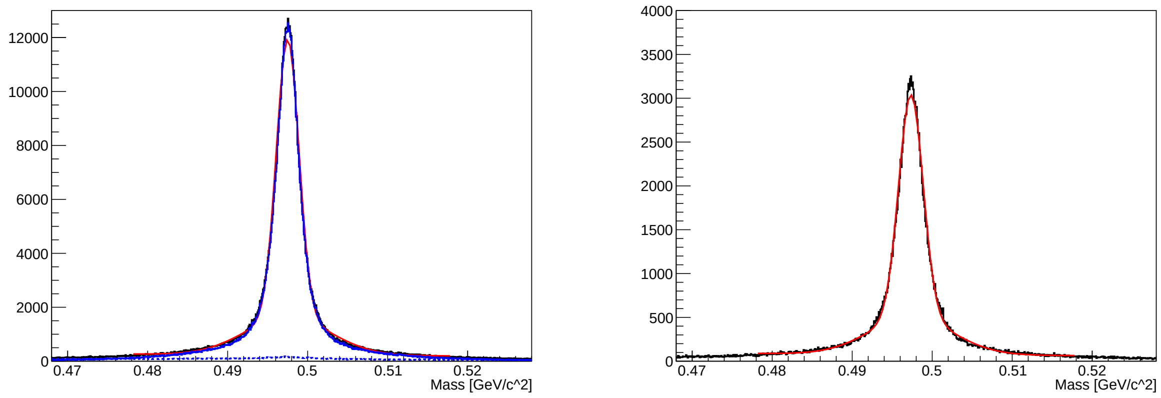

(a) generic MC (b) data

FIGURE 7.5: Distribution of invariant mass of K_S^0 candidates from (a) generic MC and (b) data. We require "goodBelleKShort". Black histogram is all K_S^0 candidates, red histogram is true K_S^0 and blue histogram is not K_S^0.

TABLE 7.3: Fitting result for K_S^0 mass distribution.

	MC12	Data	PDG(2019)[84]
Mean (MeV/c^2)	497.5 ± 0.0028	497.3 ± 0.0061	497.611
Sigma of larger gaussian (MeV/c^2)	1.4 ± 0.0041	1.5 ± 0.0097	-
Sigma of smaller gaussian (MeV/c^2)	5.3 ± 0.036	5.2 ± 0.069	-
Ratio of two gaussians	0.50	0.55	-

B-meson and the distribution of cosHelicityAngle should be $\sin^2\theta$ due to longitudinal polarization. Distribution of cosHelicityAngle of K^{*0} from $B^0 \to K^{*0}\pi^0$ and $B^0 \to K^{*0}\eta$ (transverse polarization of K^*) are shown in Figure 7.8. Excluding $|\cos\theta_{\text{hel}}| \sim 1$ is effective to suppress backgrounds that have almost same kinematics but polarization of K^*. We require $|\cos\theta_{\text{hel}}| < 0.8$.

TABLE 7.4: Fitting result for K^{*0} invariant mass distribution.

	MC12	Data	PDG(2019)[84]
Mean (MeV/c^2)	893.2 ± 0.18	891.4 ± 0.27	891.66
Sigma (MeV/c^2)	53.5 ± 0.95	49.3 ± 1.4	-

7.1.6 Selection of B

To select B-meson, we use two independent variables: beam energy constrained mass (M_{bc}) and the energy difference (ΔE). Both are defined as

$$M_{bc} = \sqrt{{E_{\text{beam}}^{cms}}^2 - |\vec{p}_B^{\,cms}|^2}, \tag{7.1}$$

$$\Delta E = E_B^{cms} - E_{\text{beam}}^{cms}, \tag{7.2}$$

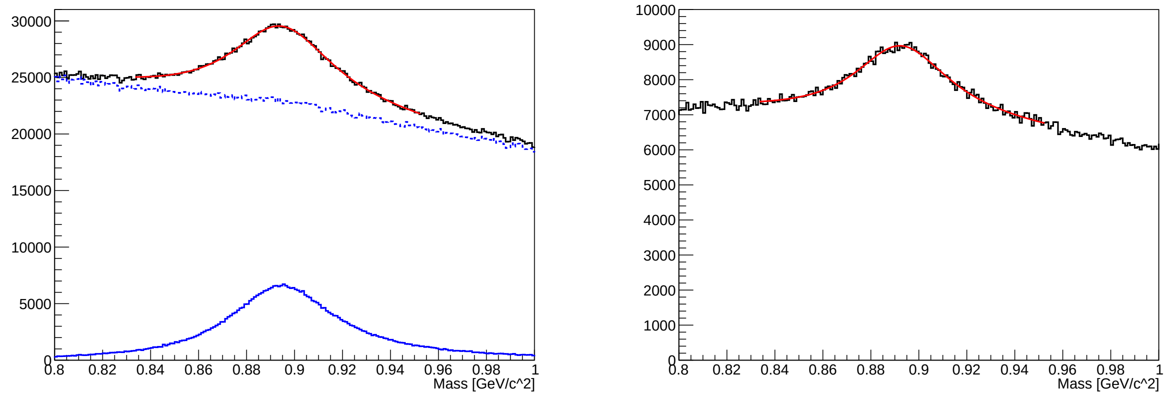

(a) generic MC

(b) data

FIGURE 7.6: Distribution of invariant mass of K^{*0} candidates from (a) generic MC and (b) data. For both $K^{\pm}$ and $\pi^{\pm}$ candidates, we require $dr < 0.5\,\mathrm{cm}$, $|dz| < 2\,\mathrm{cm}$, $nSVDHits \geq 6$, binary PID $K\,probability(K/\pi) > 0.6$ for $K^{\pm}$ candidates and $\pi\,probability(\pi/K) > 0.6$ for $\pi^{\pm}$ candidates. Black histogram is all K^{*0} candidates, red histogram is true K^{*0} and blue histogram is not K^{*0}.

where E^{cms}_{beam} is half of the center-of-mass energy, $\vec{p}^{\,cms}_B$ and E^{cms}_B are four momenta and energy of reconstructed B-meson candidates in the center-of-mass system. When B-meson is correctly reconstructed, values should be $\Delta E = 0$ and $M_{bc} = m_B(\sim 5.28\,\mathrm{GeV}/c^2)$. B-meson candidates are required to be in the ranges of $5.2\,\mathrm{GeV}/c^2 < M_{bc} < 5.29\,\mathrm{GeV}/c^2$ and $-0.5\,\mathrm{GeV} < \Delta E < 0.5\,\mathrm{GeV}$.

7.1.7 Summary of selection criteria

Selection criteria written in subsection 7.1.1 - 7.1.6 are summarized in Table 7.5. Signal box is defined as $5.27 < M_{bc}[\mathrm{GeV}/c^2] < 5.29, -0.2 < \Delta E[\mathrm{GeV}] < 0.08$, sideband is the region excluding signal box, and fitting region are $5.2 < M_{bc}[\mathrm{GeV}/c^2] < 5.29, -0.2 < \Delta E[\mathrm{GeV}] < 0.08$ [86].

TABLE 7.5: Selection criteria.

Particle	Selection
γ	$1.8 < E^*\,[\mathrm{GeV}] < 3.0, clusterReg == 2, clusterNHits \geq 8,$ $clusterE9E21 \geq 0.95, SecondMoment \leq 1.5\,[\mathrm{GeV}],$ $\pi^0\,probability < 0.87, \eta\,probability < 0.97$
$K^{\pm}$	$dr < 0.5\,[\mathrm{cm}], \lvert dz\rvert < 2\,[\mathrm{cm}], nSVDHits \geq 6,$ $K\,probability(K/\pi) > 0.6$
$\pi^{\pm}$	$dr < 0.5\,[\mathrm{cm}], \lvert dz\rvert < 2\,[\mathrm{cm}], nSVDHits \geq 6,$ $\pi\,probability(\pi/K) > 0.6$
π^0	$E_\gamma > 0.07\,[\mathrm{GeV}],$ $0.1215 < M[\mathrm{GeV}/c^2] < 0.1415, \lvert cosHelicityAngle\rvert < 0.8$
K^0_S	$goodBelleKshort, 0.4876 < M[\mathrm{GeV}/c^2] < 0.5076$
$K^{*0}/K^{*\pm}$	$0.8167 < M[\mathrm{GeV}/c^2] < 0.9667, \lvert cosHelicityAngle\rvert < 0.8$
$B^0/B^{\pm}$	$5.2 < M_{bc}[\mathrm{GeV}/c^2] < 5.29, -0.5 < \Delta E[\mathrm{GeV}] < 0.5$ signal box : $5.27 < M_{bc}[\mathrm{GeV}/c^2] < 5.29, -0.2 < \Delta E[\mathrm{GeV}] < 0.08$ fitting region : $5.2 < M_{bc}[\mathrm{GeV}/c^2] < 5.29, -0.2 < \Delta E[\mathrm{GeV}] < 0.08$

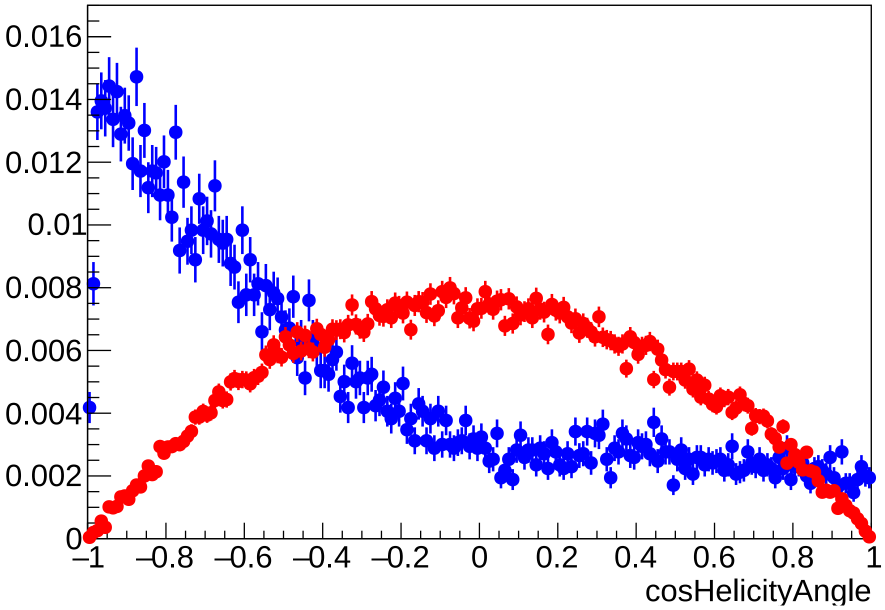

FIGURE 7.7: Distribution of cosHelicityAngle for K^{*} from combined both signal MC and generic MC. Red histogram is true K^{*} from $B \to K^{*}\gamma$ decay, blue histogram is not K^{*} and true K^{*} other than $B \to K^{*}\gamma$ decay. Both histograms are normalized by the number of entries.

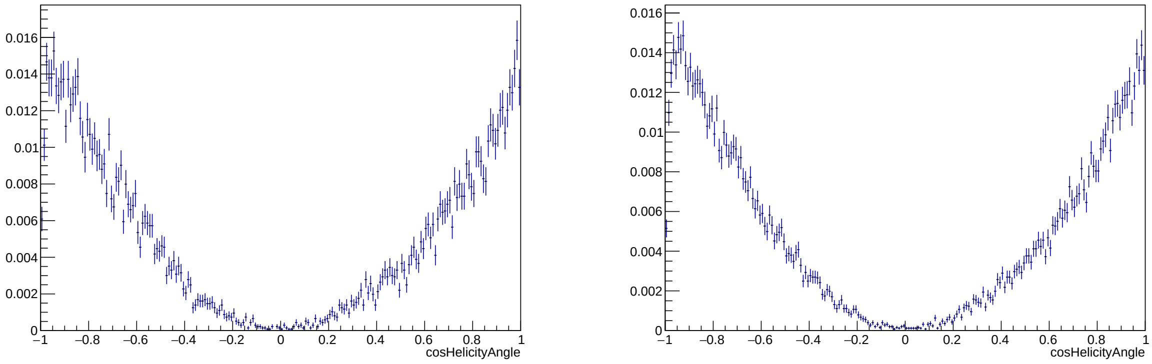

(a) $B^0 \to K^{*0}\pi^0$ mode (b) $B^0 \to K^{*0}\eta^0$ mode

FIGURE 7.8: Distribution of cosHelicityAngle of K^{*0} from signal MC for (a) $B^0 \to K^{*0}\pi^0$ mode and (b) $B^0 \to K^{*0}\eta^0$. The histograms is normalized by the number of entries.

7.1.8 Best candidate selection

Multiple candidates can be reconstructed in an event after all selection in above. Figure 7.9 shows the number of candidates in an event for using three decay modes with signal MC. The average value of the number of candidates in an event is 1.217, and 80.8 % of events have only one candidate in an event. We select a candidate that has the smallest $|\Delta E|$ value to select only one candidate in an event.

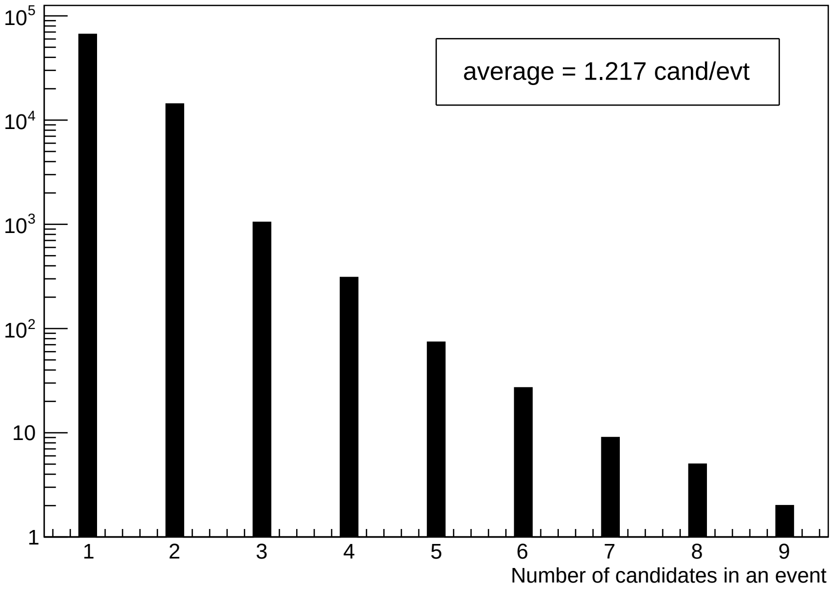

FIGURE 7.9: The distribution of the number of candidates in an event.

7.2 $q\bar{q}$ background suppression

The dominant background is a random combination of final state particles that comes from $e^+e^- \to q\bar{q}(q = u, d, s, \text{and}\, c)$ events. Those events are usually referred to as "continuum background". The cross section of continuum background is three times higher than B-meson pair production at the peak of $\Upsilon(4S)$ resonance, and it is important to suppress continuum background.

The event shape is mainly used to suppress continuum backgrounds. B-meson is almost rest in the center-of-mass system and the spin of B-meson is 0, therefore, the event shape of B-meson decay is spherical. On the other hand, the quarks from continuum backgrounds have a large momentum since the produced pair of light quarks $(u, d, s, \text{and}\, c)$ is energetic and make many hadrons along the direction of them, and its event shape is jet-like. The event shapes of B-meson decay and continuum background are shown in Figure 7.10.

Multi-Variate Analysis (MVA) with the Fast Boosted Decision Tree (FastBDT) method [87] is used for continuum suppression. The detail of the input parameters is written in the following.

Kakuno Super Fox-Wolfram (KSFW)

$$KSFW = \sum_{l=0}^{4} R_l^{so} + \sum_{l=0}^{4} R_l^{oo} + \gamma \sum_{n=1}^{N_t} |(P_t)_n|, \tag{7.3}$$

where R_l^{so} and R_l^{oo} are modified Fox-Wolfram moment explained in the following sentence, P_t the transverse momentum, γ is a Fisher coefficient, and N_t is the total number of particles. s and o donate daughter of Bcandidate and rest of event (ROE), respectively. R_i^{so} and R_i^{oo} are divided into two cases, odd and even, depending on l.

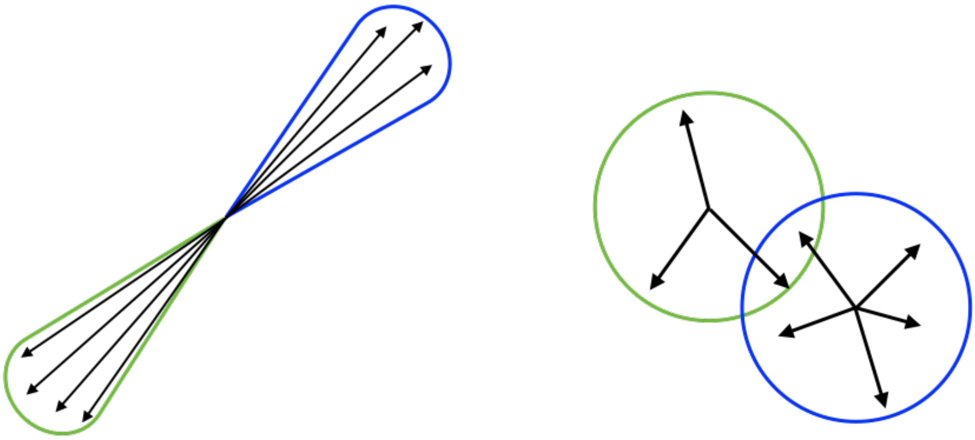

FIGURE 7.10: Event shapes of continuum (left) and B-meson decay (right).

R_l^{so}

Particles are divided into three categories: charged particle (c), neutral particle (n), and missing particle (m). Here, missing momentum is treated as an additional particle and R_l^{so} is defined as

$$R_l^{so} = \frac{\alpha_{cl} H_{cl}^{so} + \alpha_{nl} H_{nl}^{so} + \alpha_{ml} H_{ml}^{so}}{E^*_{\text{beam}} - \Delta E}, \tag{7.4}$$

where α_{cl}, α_{nl}, and α_{ml} are Fisher coefficients If l is odd,

$$H_{nl}^{so} = H_{ml}^{so} = 0, \tag{7.5}$$

$$H_{cl}^{so} = \sum_i \sum_{jx} Q_i Q_{jx} |p_{jx}| P_l(\cos\theta_{i,jx}), \tag{7.6}$$

where i is the daughter particle of Bcandidate, j is the particle in ROE, x is a category of the particle ($x = c, n, m$), Q_i and Q_{jx} are charges of the particle i and jx, p_{jx} is a momentum of particle jx, P_l is l-th Legendre polynomial, and $\theta_{i,jx}$ is the angle between particles i and jx. If l is even,

$$H_{xl}^{so} = \sum_i \sum_{jx} |p_{jx}| P_l(\cos\theta_{i,jx}), \tag{7.7}$$

which is similar to Equation 7.6. There are two free parameters for odd l (=1,3) and nine free parameters for even l, multiplied by three even l (=0,2,4) and three categories ($x = c, n, m$).

R_l^{oo}

If l is odd,

$$R_l^{oo} = \sum_j \sum_k \beta_l Q_j Q_k |p_j||p_k| P_l(\cos\theta_{ij,k}),, \tag{7.8}$$

where j and k are particles in ROE, β is the Fisher coefficient, and other variables are same as above. If l is even,

$$R_l^{oo} = \sum_j \sum_k \beta_l |p_j||p_k| P_l(\cos\theta_{ij,k}),. \tag{7.9}$$

There are five free parameters for coefficient β_l (l=0,1,2,3,4).

Available KSFW moments can be defined as

$$\begin{aligned} \mathrm{hso}xl &= \frac{H^{so}_{xl}}{H^{\max}_0}, && (7.10)\\ \mathrm{hoo}l &= \frac{H^{oo}_{xl}}{H^{\max}_0}, && (7.11) \end{aligned}$$

where $x = 0, 1, 2(= c, n, m)$, $l = 0, 1, 2, 3, 4$, and $H^{\max}_0 = 2(E - \Delta E)$ for normalization to not depend on ΔE. Since γ is used as signal particle, six variables hso$x$1, hso$x$3 equal to zero and not used. 14 KSFW moments listed in Table 7.6 are used.

Missing mass squared

To improve the background suppression, all Fisher coefficients are optimized for seven missing mass squared (mm2) bins since the KSFW is strongly correlated with it. The missing mass squared is defined as

$$M^2_{\mathrm{miss}} = \left(E_{\Upsilon(4S)} - \sum_{n=1}^{N_t} E_n \right)^2 - \sum_{n=1}^{N_t} |p_n|^2, \tag{7.12}$$

where $E_{\Upsilon(4S)}$ is the energy of $\Upsilon(4S)$, E_n and p_n are the energy and momentum of the reconstructed particle n, respectively, and N_t is the number of a total number of reconstructed final state particles. mm2 is used as input of FastBDT training.

Thrust variables

Thrust variables represent the event shape. The Thrust axis $\vec{n_T}$ is defined as the unit vector along the total projection of the collection of N momenta $\vec{p_i}$ is maximal. The thrust T is defined as

$$T = \max \frac{\sum_{i=1}^{N} |\vec{n_T} \cdot \vec{p_i}|}{\sum_{i=1}^{N} |\vec{p_i}|}. \tag{7.13}$$

Two thrust values of Bcandidate (ThrustB) and the rest of the event (ThrustO) are obtained.

One of the useful variables is CosTBTO, the absolute value of the cosine angle between the axis of ThrustB and ThrustO. Particles that come from B-meson decay are isotropically distributed since the B-meson is produced almost at rest in the $\Upsilon(4S)$ frame. Thus, the thrust axis of $B$is randomly distributed. Conversely, particles come from $e^+e^- \to q\bar{q}$ follow their jet-like structure and the thrust axis is directional. Therefore, CosTBTO is uniformly distributed for $B$and peaked at a large value. Another related value is CosTBz, the absolute value of the cosine angle between the axis of ThrustB and the z axis (beam axis). It has a similar trend with CosTBTO, uniformly distributed for B-meson decay, while $e^+e^- \to q\bar{q}$ follows 1+CosTBz^2. We use ThrustO, CosTBTO, and CosTBz as input parameter.

CLEO Cone

The CLEO collaboration used variables of the sum of absolute values of the momentum of all particles separated by the thrust axis in an interval of 10° [88]. The cone is merged with the respective cone in the opposite, resulting in nine concentric cones are obtained. For this analysis, we calculate it from only ROE particles.

Momentum in center-of-mass system

The angle θ_B between Bcandidate and the beam axis is useful to discriminate Bsignal and continuum background. Since the spin-1 $\Upsilon(4S)$ decays into two spin-0 B-meson, the distribution of θ_B follows $\sin\theta_B$ with respect to the beam axis. On the other hand, $e^+e^- \to q\bar{q}$ event has momentum in the direction of the beam axis, however, θ_B is uniformly distributed since fake B-meson candidates are reconstructed from random combination of particles. We use $\cos\theta_B$ as an input parameter of FastBDT.

The list of used variables

The variables used as the input of FastBDT are listed in Table 7.6.

TABLE 7.6: The list of variables used as the input of FastBDT.

Variables	Explanation
hso00, hso02, hso04, hso10, hso12, hso14, hso20, hso22, hso24, hoo0, hoo1, hoo2, hoo3, hoo4	14 variables of KSFW moments calculated using K^* and γ as signal side
mm2	missing mass squared
ThrustO	magnitude of Thrust of the rest of event
CosTBTO	absolute value of cosine angle between the axis of ThrustB and ThrustO
CosTBz	absolute value of cosine angle between the axis of ThrustB and the beam axis
cc1_CcROE, cc2_CcROE, cc3_CcROE, cc4_CcROE, cc5_CcROE, cc6_CcROE, cc7_CcROE, cc8_CcROE, cc9_CcROE	nine CLEO Cone variables calculated from particles remaining in the rest of the event
useCMSFrame__bocosTheta__bc	cosine angle between the momentum of signal side B in the CMS and the beam axis

7.2.1 Training of FastBDT

FastBDT is trained using one million events of signal MC as signals, and the 2/3 of the continuum MC corresponding to the integrated luminosity of 266.6 fb^{-1} as backgrounds. All selections listed in subsection 7.1.6 are required before training. The training is performed $B^0 \to K^{*0}\gamma$ mode and $B^+ \to K^{*+}\gamma$ mode, separately. The correlations of input parameters for FastBDT training are shown in Figure 7.11.

The output values is ranged between 0 to 1. The signal like events are concentrated near 1 and the background like events are concentrated near 0. Figure 7.12 shows outputs of FastBDT for $B^0 \to K^{*0}\gamma$ and $B^+ \to K^{*+}\gamma$ using signal MC, continuum MC, and generic B MC.

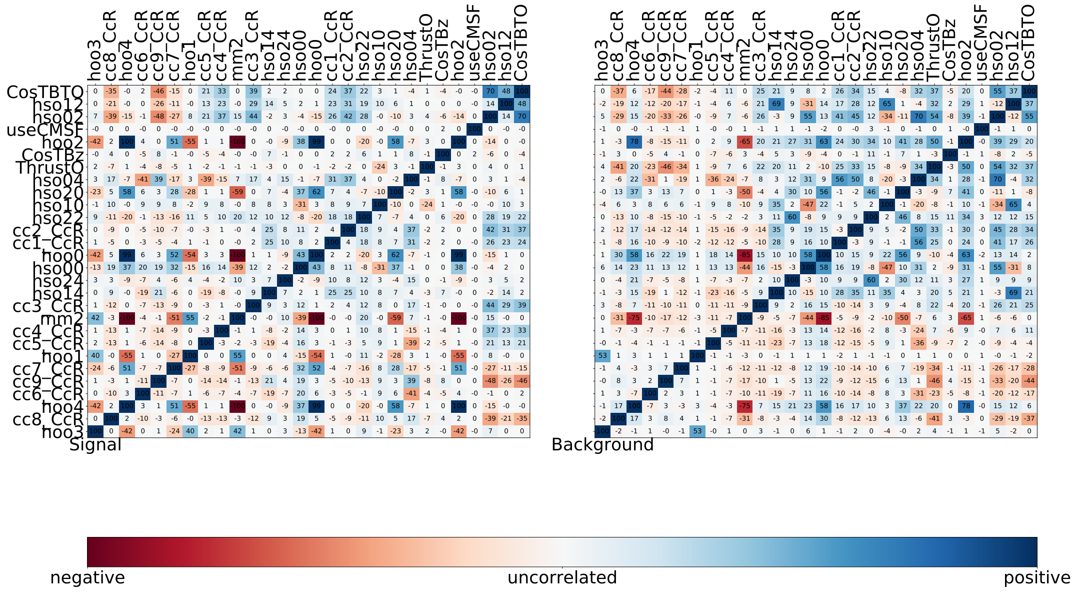

(a) $B^0 \to K^{*0}\gamma$

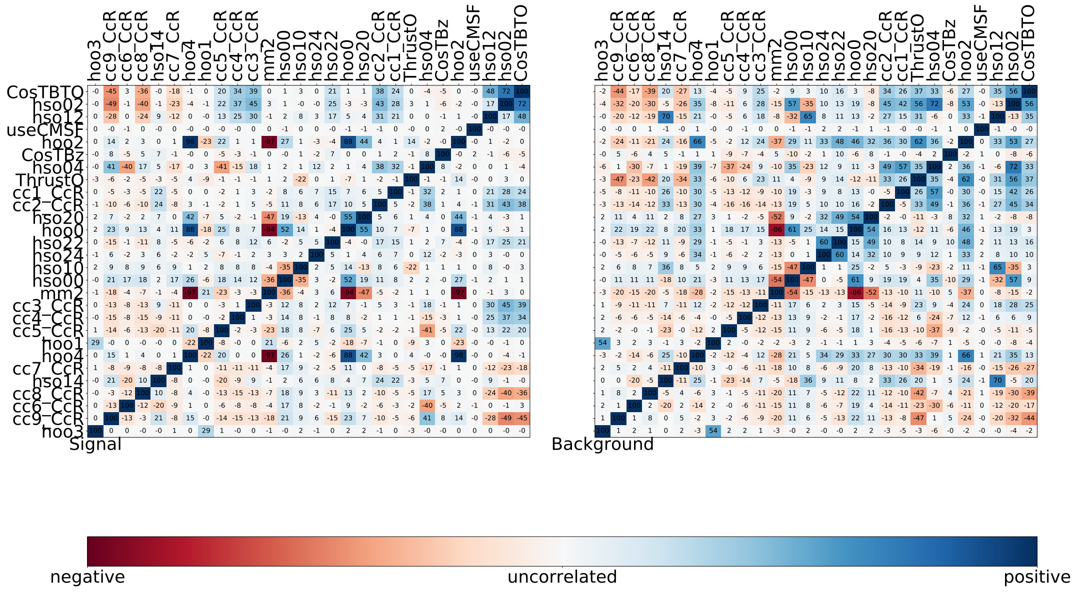

(b) $B^+ \to K^{*+}\gamma$

FIGURE 7.11: Correlation FastBDT training. (a) $B^0 \to K^{*0}\gamma$ and (b) $B^+ \to K^{*+}\gamma$. Left is signal and right is background.

7.2.2 Definition of the cut value of FastBDT

The cut value of the FastBDT is determined by calculating the Figure of Merit (FOM) given by $S/\sqrt{S+B}$ where S and B are numbers of signals and backgrounds in the signal box, respectively. For calculating the FOM, we use signal MC and continuum MC that are statistically independent of those used for the training of the FastBDT, and generic BMC that is not used for the training. We calculate the FOM for the integrated luminosity of 2.62 fb^{-1} by scaling the number of events. The FOM value as the function of the cut value of the FastBDT output is shown in

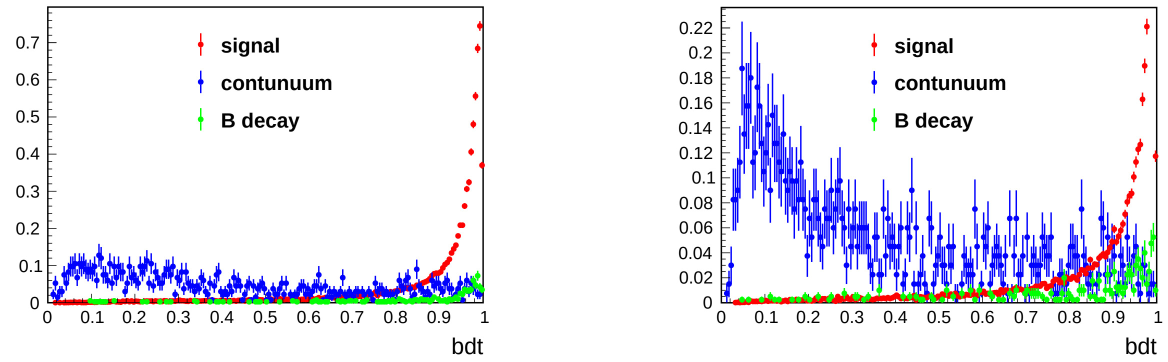

(a) $B^0 \to K^{*0}\gamma$

(b) $B^+ \to K^{*+}\gamma$

FIGURE 7.12: BDT distributions for (a) $B^0 \to K^{*0}\gamma$ and (b) $B^+ \to K^{*+}\gamma$. Each distributions are normalized by integrated luminosity.

Fig. Figure 7.13. To suppress continuum events with maximizing FOM, we require bdt > 0.68 and bdt > 0.765 for $B^+ \to K^{*+}\gamma$ mode and $B^0 \to K^{*0}\gamma$ mode, respectively. 77.2 % of $e^+e^- \to q\bar{q}$ backgrounds are rejected with retaining 90.6 % of signal events for $B^0 \to K^{*0}(\to K^+\pi^-)\gamma$ mode. Table 7.7 summarizes the ratio of $e^+e^- \to q\bar{q}$ rejection and signal retainment for all decay modes.

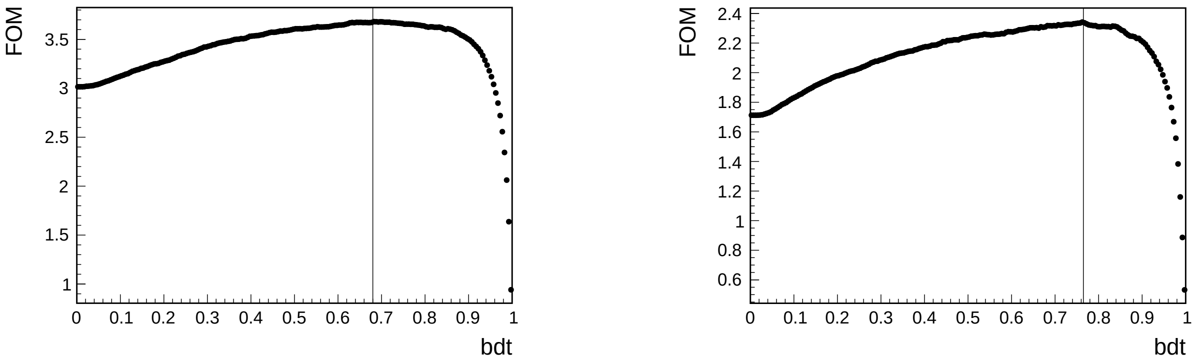

(a) $B^0 \to K^{*0}\gamma$

(b) $B^+ \to K^{*+}\gamma$

FIGURE 7.13: Figure of Merit as the function of the cut value of the FastBDT for (a) $B^0 \to K^{*0}\gamma$ mode and (b) $B^+ \to K^{*+}\gamma$ mode. FOM value is scaled to 2.62 fb^{-1}. The vertical line shows bdt value which has maximum significance.

TABLE 7.7: The ratio of $e^+e^- \to q\bar{q}$ rejection and signal retainment.

	$B^0 \to K^{*0}(\to K^+\pi^-)\gamma$	$B^+ \to K^{*+}(\to K^+\pi^0)\gamma$	$B^+ \to K^{*+}(\to K^0_S\pi^+)\gamma$
Signal keep	90.6 %	82.1 %	80.8 %
$e^+e^- \to q\bar{q}$ reject	77.2 %	87.2 %	88.0 %

7.3 Peaking and higher resonance background

There are two kinds of background from B-decay: peaking background and higher resonance background. The peaking background comes from $B \to K^*\pi^0$ and $B \to K^*\eta$ since one γ that comes from π^0 or η decay is missed and the other γ may be reconstructed as prompt if it is the γ from B-decay. The higher resonance background comes from $B \to K_2^*\gamma$ since width of both K^* and K_2^* resonance are wide, and some events of $K_2^* \to K\pi$ is induced in the K^* peak region in $M_{K\pi}$ distribution. We use $B^0 \to K^{*0}\pi^0$ and $B^0 \to K^{*0}\eta$ as peaking backgrounds and $B^0 \to K_2^{*0}\gamma$ as higher resonance backgrounds for $B^0 \to K^{*0}(\to K^+\pi^-)\gamma$ mode, and $B^+ \to K^{*+}\pi^0$ and $B^+ \to K^{*+}\eta$ as peaking backgrounds and $B^+ \to K_2^{*+}\gamma$ as higher resonance backgrounds for $B^+ \to K^{*+}(\to K^+\pi^0)\gamma$ mode and $B^+ \to K^{*+}(\to K_S^0\pi^+)\gamma$ mode.

Those backgrounds are estimated with the same procedure written in above. We estimate the number of events that come from above peaking backgrounds and higher resonance backgrounds. Table 7.8, Table 7.9, and Table 7.10 summarize the expected number of events in the signal box and sideband region.

TABLE 7.8: Expected number of events for $B^0 \to K^{*0}(\to K^+\pi^-)\gamma$ from MC in signal box and sideband region. Use signal MC, peaking backgrounds MC ($B^0 \to K^{*0}\pi^0$ and $B^0 \to K^{*0}\eta$) and higher resonance backgrounds MC ($B^0 \to K_2^{*0}\gamma$). Number of remaining events is scaled into 2.62 fb^{-1}.

Region	Selection	Signal	$B^0 \to K^{*0}\pi^0$	$B^0 \to K^{*0}\eta$	$B^0 \to K_2^{*0}\gamma$
	Generated	79.82	10.05	44.90	35.17
Signal box	Reconstruction	21.03	0.05	0.20	0.03
Sideband	Reconstruction	2.01	0.03	0.40	0.33

TABLE 7.9: Expected number of events for $B^+ \to K^{*+}(\to K^+\pi^0)\gamma$ from MC in signal box and sideband region. Use signal MC, peaking backgrounds MC ($B^+ \to K^{*+}\pi^0$ and $B^+ \to K^{*+}\eta$) and higher resonance backgrounds MC ($B^+ \to K_2^{*+}\gamma$). Number of remaining events is scaled into 2.62 fb^{-1}.

Region	Selection	Signal	$B^+ \to K^{*+}\pi^0$	$B^+ \to K^{*+}\eta$	$B^+ \to K_2^{*+}\gamma$
	Generated	31.31	21.10	57.04	40.58
Signal box	Reconstruction	5.58	0.03	0.07	0.02
Sideband	Reconstruction	0.65	0.02	0.16	0.17

TABLE 7.10: Expected number of events for $B^+ \to K^{*+}(\to K_S^0\pi^+)\gamma$ from MC in signal box and sideband region. Use signal MC, peaking backgrounds MC ($B^+ \to K^{*+}\pi^0$ and $B^+ \to K^{*+}\eta$) and higher resonance backgrounds MC ($B^+ \to K_2^{*+}\gamma$). Number of remaining events is scaled into 2.62 fb^{-1}.

Region	Selection	Signal	$B^+ \to K^{*0}\pi^+$	$B^+ \to K^{*+}\eta$	$B^+ \to K_2^{*+}\gamma$
	Generated	31.36	21.10	57.04	40.58
Signal box	Reconstruction	4.95	0.03	0.07	0.01
Sideband	Reconstruction	0.48	0.02	0.14	0.15

7.4 Estimation of the number of events

I estimate the number of events in the signal box, sideband region and fitting region at the integrated luminosity of 2.62 fb^{-1} by scaling the number of events of MC samples to match the integrated luminosity. Using MC samples, we count the number of events after applying all selection.

To estimate the number of events, the branching fraction of $B^0 \to K^{*0}\gamma$ mode and $B^+ \to K^{*+}\gamma$ mode are assumed 4.18×10^{-5} and 3.92×10^{-5}, respectively [89]. In addition, the difference of the branching fraction between $\Upsilon(4S) \to B^0\bar{B}^0$ and $\Upsilon(4S) \to B^+B^-$ is taken into account. The branching fraction of $\Upsilon(4S) \to B^0\bar{B}^0$ and $\Upsilon(4S) \to B^+B^-$ is 0.486 ± 0.006 and 0.514 ± 0.006, respectively. To calculate the integrated luminosity which corresponds to the number of generated events, we assume the cross section of $e^+e^- \to \Upsilon(4S)$ process to be 1.1 nb. Therefore, 200k events which is used to estimate the number of signal for $B^0 \to K^{*0}\gamma$ mode and $B^+ \to K^{*+}\gamma$ mode correspond to $4.4 \times 10^3\,\mathrm{fb}^{-1}$ and $5.6 \times 10^3\,\mathrm{fb}^{-1}$, respectively. Then we obtain the expected number of events at $2.62\,\mathrm{fb}^{-1}$ by scaling the counted number of events by the ratio of target luminosity ($2.62\,\mathrm{fb}^{-1}$) and integrated luminosity corresponding to the generated events ($4.4 \times 10^3\,\mathrm{fb}^{-1}$ or $5,6 \times 10^3\,\mathrm{fb}^{-1}$). Table 7.11 summarizes the signal efficiency and the expected number of events in the signal box, sideband region and fitting region.

TABLE 7.11: Expected number of events for reconstruction and $q\bar{q}$ suppression for three decay modes from MC in signal box, sideband region, and fitting region. The number of events is scaled into 2.62 fb^{-1}. $B^0 \to K^{*0}\gamma$ is excluded from mixed and charged MC for $B^0 \to K^{*0}(\to K^+\pi^-)\gamma$ mode. $B^+ \to K^{*+}\gamma$ is excluded from mixed and charged MC for $B^+ \to K^{*+}(\to K^+\pi^0)\gamma$ mode and $B^+ \to K^{*+}(\to K_S^0\pi^+)\gamma$ mode. S and B are the number of events of signal and backgrounds components, respectively.

Mode	Region	Selection	Signal	Continuum	Mixed	Charged	Sum of backgrounds	Signal efficiency	$S/\sqrt{S+B}$	$S/\sqrt{B}$
$K^+\pi^-$		Generated	79.82	5.08×10^6	1.41×10^6	1.49×10^6	7.98×10^6	100.0%	-	-
	Signal box	Reconstruction	21.03	24.60	1.23	0.90	26.73	24.35%	3.04	4.07
		$q\bar{q}$ suppression	19.05	5.60	1.04	0.79	7.43	23.87%	3.70	6.99
	Sideband	Reconstruction	2.01	475.75	7.94	9.64	493.33	-	-	-
		$q\bar{q}$ suppression	1.76	130.57	6.90	8.28	145.75	-	-	-
	Fitting	Reconstruction	21.35	155.57	2.10	1.84	159.51	26.75%	-	-
		$q\bar{q}$ suppression	19.33	41.35	1.79	1.53	44.67	24.22%	-	-
$K^+\pi^0$		Generated	31.31	5.08×10^6	1.41×10^6	1.49×10^6	7.98×10^6	100.0%	-	-
	Signal box	Reconstruction	5.58	19.37	0.59	0.71	20.67	17.84%	1.09	1.23
		$q\bar{q}$ suppression	4.58	2.47	0.42	0.52	3.41	14.62%	1.62	2.48
	Sideband	Reconstruction	0.65	347.93	6.47	4.71	359.11	-	-	-
		$q\bar{q}$ suppression	0.52	52.72	4.64	3.38	60.74	-	-	-
	Fitting	Reconstruction	5.68	120.80	1.40	1.35	123.55	18.16%	-	-
		$q\bar{q}$ suppression	4.66	18.25	0.95	0.97	20.17	14.88%	-	-
$K_S^0\pi^+$		Generated	31.36	5.08×10^6	1.41×10^6	1.49×10^6	7.98×10^6	100.0%	-	-
	Signal box	Reconstruction	4.95	7.42	0.38	0.49	8.29	15.79%	1.36	1.72
		$q\bar{q}$ suppression	4.00	0.89	0.24	0.36	1.49	12.76%	1.71	3.28
	Sideband	Reconstruction	0.48	149.20	3.70	2.99	155.89	-	-	-
		$q\bar{q}$ suppression	0.38	25.31	2.70	2.22	30.23	-	-	-
	Fitting	Reconstruction	5.05	49.18	0.78	0.88	50.83	16.11%	-	-
		$q\bar{q}$ suppression	4.08	8.47	0.50	0.64	9.61	13.02%	-	-

Chapter 8

Search of $B \to K^*\gamma$ at Belle II

In this chapter, the method of signal yield extraction is described, and the results of $B \to K^*\gamma$ search at early stage of Belle II experiment are discussed.

8.1 Signal yield extraction

To extract the signal yield, we perform extended unbinned maximum likelihood fit to M_{bc} distribution using Roofit package. Since we use the value of $|\Delta E|$ for the best candidate selection, we do not use the distribution of $|\Delta E|$ to extract the signal yield. I use M_{bc} distribution that is obtained by applying $-0.2\,\mathrm{GeV} < \Delta E < 0.08\,\mathrm{GeV}$ and other all selections criteria except for the requirement of M_{bc}. I use crystal ball function and argus function for PDFs of signal and continuum background, respectively [90, 91]. The crystal ball function is defined as

$$f(x) = \frac{1}{\sigma \cdot \left(\frac{n}{|\alpha|}\frac{1}{n-1}\exp\left(-\frac{|\alpha|^2}{2}\right) + \sqrt{\frac{\pi}{2}}\left(1 + erf\left(\frac{|\alpha|}{2}\right)\right)\right)} \tag{8.1}$$

$$\cdot \begin{cases} \exp\left(-\frac{(x-\mu)^2}{2\sigma^2}\right), & \text{for } \frac{x-\mu}{\sigma} > -\alpha \\ \left(\frac{n}{|\alpha|}\right)^2 \exp\left(-\frac{|\alpha|^2}{2}\right) \cdot \left(\left(\frac{n}{|\alpha|} - |\alpha|\right) - \frac{x-\mu}{\sigma}\right)^{-n}, & \text{for } \frac{x-\mu}{\sigma} < -\alpha \end{cases} \tag{8.2}$$

where μ is mean, σ is width, α and n are tail parameters, and erf is error function.

The argus function is defined as

$$f(x) = x \cdot \sqrt{1 - \left(\frac{x}{m_0}\right)} \cdot \exp\left[c\left\{1 - \left(\frac{x}{m_0}\right)^2\right\}\right], \tag{8.3}$$

where m_0 is the end point, c is the shape parameter, respectively.

Figure 8.1 and Figure 8.2 show distributions of crystal ball function and argus function, respectively.

I use a function with combining crystal ball and argus functions to express peaking and higher resonance background components although the fraction of peaking and higher resonance backgrounds is less than 2%. Fitting parameters are summarized in Table 8.1.

We obtain parameters of PDFs (crystal ball function and argus function) by fitting to the M_{bc} distribution of signal MC and continuum MC, respectively. Figure 8.3 - 8.5 show fitting results using signal MC and continuum MC for $B^0 \to K^{*0}(\to K^+\pi^-)\gamma$, $B^+ \to K^{*+}(\to K^+\pi^0)\gamma$, and

$B^+ \to K^{*+}(\to K^0_S\pi^+)\gamma$, respectively. The shape parameters of PDFs obtained from the fit are shown in Table 8.2.

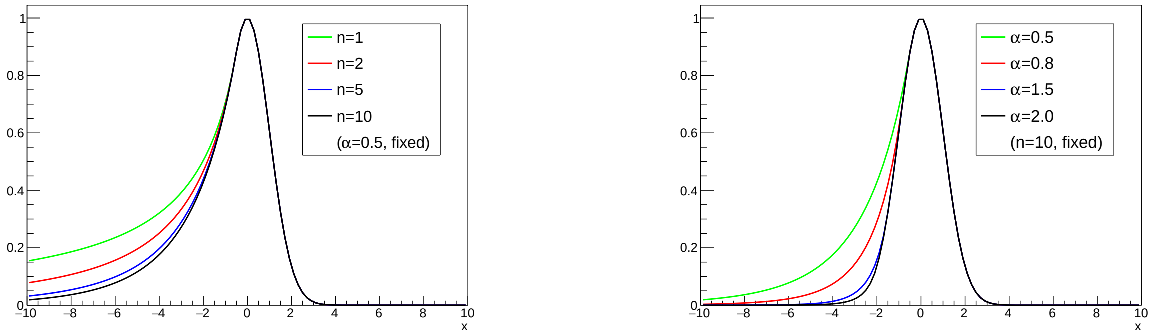

(a) varying n

(b) varying α

FIGURE 8.1: The crystal ball function distribution for verious (a) n and (b) α. σ and μ are fixed to be 0 and 1, respectively.

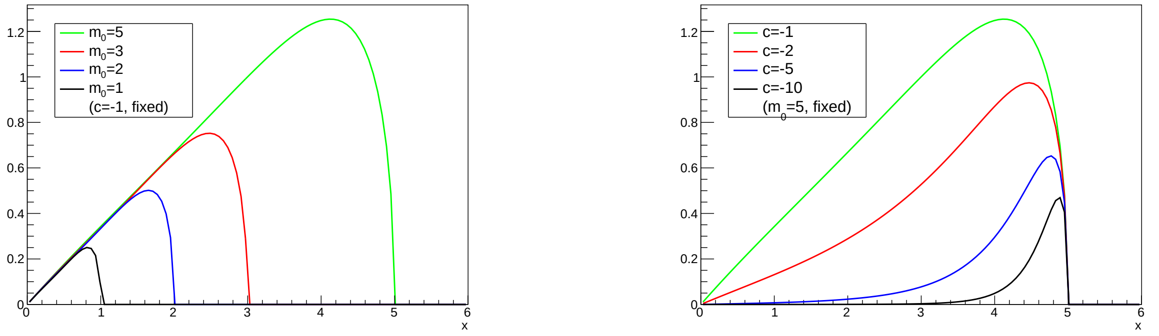

(a) varying m_0

(b) varying c

FIGURE 8.2: The argus function distribution for verious (a) m_0 and (b) c.

TABLE 8.1: Summary of fit function and its parameters.

Fit sample	Function	Parameter	Fit to real data	How to fix
Signal	Crystal ball	Mean	fix	$B \to D\pi$ decay of real data
		Width	fix	corrected MC value using real data
		Tail parameter α	fix	MC value
		Tail parameter n	fix	MC value
		Yield	float	-
Continuum	Argus	Shape parameter	float	-
		End point	fix	$B \to D\pi$ decay of real data
		Yield	float	-
Peaking and higher resonance background	Crystal ball	Mean	fix	MC value
		Width	fix	MC value
		Tail parameter α	fix	MC value
		Tail parameter n	fix	MC value
		Yield	fix	scaled MC value by luminosity
	Argus	Shape parameter	fix	MC value
		End point	fix	MC value
		Yield	fix	scaled MC value by luminosity

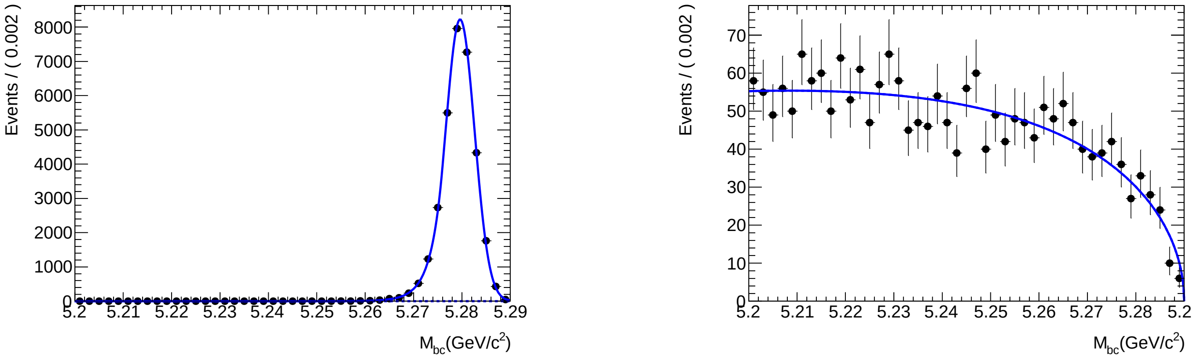

(a) signal MC

(b) continuum MC

FIGURE 8.3: Distributions of m_{bc} for (a) signal MC and (b) continuum MC for $B^0 \to K^{*0}\gamma \to K^+\pi^-\gamma$ mode. Blue line is the fit result.

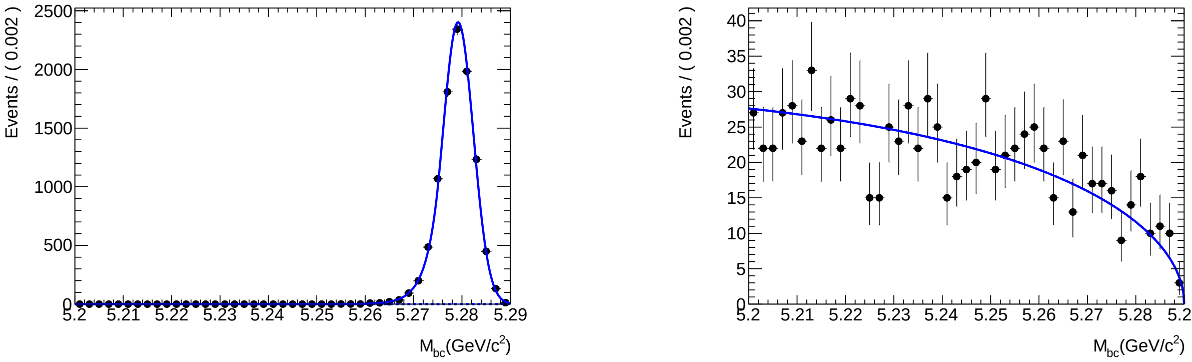

(a) signal MC

(b) continuum MC

FIGURE 8.4: Distributions of m_{bc} for (a) signal MC and (b) continuum MC for $B^+ \to K^{*+}\gamma \to K^+\pi^0\gamma$ mode. Blue line is the fit result.

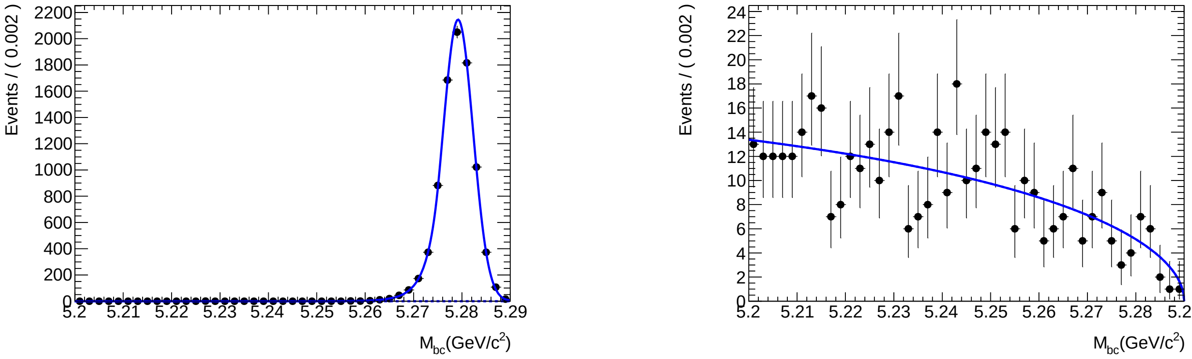

(a) signal MC

(b) continuum MC

FIGURE 8.5: Distributions of m_{bc} for (a) signal MC and (b) continuum MC for $B^+ \to K^{*+}\gamma \to K^0_S\pi^+\gamma$ mode. Blue line is the fit result.

TABLE 8.2: Shape parameters of PDFs.

Mode	MC type	Parameter	Value
$B^0 \to K^{*0}\gamma \to K^+\pi^-\gamma$	signal MC	mean	5.27962 ± 0.0000229 GeV/c^2
	signal MC	sigma	2.99082 ± 0.0185 MeV/c^2
	signal MC	tail parameter α	1.24037 ± 0.0286
	signal MC	tail parameter n	34.0049 ± 11.88
	continuum MC	argus shape	-15.78 ± 2.43
$B^+ \to K^{*+}\gamma \to K^+\pi^0\gamma$	signal MC	mean	5.27920 ± 0.000103 GeV/c^2
	signal MC	sigma	3.15429 ± 0.0641 MeV/c^2
	signal MC	tail parameter α	1.25876 ± 0.0504
	signal MC	tail parameter n	89.87 ± 137.88
	continuum MC	argus shape	-7.13 ± 6.59
$B^+ \to K^{*+}\gamma \to K_S^0\pi^+\gamma$	signal MC	mean	5.27920 ± 0.0000436 GeV/c^2
	signal MC	sigma	3.09420 ± 0.0352 MeV/c^2
	signal MC	tail parameter α	1.3159 ± 0.0617
	signal MC	tail parameter n	16.67 ± 6.37
	continuum MC	argus shape	-4.08 ± 5.4

8.1.1 Fixed parameters

Since the definition of M_{bc} contains the energy of the beam which is not simulated in the MC, we have to determine some fitting parameters using real data. The mean of crystal ball in the signal PDF and end point of argus in the background PDF are directly determined by a control sample $B \to D\pi$. The width of crystal ball in the signal PDF is corrected by $B \to D\pi$ mode and energy resolution of high energy gamma, and detail is written in the following subsections. Parameters of combined functions of crystal ball and argus for peaking and higher resonance background are fixed by MCs of those decay modes, and detail is written in the following subsections.

Fixed parameter using $B \to D\pi$ mode

We use control samples of $B^0 \to D^-\pi^+ \to K^+\pi^-\pi^-\pi^+$ mode for $B^0 \to K^{*0}(\to K^+\pi^-)\gamma$ mode and $B^+ \to \bar{D}^0\pi^+ \to K^-\pi^+\pi^+$ mode for $B^+ \to K^{*+}(\to K^+\pi^0)\gamma$ mode and $B^+ \to K^{*+}(\to K_S^0\pi^+)\gamma$ mode. The selection criteria are summarized in Table 8.3. We obtain parameters of PDFs by fitting to the M_{bc} distribution of $B \to D\pi$ candidates with assuming PDFs of signal events and continuum events as Gaussian and argus function, respectively. The fit is performend by floating all parameters.

Figure 8.6 shows fit result for $B^0 \to D^-\pi^+ \to K^+\pi^-\pi^-\pi^+$ mode from MC of generic B-decay that contain $B \to D\pi$ and real data, respectively. Figure 8.7 shows fit result for $B^+ \to \bar{D}^0\pi^+ \to K^-\pi^+\pi^+$ mode from generic MC and real data, respectively. The shape parameters of PDFs are summarized in Table 8.4 and Table 8.5 for before BDT selection and after BDT selection, respectively.

The mean of Gaussian for $B \to D\pi$ is highly correlated to the energy of the beam and is common to that of crystal ball function for $B \to K^*\gamma$. For $D\pi$ candidates after the BDT selection, we fit M_{bc} distribution and extract mean of Gaussian, which is used as a fixed parameter in the fit to M_{bc} distribution for $B \to K^*\gamma$. The average value of sigma of signal in the fit of $M_{\mathrm{bc}}$for

$B^0 \to D^-\pi^+ \to K^+\pi^-\pi^-\pi^+$ mode and $B^+ \to \bar{D^0}\pi^+ \to K^-\pi^+\pi^+$ mode after BDT selection is used to correct width of $M_{\rm bc}$ for $B \to K^*\gamma$ signal since beam energy spread has no difference between charged B-decays and neutral B-decays. In addition, the average value of end point in the fit of $M_{\rm bc}$ distribution for $B^0 \to D^-\pi^+ \to K^+\pi^-\pi^-\pi^+$ mode and $B^+ \to \bar{D^0}\pi^+ \to K^-\pi^+\pi^+$ mode before BDT selection is directly used as a fixed parameter in the fit of $M_{\rm bc}$ for $B \to K^*\gamma$ background, since beam energy spread has no difference between backgrounds of $B \to K^*\gamma$ and $B \to D\pi$.

TABLE 8.3: Selection criteria of $B^0 \to D^-\pi^+ \to K^+\pi^-\pi^-\pi^+$ and $B^+ \to \bar{D^0}\pi^+ \to K^-\pi^+\pi^+$.

Particle	Selection
$K^\pm$	$dr < 0.5$ [cm], $\lvert dz\rvert < 2$ [cm], $nSVDHits \geq 6$, $K\, probability(K/\pi) > 0.6$
$\pi^\pm$	$dr < 0.5$ [cm], $\lvert dz\rvert < 2$ [cm], $nSVDHits \geq 6$, $\pi\, probability(\pi/K) > 0.6$
D^0	$1.85 < M[\mathrm{GeV}/c^2] < 1.89, massKFit > 0.0$
$D^\pm$	$1.84 < M[\mathrm{GeV}/c^2] < 1.89, massKFit > 0.0$
$B^0/B^\pm$	$5.2 < m_{bc}[\mathrm{GeV}/c^2] < 5.29, -0.3 < \Delta E[\mathrm{GeV}] < 0.3$ FastBDT>0.68 for B^0 FastBDT>0.765 for $B^\pm$ signal box : $5.27 < m_{bc}[\mathrm{GeV}/c^2] < 5.29, -0.05 < \Delta E[\mathrm{GeV}] < 0.05$

TABLE 8.4: Shape parameters of PDFs after BDT selection from $B^0 \to D^-\pi^+ \to K^+\pi^-\pi^-\pi^+$ mode and $B^+ \to \bar{D^0}\pi^+ \to K^-\pi^+\pi^+$ mode using MC and real data.

Mode	Parameter	MC	Real data
$B^0 \to D^-\pi^+ \to K^+\pi^-\pi^-\pi^+$	mean [GeV]	5.27958 ± 0.0000474	5.28049 ± 0.000195
	sigma [MeV]	2.55119 ± 0.0435	2.55872 ± 0.149
	end point [GeV]	5.28986 ± 0.000113	5.28738 ± 0.000639
$B^+ \to \bar{D^0}\pi^+ \to K^-\pi^+\pi^+$	mean [GeV]	5.27921 ± 0.0000638	5.28023 ± 0.000213
	sigma [MeV]	2.56616 ± 0.0557	2.61842 ± 0.173
	end point [GeV]	5.28941 ± 0.000171	5.28785 ± 0.00112

TABLE 8.5: Shape parameters of PDFs AFTER BDT selection from $B^0 \to D^-\pi^+ \to K^+\pi^-\pi^-\pi^+$ mode and $B^+ \to \bar{D^0}\pi^+ \to K^-\pi^+\pi^+$ mode using MC and real data.

Mode	Parameter	MC	Real data
$B^0 \to D^-\pi^+ \to K^+\pi^-\pi^-\pi^+$	mean [GeV]	5.27957 ± 0.0000466	5.28036 ± 0.000195
	sigma [MeV]	2.58350 ± 0.0399	2.55655 ± 0.151
	end point [GeV]	5.28959 ± 0.000283	5.28784 ± 0.00169
$B^+ \to \bar{D^0}\pi^+ \to K^-\pi^+\pi^+$	mean [GeV]	5.27920 ± 0.0000666	5.28020 ± 0.000227
	sigma [MeV]	2.56199 ± 0.0515	2.65006 ± 0.175
	end point [GeV]	5.28850 ± 0.000399	5.28774 ± 0.00330

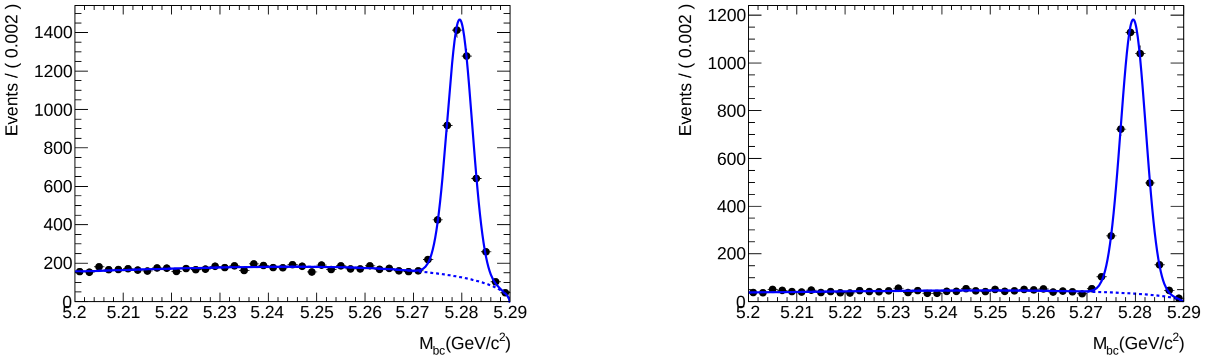

(a) MC before BDT selection

(b) MC after BDT selection

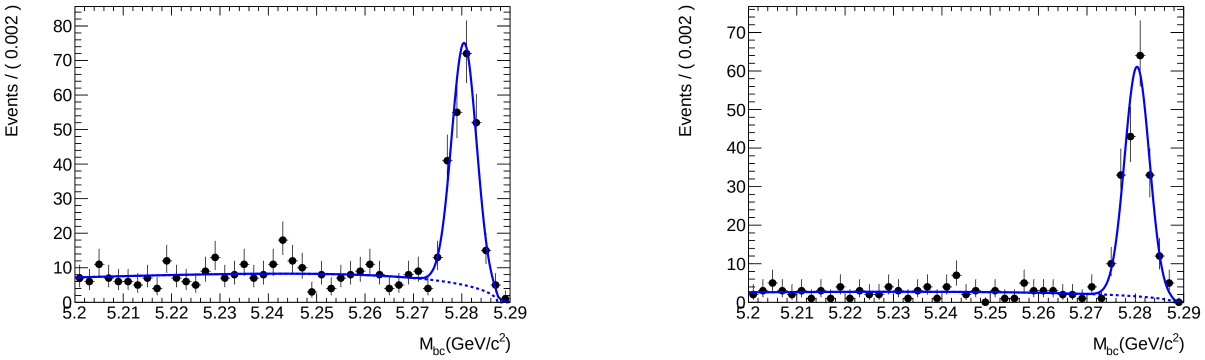

(c) Data before BDT selection

(d) Data after BDT selection

FIGURE 8.6: Distributions of M_{bc} using generic MC and real data for $B^0 \rightarrow D^-\pi^+ \rightarrow K^+\pi^-\pi^-\pi^+$ mode before/after BDT selection. Blue line is the fit result.

Correction of the width of crystal ball function to signal

The width of $B \rightarrow K^*\gamma$ has mainly determined by two sources: beam energy spread and energy leakage of high energy gamma. We use Equation 8.4 to correct the width. The derivation of the correction is written in A.1.

$$\begin{aligned} \sigma^2_{M_{bc}}(K^*\gamma; data) &= \sigma^2_{M_{bc}}(D\pi; data) \\ &+ \{\sigma^2_{M_{bc}}(K^*\gamma; MC) - \sigma^2_{E^*_{\text{beam}}}(D\pi; MC)\} \cdot \left(\frac{\sigma_{E_\gamma}(data)}{\sigma_{E_\gamma}(MC)}\right)^2, \end{aligned} \tag{8.4}$$

where $\sigma_{M_{bc}}$ and σ_{E_γ} are the width of M_{bc} distribution and variation of photon energy in the laboratory frame, respectively. Decay mode and data type are denoted in parentheses: $K^*\gamma$ is $B \rightarrow K^*\gamma$ mode, $D\pi$ is $B \rightarrow D\pi$ mode, $data$ is real data, and MC is MC. Ratio of $\sigma_{E_\gamma}(data)$ to $\sigma_{E_\gamma}(MC)$ is 1.001 ± 0.001 [92].

Fixed parameter for peaking and higher resonance background

Peaking and higher resonance backgrounds written in section 7.3 are included in fitting function with fixed shape parameters and yields. The used number of MC events is scaled by integrated luminosity to 1.175×10^5 fb^{-1} and 0.975×10^5 fb^{-1} for $B^0 \rightarrow K^{*0}\gamma$ and $B^+ \rightarrow K^{*+}\gamma$, respectively.

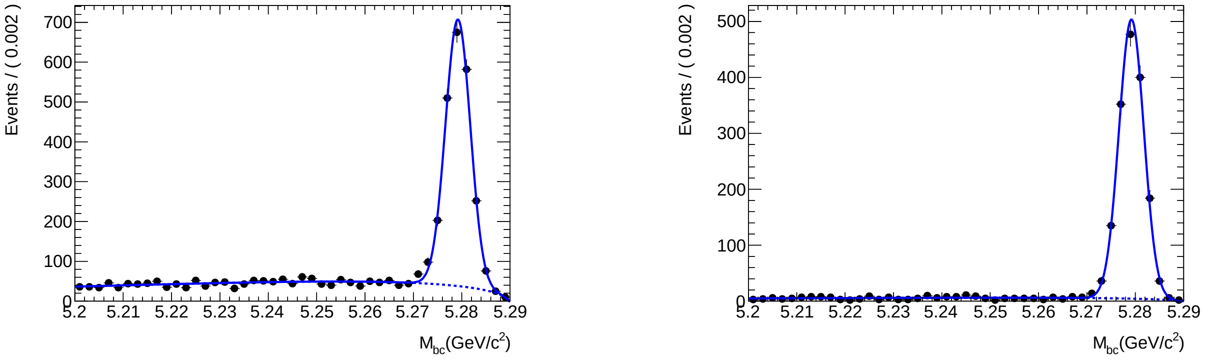

(a) MC before BDT selection (b) MC after BDT selection

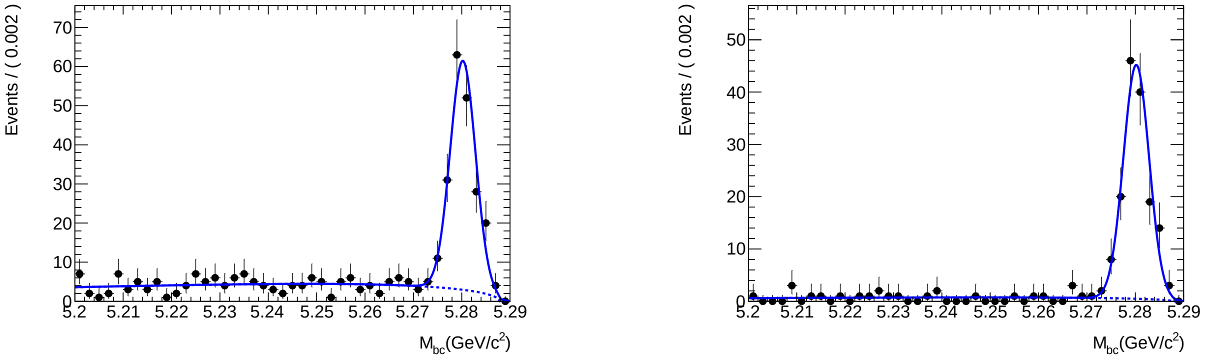

(c) Data before BDT selection (d) Data after BDT selection

FIGURE 8.7: Distributions of M_{bc} using generic MC and real data for $B^+ \to \bar{D}^0\pi^+ \to K^-\pi^+\pi^+$ mode before/after BDT selection . Blue line is the fit result.

To determine the parameters of the distribution, crystal ball function and argus function are used as a fitting function. M_{bc} distributions of peaking and higher resonance backgrounds with the fitting curve are shown in Figure 8.8. The fitting results are summarized in Table 8.6. Yields of crystal ball function and argus function are scaled to match to an integrated luminosity of 2.62 fb^{-1} when we fit M_{bc} distribution of $B \to K^*\gamma$ of real data.

8.1.2 Summary of fixed parameter

Table 8.7 summarize fixed and float parameters for the fit of the M_{bc} distribution for $K^*\gamma$ candidates in real data analysis. The errors of parameters are used to estimate the systematic uncertainty. The systematic uncertainties of tail parameter α and n of a crystal ball function are not estimated by the fitting error (detail is described in subsection 8.3.3) The peaking and higher resonance background are the same as tail parameter and detail is described in subsection 8.3.3.

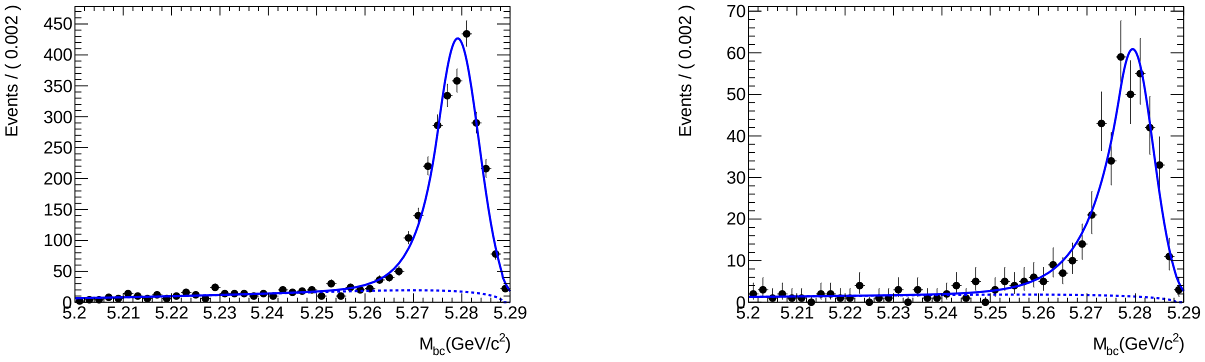

(a) $B^0 \to K^{*0}(\to K^+\pi^-)\gamma$ (b) $B^+ \to K^{*+}(\to K^+\pi^0)\gamma$

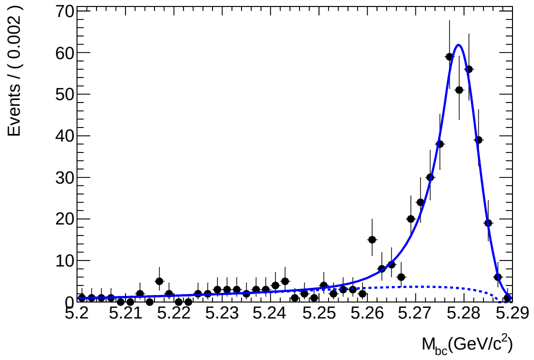

(c) $B^+ \to K^{*+}(\to K^0_S\pi^+)\gamma$

FIGURE 8.8: M_{bc} distribution of peaking and higher resonance backgrounds for $B^0 \to K^{*0}(\to K^+\pi^-)\gamma$, $B^+ \to K^{*+}(\to K^+\pi^0)\gamma$ and $B^+ \to K^{*+}(\to K^0_S\pi^+)\gamma$. Number of events for each modes are scaled to an integrated luminosity of $1.175 \times 10^5\text{fb}^{-1}$ for $B^0 \to K^{*0}(\to K^+\pi^-)\gamma$ mode and $0.975 \times 10^5\text{fb}^{-1}$ for $B^+ \to K^{*+}\gamma \to K^+\pi^0\gamma$ and $B^+ \to K^{*+}\gamma \to K^0_S\pi^+\gamma$ mode.

TABLE 8.6: Fitting results of peaking and higher backgrounds.

Function	Parameter	$K^+\pi^-\gamma$ (1.175×10^5 fb^{-1})	$K^+\pi^0\gamma$ (0.975×10^5 fb^{-1})	$K^0_S\pi^-\gamma$ (0.975×10^5 fb^{-1})
Crystal ball	Mean [GeV/c^2]	5.27819 ± 0.00019	5.27947± 0.00047	5.27889 ± 0.00046
	Width [MeV/c^2]	4.31469 ± 0.169	4.23063 ± 0.381	3.81359 ± 0.348
	Tail parameter α	0.959157 ± 0.104	0.645397 ± 0.124	0.700139 ± 0.150
	Tail parameter n	139.433 ± 0.047	103.666 ± 0.154	121.451 ± 1.201
	Yield	2410.75 ± 68.72	391.77 ± 28.27	337.21 ± 31.10
Argus	Shape parameter	-70.78 ± 9.85	-40.09 ± 32.93	-82.33 ± 26.82
	End point [GeV/c^2]	5.28850 ± 0.00027	5.28838 ± 0.00232	5.28701 ± 0.00056
	Yield	603.23 ± 53.99	69.46 ± 21.71	104.83 ± 27.10

TABLE 8.7: Fitting parameters with fixed value.

Fit sample	Function	Parameter	Fix/Float	Value		
				$K^+\pi^-$	$K^+\pi^0$	$K_0^S\pi^+$
Signal	Crystal ball	Mean $\left[\mathrm{GeV}/c^2\right]$	fix	5.28036 ± 0.000198	5.28020 ± 0.000227	5.28020 ± 0.000227
		Width $\left[\mathrm{MeV}/c^2\right]$	fix	3.022 ± 0.105	3.184 ± 0.117	3.124 ± 0.106
		Tail parameter α	fix	1.24037	1.25876	1.3159
		Tail parameter n	fix	34.0049	89.87	16.67
		Yield	float	-	-	-
Continuum	Argus	Shape parameter	float	-	-	-
		End point $\left[\mathrm{GeV}/c^2\right]$	fix	5.28762 ± 0.000645	5.28762 ± 0.000645	5.28762 ± 0.000645
		Yield	float	-	-	-
Peaking and higher resonance background	Crystal ball	Mean $\left[\mathrm{GeV}/c^2\right]$	fix	5,27819	5.27947	5.27889
		Width $\left[\mathrm{MeV}/c^2\right]$	fix	4.31469	4.23063	3.81359
		Tail parameter α	fix	0.959157	0.645397	0.700139
		Tail parameter n	fix	139.433	103.666	121.451
		yield	fix	0.5412	0.1117	0.0962
	Argus	Shape parameter	fix	-70.78	-40.09	-82.33
		End point $\left[\mathrm{GeV}/c^2\right]$	fix	5.28850	5.28838	5.28701
		Yield	fix	0.1354	0.0198	0.0299

8.2 Result

Figure 8.9 shows stacked M_{bc} distribution using $B^0 \to K^{*0}\gamma \to K^+\pi^-\gamma$, $B^+ \to K^{*+}\gamma \to K^+\pi^0\gamma$ and $B^+ \to K^{*+}\gamma \to K_S^0\pi^+\gamma$ modes. It has a clear peak at the mass of B-meson. Figure 8.10 shows the M_{bc} distribution with the fitting curve for each decay modes. From the fitting results, signal yields are

- $B^0 \to K^{*0}(\to K^+\pi^-)\gamma$ mode: 19.07 ± 5.2
- $B^+ \to K^{*+}(\to K^+\pi^0)\gamma$ mode: 9.81 ± 3.4
- $B^+ \to K^{*+}(\to K_S^0\pi^+)\gamma$ mode: 6.57 ± 3.1,

where the error is statistical only. The statistical significance of the signal is evaluated by the following formula:

$$\text{significance}^2 = -2 \cdot \log\left(L_{\max}/L_0\right) = -2 \cdot \left(logL_{\max} - logL_0\right) \tag{8.5}$$

where $L_{\max}$ and L_0 are likelihood value when the signal yield is floated and is fixed to zero, respectiely. Figure 8.11 shows M_{bc} distributions with the fitting curve when the signal yield is fixed to zero. Figure 8.12 shows the likelihood curves as a function of signal yield. Log likelihood value when the signal yield is fixed to zero and significance are summarized in Table 8.8 Significance is 4.42, 3.73, and 2.13 for $B^0 \to K^{*0}\gamma \to K^+\pi^-\gamma$, $B^+ \to K^{*+}\gamma \to K^+\pi^0\gamma$, and $B^+ \to K^{*+}\gamma \to K_S^0\pi^+\gamma$ mode, respectively. Combing all modes, the significance is 6.2. From this result, we (re-)observe $B \to K^*\gamma$ decays at the Belle II experiment.

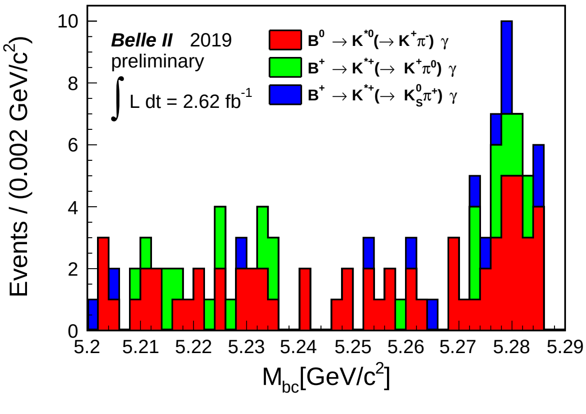

FIGURE 8.9: Stacked M_{bc} distribution using $B^0 \to K^{*0}(\to K^+\pi^-)\gamma$ mode, $B^+ \to K^{*+}(\to K^+\pi^0)\gamma$ mode and $B^+ \to K^{*+}(\to K_S^0\pi^+)\gamma$ mode.

8.3 Discussion

Results of this study are compared with the results of the past experiment: the CLEO-II experiment and the Belle experiment, and validity of apparatus and software of the Belle II experiment for rare B-decay search is discussed. We also discuss the systematic uncertainty in the analysis of $B \to K^*\gamma$.

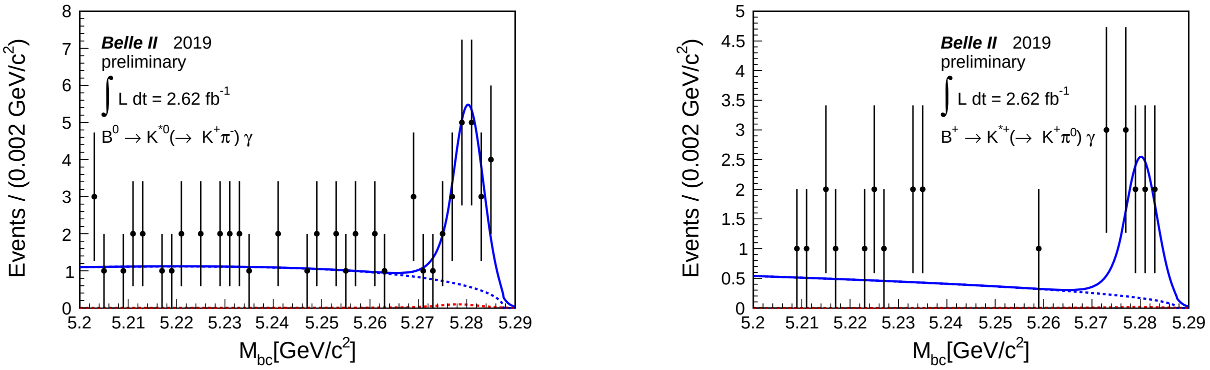

(a) $B^0 \to K^{*0}(\to K^+\pi^-)\gamma$ (b) $B^+ \to K^{*+}(\to K^+\pi^0)\gamma$

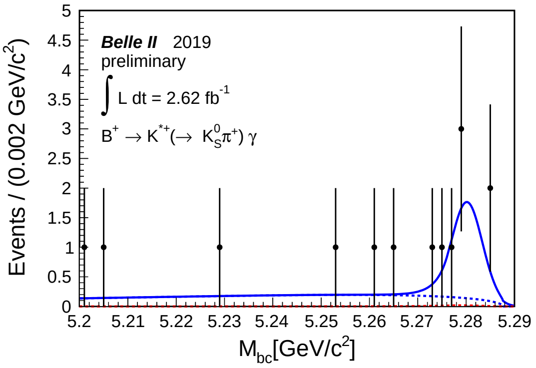

(c) $B^+ \to K^{*+}(\to K^0_S\pi^+)\gamma$

FIGURE 8.10: M_{bc} distribution with fitting curve .Blue solid line is fitting curve with all components, blue dash line is continuum background, red dash line is peaking and higher resonance background.

8.3.1 Comparing to the CLEO-II experiment

The CLEO-II experiment, operated from 1986 to 1993, first observed the $B \to K^{*}\gamma$ decay using data corresponding to an integrated luminosity of 1.38 fb^{-1}. The obtained number of signal is 10.5 ± 3.6. From our study, the number of signal is found to be 35.5 ± 6.9 using 2.62 fb^{-1}. The comparison between the CLEO-II experiment and this study is summarized in Table 8.9. This result is consistent with the expected number of signal which is calculated from world average value [89] and efficiency of MC of this study. It demonstrates that the Belle II spectrometer working as expected and MC simulation of Belle II expresses the real data correctly. The Belle II experiment provides better results using first data set than CLEO-II. It concludes that Belle II has capability to measure rare B-meson decays.

TABLE 8.8: Summary of log likelihood value when signal yield is fixed to zero and significance.

mode	log likelihood value (signal yield =0)	significance
$B^0 \to K^{*0}\gamma \to K^+\pi^-\gamma$	19.28	4.42
$B^+ \to K^{*+}\gamma \to K^+\pi^0\gamma$	13.90	3.73
$B^+ \to K^{*+}\gamma \to K^0_S\pi^+\gamma$	4.52	2.13

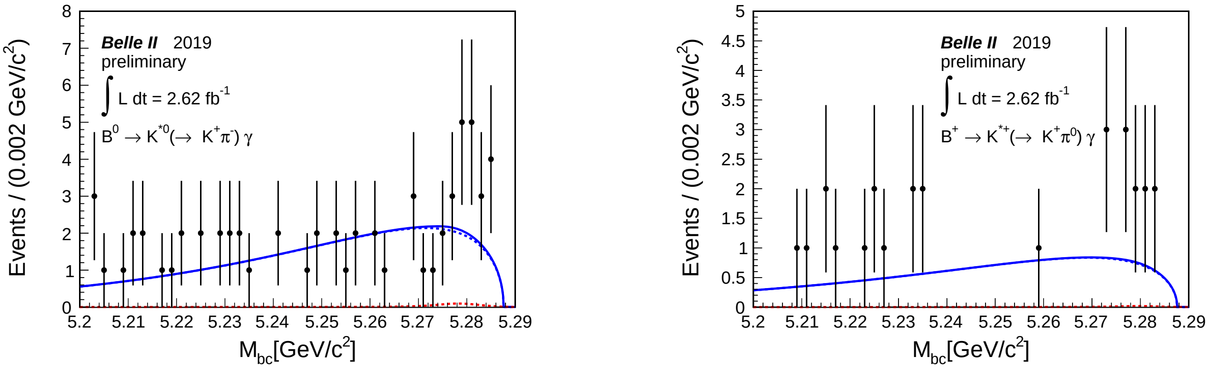

(a) $B^0 \to K^{*0}(\to K^+\pi^-)\gamma$ (b) $B^+ \to K^{*+}(\to K^+\pi^0)\gamma$

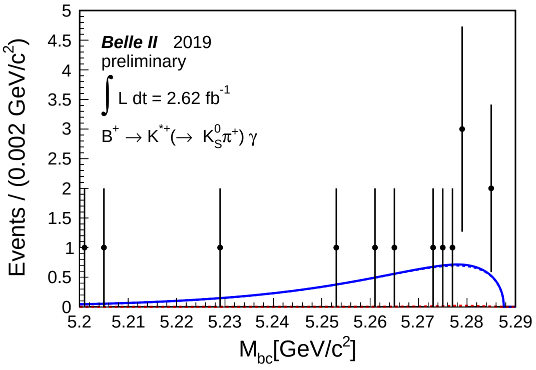

(c) $B^+ \to K^{*+}(\to K^0_S\pi^+)\gamma$

FIGURE 8.11: M_{bc} distribution with fitting curve when signal yield is fixed to 0. Blue solid line is fitting curve with all components, blue dash line is continuum background, red dash line is peaking and higher resonance background.

8.3.2 Comparing to the Belle experiment

I compare reconstruction efficiencies to the Belle experiment. The reconstruction efficiency is obtained by MC and corrected by the ratio of data to MC using control samples. The reconstruction efficiency is defined as the ratio of the number of remained events to the number of generated events of $B \to K^*\gamma$. To correct efficiency, we use correction factor R_{eff}. The correction factor R_{eff} is defined as the ratio of efficiency of real data to MC.

$$R_{\text{eff}} = \frac{\epsilon_{\text{data}}}{\epsilon_{\text{MC}}} \tag{8.6}$$

TABLE 8.9: Comparison between the CLEO-II experiment and this study. The uncertainty of the number of signal is statistics.

	CLEO-II [18]	This study
Number of signal	10.5 ± 3.6	35.5 ± 6.9
Integrated luminosity	1.38 fb^{-1}	2.62 fb^{-1}
Number of $B\bar{B}$	1.39×10^6	2.864×10^6
Operation period	1986 to 1993 (seven years)	May to June 2019 (four months)

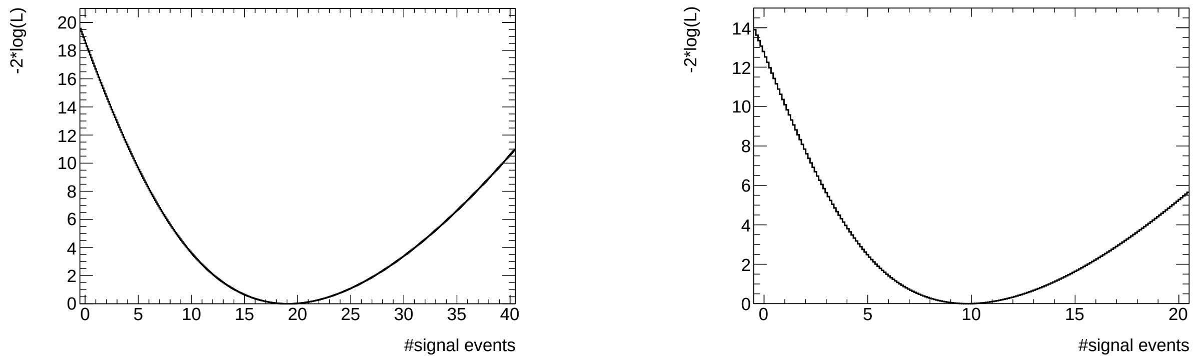

(a) $B^0 \to K^{*0}(\to K^+\pi^-)\gamma$ (b) $B^+ \to K^{*+}(\to K^+\pi^0)\gamma$

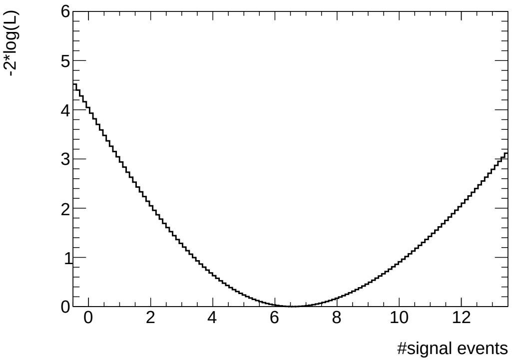

(c) $B^+ \to K^{*+}(\to K_S^0\pi^+)\gamma$

FIGURE 8.12: Log likelihood curve as a function of signal yield.

TABLE 8.10: Comparison of the efficiencies between the Belle experiment and this study.

	Belle [20]	This study
$B^0 \to K^{*0}(\to K^+\pi^-)\gamma$	$15.61 \pm 0.49\%$	$14.97 \pm 1.10\%$
$B^+ \to K^{*+}(\to K^+\pi^0)\gamma$	$3.66 \pm 0.12\%$	$4.34 \pm 0.50\%$
$B^+ \to K^{*+}(\to K_S^0\pi^+)\gamma$	$5.01 \pm 0.14\%$	$4.20 \pm 0.47\%$

where ϵ_{data} and ϵ_{MC} are efficiencies of real data and MC, respectively. The uncertainty of R_{eff} is assigned as the systematic uncertainty of the selection. Correction factors of each selection criteria are described in subsection 8.3.3.

Table 8.10 shows the results of corrected reconstruction efficiencies for each decay modes. Since the number of layers of VXD in the Belle II spectrometer is increased, the amount of materials in front of CDC is increased compared to Belle. Thus, gamma conversion and multiple scattering are more likely to happen and we are concerned that the reconstruction efficiency will be worse than that of Belle. In addition, detector is not fully understood since Belle II is very early stage and the difference between real data and MC is not small. Results of this study are comparable to Belle even at the early state of the Belle II experiment. We expect the improvement of the reconstruction efficiency by further tuning of tracking, particle identification, reconstruction of gamma, and so on.

8.3.3 The branching fraction

The branching fraction $\mathcal{B}$ and its systematic uncertainty $\sigma_{\mathcal{B}}$ are defined as

$$\mathcal{B} = \frac{N_{\mathrm{sig}}}{N_{B\bar{B}} \times \epsilon}, \tag{8.7}$$

$$\sigma_{\mathcal{B}} = \mathcal{B}\sqrt{\left(\frac{\sigma_{N_{\mathrm{syst.}}}}{N_{\mathrm{sig}}}\right)^2 + \left(\frac{\sigma_{\epsilon}}{\epsilon}\right)^2 + \left(\frac{\sigma_{N_{B\bar{B}}}}{N_{B\bar{B}}}\right)^2}, \tag{8.8}$$

where N_{sig} is number of signal events obtained by signal yield extraction, $N_{B\bar{B}}$ is number of $B\bar{B}$ pairs, ϵ is reconstruction efficiency, $\sigma_{N_{\mathrm{syst.}}}$ is systematic uncertainty of N_{sig}. Since reconstruction efficiencies ϵ are already discussed in subsection 8.3.2, definitions of N_{sig} and $N_{B\bar{B}}$ are given in this section. All sources of systematic uncertainty are summarized in Table 8.11 and detailed descriptions of each sources are given in the following subsections.

The branching fractions for each decay modes are

$$\mathcal{B}(B^0 \to K^{*0}(\to K^+\pi^-)\gamma) = (4.58 \pm 1.25 \pm 0.38) \times 10^{-5},$$
$$\mathcal{B}(B^+ \to K^{*+}(\to K^+\pi^0)\gamma) = (2.56 \pm 0.89 \pm 0.35) \times 10^{-5},$$
$$\mathcal{B}(B^+ \to K^{*+}(\to K_S^0\pi^+)\gamma) = (1.78 \pm 0.84 \pm 0.27) \times 10^{-5},$$

where the second value is statistic uncertainties, the third value is systematic uncertainty. Using the Belle II data, I measure the branching fractions of $B \to K^*\gamma$ decay. The statistical uncertainty are found to be dominant for all modes. On the other hand, systematic uncertainty is also affected by amount of statistics since correction factor contains statistical uncertainty for the efficiency of data. Both uncertainty can be improved with the future accumulation of data. I verify that the Belle can measure the branching fractions, and this lead to the ability to measure various parameters for searching NP such as CP asymmetry, isospin asymmetry in future operation.

TABLE 8.11: The list of systematic uncertainties for branching fraction.

Value	Source	$K^+\pi^-\gamma$	$K^+\pi^0\gamma$	$K_S^0\pi^+\gamma$
$N_{B\bar{B}}$	Number of BB pairs	1.6 %	1.6 %	1.6 %
	f_{+-}/f_{00}	1.2 %	1.2%	1.2%
ϵ	Photon selection	3.72 %	3.72 %	3.72 %
	Tracking	1.29 %	0.91 %	0.91 %
	Charged K/π identification	0.5 %	0.4 %	0.3%
	K_S^0 reconstruction	-	-	7.2 %
	π^0 reconstruction	-	4.63 %	-
	FastBDT	6.09 %	7.66 %	7.66 %
	π^0/η veto	0.2 %	0.2 %	0.2 %
N_{sig}	Fitter bias	2.1 %	6.2 %	8.1 %
	Fixed parameter in fit	1.94 %	4.48 %	5.76 %
	Peaking and higher resonance	2.09 %	1.48%	1.28%
Total		8.2 %	14.0 %	15.1 %

Number of $B\bar{B}$ pairs

The number of $B\bar{B}$ pairs is estimated by subtracting the amount of off-resonance from on-resonance [93]. The calculation to estimate the number of $B\bar{B}$ pairs is defined as

$$N_{B\bar{B}} = \frac{(N_{\text{had}}^{\text{on-res}} - R_{\text{lumi}} \times N_{\text{had}}^{\text{off-res}} \times k)}{\epsilon_{B\bar{B}}}, \tag{8.9}$$

where $N_{\text{had}}^{\text{on-res}}$ is the number of selected hadronic events in on-resonance data, $R_{\text{lumi}} \times N_{\text{had}}^{\text{off-res}} \times k$ is the estimated number of non-$B\bar{B}$ events in on-resonance data, and $\epsilon B\bar{B}$ is the efficiency of the hadronic selection for $B\bar{B}$ events. R_{lumi} is the ratio of luminosity of on-resonance to off-resonance, $N_{\text{had}}^{\text{off-res}}$ is the number of selected hadronic events in off-resonance data, and k take into account the variation in non-$B\bar{B}$ efficiency and cross sections with beam energy. As a results, the number of $B\bar{B}$ events corresponds to an integrated luminosity of 2.62 fb^{-1} is 2.864×10^6 and 1.6 % of systematic uncertainty is assigned.

f_{+-}/f_{00}

The branching fractions of $\Upsilon(4S)$ to B^+B^- and $B^0\bar{B}^0$ are $\mathcal{B}(\Upsilon(4S) \to B^+B^-) = 0.514 \pm 0.006$ and $\mathcal{B}(\Upsilon(4S) \to B^0\bar{B}^0) = 0.486 \pm 0.006$, respectively [89]. Therefore, 1.2 % of systematic uncertainties is assigned.

Photon selection efficiency

The efficiency of high energy photon is measured using radiative muon events, $e^+e^- \to \mu^+\mu^-\gamma_{\text{ISR}}$, where γ_{ISR} is an initial-state radiation photon [94]. The kinematics of photon can be defined by kinematics of two muons in the event and beam parameters as a missing recoil vector. The missing recoil vector is used as the photon direction and we check if the photon is reconstructed in that direction. The photon finding efficiency is defined as the efficiency to find the photon in the direction of the missing recoil vector. As a result, correction factor is 0.981 ± 0.0372.

Tracking efficiency

The tracking efficiency for charged track is measured using $e^+e^- \to \tau^+\tau^-$ events [95]. The target process is $\tau \to \ell^{\pm}\nu_\ell\bar{\nu}_\tau$ while the other is $\tau \to 3\pi^{\pm}\nu_\tau + n\pi^0$. The event has three good tracks with total charge is ± 1 is used to tag tau pair event. The additional track is expected to conserve the charge. The efficiency is defined as

$$\epsilon \cdot A = \frac{N_4}{N_3 + N_4}, \tag{8.10}$$

where N_4 is the number of events with all four tracks, N_3 is the number of events that additional track is missed, and A is factor to take into account the acceptance of the Belle II detector. As a result, the correction factor is 0.9987 ± 0.0091.

Charged K/π identification

Charged particle identification is evaluated by using $D^* \to D^0(\to K\pi)\pi$ [96]. Kinematics of charged K/π in $B \to K^*\gamma$ and $D^{*+} \to D^0\pi^+$ are very similar since decay process. Basically, same procedure written in section 6.3 although all sub-detectors are included. As a result, the correction factors for K and π are 98.8 ± 0.4 and 94.8 ± 0.3.

K_S^0 reconstruction

Comparing the reconstructed yields of $D^0 \to K^-\pi^+\pi^-\pi^+$ and $D^0 \to K_S^0\pi^+\pi^-$, the K_S^0 efficiency is evaluated [97]. Both have the same number of tracks and any discrepancy of tracking efficiency is cancel out. The correction factor is evaluated with the double ratio:

$$\frac{\left(\frac{N(D^0\to K_S^0\pi^+\pi^-)}{N(D^0\to K^-\pi^+\pi^-\pi^+)}\right)_{\text{data}}}{\left(\frac{N(D^0\to K_S^0\pi^+\pi^-)}{N(D^0\to K^-\pi^+\pi^-\pi^+)}\right)_{\text{MC}}}, \tag{8.11}$$

where N is the reconstructed yields of the decay which written in parenthesis. As a result, the correction factor of K_S^0 reconstruction is 1.043 ± 0.072.

π^0 reconstruction

The ratio of reconstruction efficiency between data and MC is measured by $\eta \to \gamma\gamma$ and $\eta \to 3\pi^0$ [98]. By assuming $\epsilon_{\text{data}}(\pi^0 \to \gamma\gamma)/\epsilon_{\text{MC}}(\pi^0 \to \gamma\gamma) = \epsilon_{\text{data}}(\eta \to \gamma\gamma)/\epsilon_{\text{MC}}(\eta \to \gamma\gamma)$, the π^0 efficiency is defined as

$$\frac{\epsilon_{\text{data}}(\pi^0)}{\epsilon_{\text{MC}}(\pi^0)} = \sqrt{\frac{\epsilon_{\text{data}}(2\pi^0)}{\epsilon_{\text{MC}}(2\pi^0)}}, \tag{8.12}$$

$$\frac{\epsilon_{\text{data}}(2\pi^0)}{\epsilon_{\text{MC}}(2\pi^0)} = \frac{N_{\text{data}}(\eta \to 3\pi^0)/N_{\text{MC}}(\eta \to 3\pi^0)}{N_{\text{data}}(\eta \to \gamma\gamma)/N_{\text{MC}}(\eta \to \gamma\gamma)}. \tag{8.13}$$

As a result, the correction factor of π^0 reconstruction is 0.945 ± 0.0711.

FastBDT selection

Using the control samples of $B \to D\pi$ mode, I evaluate systematic uncertainty of FastBDT selection. We obtain the number of events before and after applying FastBDT selection by fitting with same method written in section 8.1.1. FastBDT value is defined in the same way as section 7.2. The obtained number of events are summarized in Table 8.12 As a result, R_{eff} is 0.9993 ± 0.0606 for neutral $B$and 0.9865 ± 0.0766 for charged B.

π^0/η veto

The performance of the π^0 and η veto is evaluated using directly reconstructed π^0 and η candidates [83]. The π^0 and η candidates are reconstructed using high energy photon and low energy photon to match the kinematics of $b \to s\gamma$. As a result, the correction factors of π^0 veto and η

TABLE 8.12: Number of events

Mode	BDT selection	MC	Real data
$B^0 \to D^-(\to K^+\pi^-\pi^-)\pi^+$	NOT applied	4284.55 ±77.28	848.08 ±32.83
	applied	3717.04 ±65.15	736.27 ±28.99
$B^+ \to \bar{D}^0(\to K^-\pi^+)\pi^+$	NOT applied	2151.49 ±51.82	576.35 ±28.00
	applied	1601.41 ±40.88	434.86 ±21.47

veto are 1.027 ± 0.002 and 0.9838 ± 0.0004, respectively. Combining both vetos, the correction factor of the π^0/η veto is 1.010 ± 0.002.

Peaking and higher resonance backgrounds

Varying the yeild of peaking and higher resonance backgrounds by ±100%, we evaluate the deviation from original signal yield. The systematic uncertainty is defined as

$$\text{Systematic uncertainty} = \frac{N_{\text{orig}} - N_{\pm}}{N_{\text{orig}}}, \tag{8.14}$$

where N_{orig} is original signal yield, $N_{\pm}$ is signal yield when the background yield is varied by ±100%. To be conservative, larger deviation is quoted as this systematic uncertainty. As a result, 2.09 %, 1.48 %, and 1.28 % are assigned for $B^0 \to K^{*0}(\to K^+\pi^-)\gamma$ mode, $B^+ \to K^{*+}(\to K^+\pi^0)\gamma$ mode, and $B^+ \to K^{*+}(\to K^0_S\pi^+)\gamma$ mode, respectively.

Fitter bias

I evaluate the fitter bias using toy MC. 1,000 sets of toy MCs are generated and fitted by same function written in subsection 8.1.2. The generated number of events are based on poisson distribution with a mean value of expectation. Pull is defined as

$$\text{pull} = \frac{N_{\text{gen}} - N_{\text{fit}}}{\sigma_{N_{\text{fit}}}}, \tag{8.15}$$

where N_{gen} is the generated number of events, N_{fit} is the measured number of events by fitting, and $\sigma_{N_{\text{fit}}}$ is uncertainty of N_{fit}. The pull distributions for each decay mode are shown in Figure 8.13. The pull distribution is fitted by Gaussian and the mean value is used to estimate systematic error of fitter bias.

$$\text{Fitter bias} = \frac{\mu - \sigma_{N_{\text{sig}}}}{N_{\text{sig}}}, \tag{8.16}$$

where μ is mean of pull distribution, N_{sig} and $\sigma_{N_{\text{sig}}}$ are signal yields and its statistical uncertainty written in section 8.2. As a result, 2.1% ,6.2%, and 8.1% of systematic uncertainties are assigned for $B^0 \to K^{*0}(\to K^+\pi^-)\gamma$, $B^+ \to K^{*+}(\to K^+\pi^0)\gamma$, and $B^+ \to K^{*+}(\to K^0_S\pi^+)\gamma$, respectively.

Fixed parameter in fit

Five fixed parameters for PDFs of signal and continuum background components listed in Table 8.1 have finite errors and those can cause systematic uncertainty of the signal yield. Those

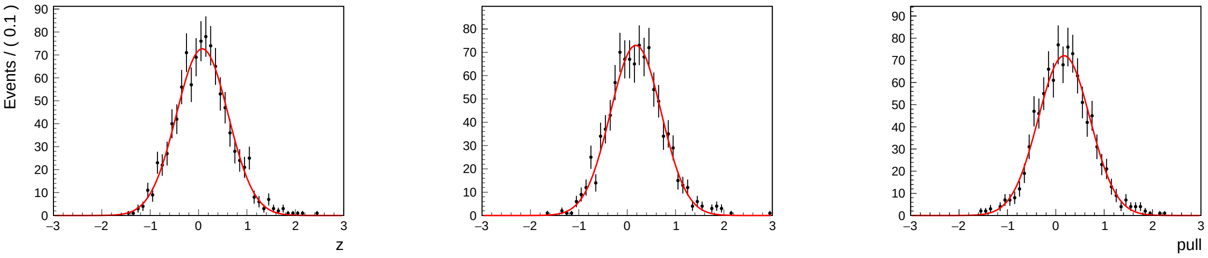

(a) $B^0 \to K^{*0}(\to K^+\pi^-)\gamma$ (b) $B^+ \to K^{*+}(\to K^+\pi^0)\gamma$ (c) $B^+ \to K^{*+}(\to K^0_S\pi^+)\gamma$

FIGURE 8.13: Pull distributions for each decay mode.

TABLE 8.13: Systematic uncertainty from fixed parameter.

Function	Parameter	$K^+\pi^-\gamma$	$K^+\pi^0\gamma$	$K^0_S\pi^+\gamma$
Crystal ball	mean	0.97 %	1.23 %	1.36%
	sigma	1.08 %	0.63 %	1.58 %
	α	1.01 %	4.23 %	5.19 %
	n	0.53 %	0.002 %	1.06 %
Argus	end point	0.58 %	0.54 %	0.88 %
Total		1.94 %	4.48 %	5.76 %

systematic uncertainty are evaluated. Mean and sigma of crystal ball for signal and end point of argus for continuum backgrounds are varied by $\pm 1\sigma$ error. Larger deviation is quoted as this systematic uncertainty. Tail parameters of crystal ball α and n are floated individually, and deviation of signal yield is evaluated. Systematics uncertainties from fixed parameters are summarized in Table 8.13.

Chapter 9

Conclusion

The Aerogel RICH counter is a novel type of particle identification device located at the end-cap region of the Belle II spectrometer. The construction of the Aerogel RICH counter and its installation into the Belle II spectrometer was completed.

I evaluate the performance of HAPDs to verify if the ARICH counter works as expected under the practical environment of the Belle II experiment. The signal-to-noise ratio is found to be greater than seven at around the upper limit of the operating temperature and I confirm that HAPDs can distinguish signal from noise in the entire range of operating temperature. Furthermore, long term stability of signal-to-noise ratio and the fraction of dead channels are monitored during the commissioning period of the Belle II experiment and are found to be greater than six and less than 1 %, respectively. Those results prove that the performance of HAPDs fulfill our requirement under the nominal or even worse environment of the Belle II experiment.

The performance of particle identification is evaluated using the first data set of beam collisions at Belle II. The overall $K(\pi)$ efficiency and $\pi(K)$ misidentification probability are measured using $D^{*+} \to D^0(\to K^-\pi^+)\pi^+$ samples to be $93.5 \pm 0.6\%$ (87.5 ± 0.9 %) and 10.9 ± 0.9 % (5.6 ± 0.3 %), respectively. The momentum and the polar angle dependence of the particle identification is evaluated, and efficiency and misidentification probability are approximately greater than 90% and smaller than 10% throughout the whole range of the polar angle in the ARICH acceptance and throughout the whole momentum range of the B-meson decay except for low momentum range that can be covered by CDC. It proves that the ARICH has the capability to identify kaon and pions as required for the Belle II experiment.

We search $B \to K^*\gamma$ decays at early stage of the Belle II experiment. Using data that corresponds to an integrated luminosity of $2.62\,\mathrm{fb}^{-1}$, we measured the numbers of signals to be 19.1 ± 5.2, 9.8 ± 3.4 and 6.6 ± 3.1 for $B^0 \to K^{*0}(\to K^+\pi^-)\gamma$, $B^+ \to K^{*+}(\to K^+\pi^0)\gamma$ and $B^+ \to K^{*+}(\to K^0_S\pi^+)\gamma$, respectively. By combining all these modes, we rediscover the $B \to K^*\gamma$ decays with the significance of $6.2\,\sigma$. This results is obtained by using a part of the first data set of the Belle II experiment, by this result reproduce the first observation of $B \to K^*\gamma$, which is one of the major physics result at the CLEO-II experiment. In addition, the reconstruction efficiencies of those decays are comparable to Belle even there are concerns of worse reconstruction efficiency less understanding of the detector. This study demonstrates that Belle II has the capability to reconstruct rare B-decays as expected and Belle II is ready to search new physics beyond the Standard Model.

Appendix A

Calculations

A.1 Correction of the width of signal PDF

From definition of M_{bc}, the width is defined as

$$\begin{aligned}\sigma^2_{M_{\mathrm{bc}}} &= (\frac{E^*_{beam}}{M_{\mathrm{bc}}})^2 \sigma^2_{E^*_{beam}} + (\frac{p^*_B}{M_{\mathrm{bc}}})^2 \sigma^2_{p^*_B} \\ &\sim \sigma^2_{E^*_{beam}} + (\frac{p^*_B}{M_{\mathrm{bc}}})^2 \sigma^2_{p^*_B} (\because \frac{E^*_{beam}}{M_{\mathrm{bc}}} \sim 1) \end{aligned} \tag{A.1}$$

where E^*_{beam} is beam energy in CMS, $\sigma_{E^*_{beam}}$ is variation of beam energy in CMS comes from beam energy spread, p^*_B is momentum of B meson in CMS, $\sigma^*_{p_B}$ is variation of momentum of B meson comes from energy resolution of high energy photon. Beam energy spread is same between $B \to K^*\gamma$ mode and $B \to D\pi$ mode. Since $\sigma^*_{p_B}$ is come from resolution of high energy photon, $\sigma^*_{p_B}$ can be re-written as

$$\sigma^*_{p_B} \sim \sigma_{E^*_\gamma} = \frac{E^*_\gamma}{E_\gamma}\sigma_{E_\gamma} \sim \sigma_{E_\gamma} \quad (\because \frac{E^*_\gamma}{E_\gamma} \sim 1) \tag{A.2}$$

where $\sigma_{E^*_\gamma}$ is variation of photon energy of in CMS, E^*_γ is photon energy in CMS, E_γ is photon energy in Lab frame and σ_{E_γ} is variation of photon energy in Lab frame. Thus, $(\frac{p^*_B}{M_{\mathrm{bc}}})^2 \sigma^2_{p^*_B}$ for $B \to D\pi$ mode is approximately equal to 0.

In addition, we obtain following four equations.

$$
\begin{aligned}
\sigma^2_{M_{\rm bc}}(K^*\gamma;MC) &= \sigma^2_{E^*_{beam}}(K^*\gamma;MC) + (\frac{p^*_B}{M_{\rm bc}})^2 \sigma^2_{p^*_B}(K^*\gamma;MC) \\
&\sim \sigma^2_{E^*_{beam}}(K^*\gamma;MC) + (\frac{p^*_B}{M_{\rm bc}})^2 \sigma^2_{E_\gamma}(MC) \quad (\because \sigma^*_{p_B} \sim \sigma_{E_\gamma}) \qquad \text{(A.3)} \\
\sigma^2_{M_{\rm bc}}(K^*\gamma;data) &= \sigma^2_{E^*_{beam}}(K^*\gamma;data) + (\frac{p^*_B}{M_{\rm bc}})^2 \sigma^2_{p^*_B}(K^*\gamma;data) \\
&\sim \sigma^2_{E^*_{beam}}(K^*\gamma;data) + (\frac{p^*_B}{M_{\rm bc}})^2 \sigma^2_{E_\gamma}(data) \quad (\because \sigma^*_{p_B} \sim \sigma_{E_\gamma}) \qquad \text{(A.4)} \\
\sigma^2_{M_{\rm bc}}(D\pi;MC) &= \sigma^2_{E^*_{beam}}(D\pi;MC) + (\frac{p^*_B}{M_{\rm bc}})^2 \sigma^2_{p^*_B}(D\pi;MC) \\
&\sim \sigma^2_{E^*_{beam}}(D\pi;MC) \quad (\because (\frac{p^*_B}{M_{\rm bc}})^2 \sigma^2_{p^*_B}(D\pi;MC) \sim 0) \\
&= \sigma^2_{E^*_{beam}}(K^*\gamma;MC) \quad (\because \sigma^2_{E^*_{beam}}(D\pi;MC) = \sigma^2_{E^*_{beam}}(K^*\gamma;MC)) \qquad \text{(A.5)} \\
\sigma^2_{M_{\rm bc}}(D\pi;data) &= \sigma^2_{E^*_{beam}}(D\pi;data) + (\frac{p^*_B}{M_{\rm bc}})^2 \sigma^2_{p^*_B}(D\pi;data) \qquad \text{(A.6)} \\
&\sim \sigma^2_{E^*_{beam}}(D\pi;data) \quad (\because (\frac{p^*_B}{M_{\rm bc}})^2 \sigma^2_{p^*_B}(D\pi;data) \sim 0) \\
&= \sigma^2_{E^*_{beam}}(K^*\gamma;data) \quad (\because \sigma^2_{E^*_{beam}}(D\pi;data) = \sigma^2_{E^*_{beam}}(K^*\gamma;data)) \qquad \text{(A.7)}
\end{aligned}
$$

where $\sigma^2_{M_{\rm bc}}(K^*\gamma;MC)$ and $\sigma^2_{M_{\rm bc}}(K^*\gamma;data)$ are width of $M_{\rm bc}$ distribution of $B \to K^*\gamma$ mode for MC and data, $\sigma^2_{M_{\rm bc}}(D\pi;MC)$ and $\sigma^2_{M_{\rm bc}}(D\pi;data)$ are width of $M_{\rm bc}$ distribution of $B \to K^*\gamma$ mode for MC and data. Substituting eq. Equation A.7 for Equation A.4 and deforming Equation A.3, we obtain following formula.

$$
\begin{aligned}
\sigma^2_{M_{\rm bc}}(K^*\gamma;data) &= \sigma^2_{E^*_{beam}}(K^*\gamma;data) + (\frac{p^*_B}{M_{\rm bc}})^2 \sigma^2_{E_\gamma}(data) \quad (\because \sigma^*_{p_B} \sim \sigma_{E_\gamma}) \\
&= \sigma^2_{M_{\rm bc}}(D\pi;data) + (\frac{p^*_B}{M_{\rm bc}})^2 \sigma^2_{E_\gamma}(MC) \cdot \frac{\sigma^2_{E_\gamma}(data)}{\sigma^2_{E_\gamma}(MC)} \qquad \text{(A.8)} \\
(\frac{p^*_B}{M_{\rm bc}})^2 \sigma^2_{E_\gamma}(MC) &= \sigma^2_{M_{\rm bc}}(K^*\gamma;MC) - \sigma^2_{E^*_{beam}}(D\pi;MC) \qquad \text{(A.9)}
\end{aligned}
$$

Substituting Equation A.9 for Equation A.8, we obtain the final formula of width correction.

$$
\begin{aligned}
\sigma^2_{M_{\rm bc}}(K^*\gamma;data) &= \sigma^2_{M_{\rm bc}}(D\pi;data) \\
&\quad + \{\sigma^2_{M_{\rm bc}}(K^*\gamma;MC) - \sigma^2_{E^*_{beam}}(D\pi;MC)\} \cdot (\frac{\sigma_{E_\gamma}(data)}{\sigma_{E_\gamma}(MC)})^2 \qquad \text{(A.10)}
\end{aligned}
$$

We use this formula to fix width of crystal ball to signal to fit real data.

Appendix B

Figures

B.1 Comparison of Cherenkov angle distribution for $K_S^0 \to \pi^+\pi^-$ decay

Comparisons of Cherenkov angle distribution between data and PDF estimation using $K_S^0 \to \pi^+\pi^-$ samples in the momentum range of 0.0 GeV/c to 4.0 GeV/c are shown in Figure B.1 -B.4.

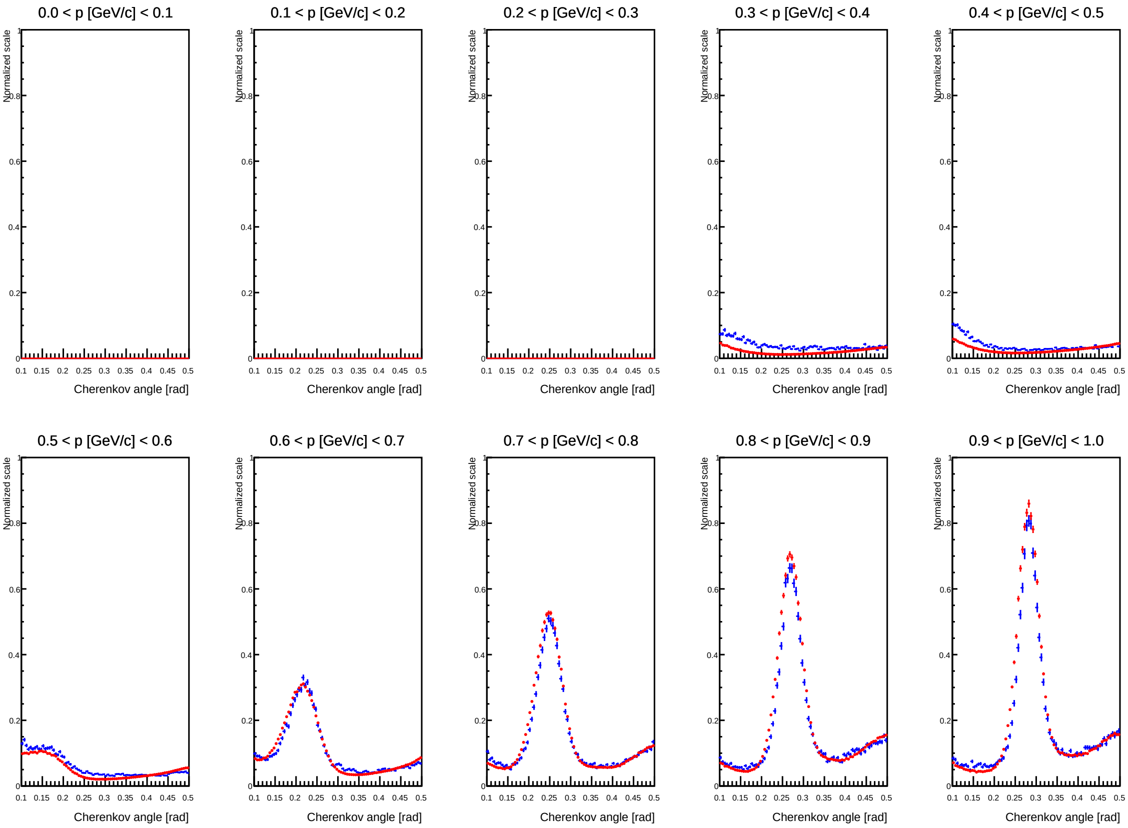

FIGURE B.1: Comparisons in the momentum range of 0.0 GeV/c to 1.0 GeV/c. Blue marker is data and Red marker is PDF estimation. Both are normalized by the number of tracks.

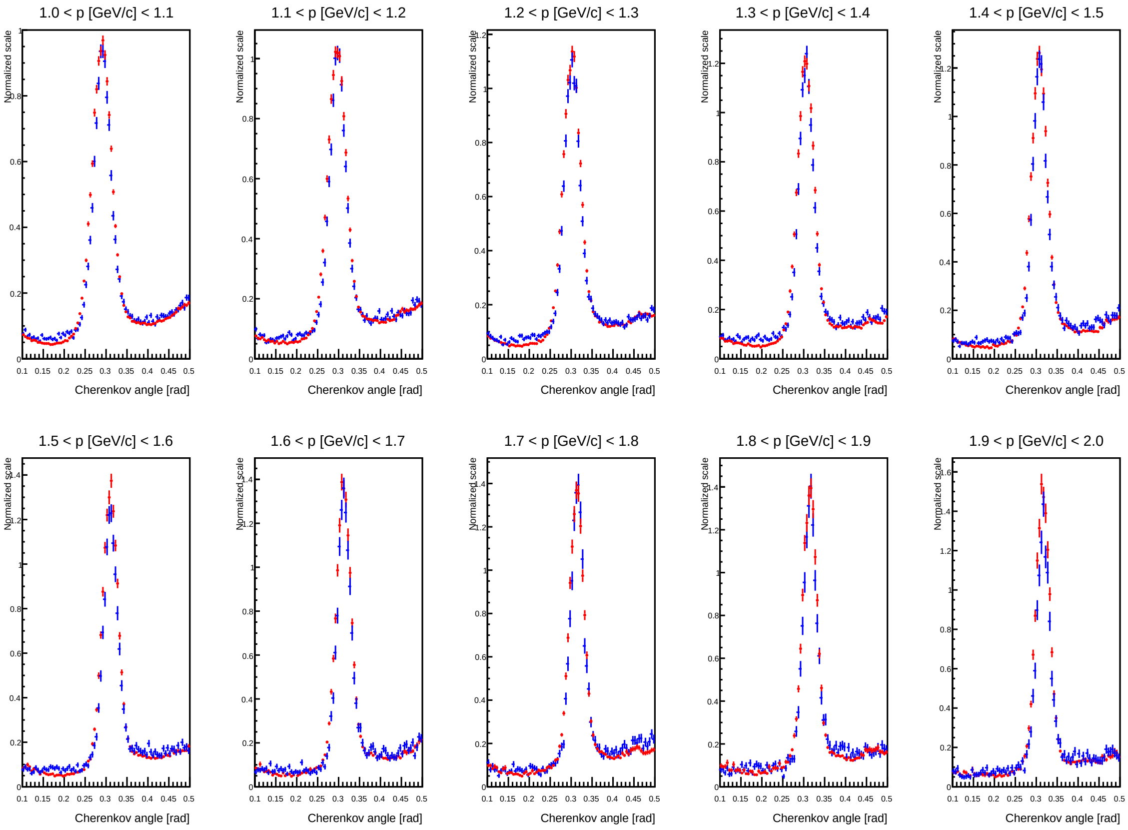

FIGURE B.2: Meaning of plots are with similar to Figure B.1, but in the momentum range of 1.0 GeV/c to 2.0 GeV/c.

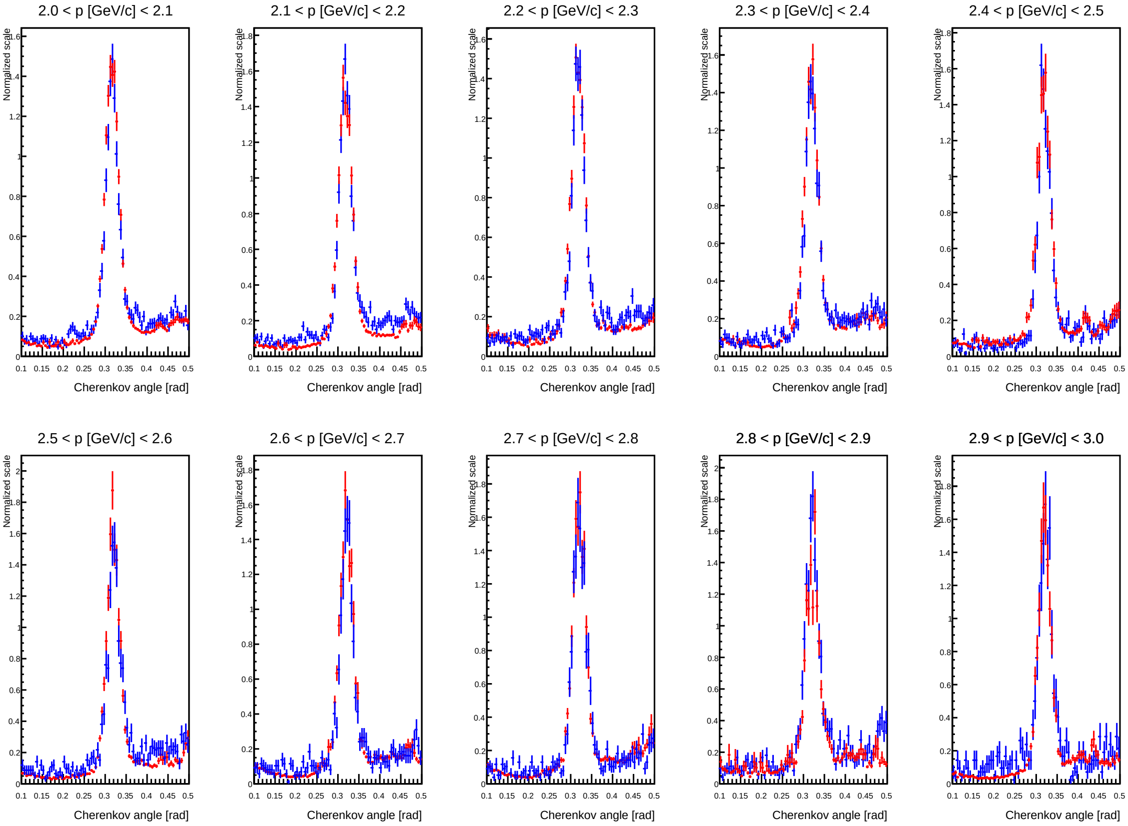

FIGURE B.3: Meaning of plots are with similar to Figure B.1, but in the momentum range of 2.0 GeV/c to 3.0 GeV/c.

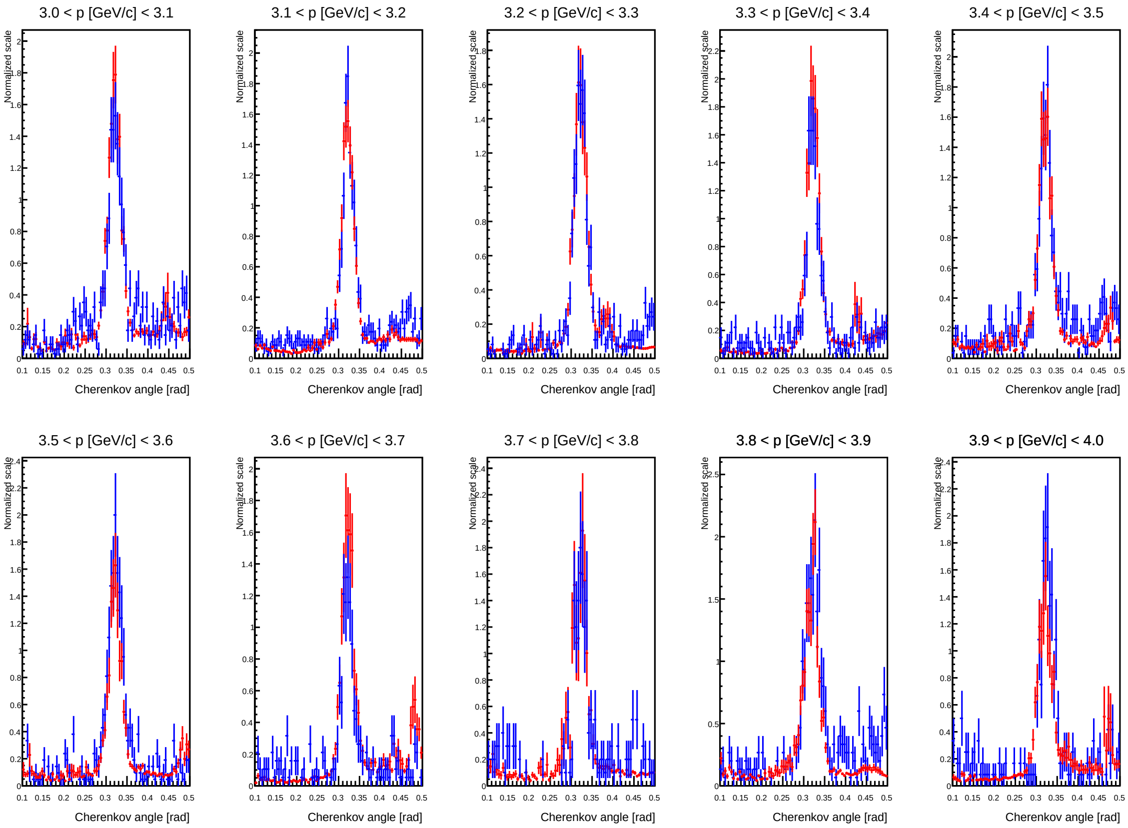

FIGURE B.4: Meaning of plots are with similar to Figure B.1, but in the momentum range of 3.0 GeV/c to 4.0 GeV/c.

Bibliography

[1] A. D. Sakharov. "Violation of CP Invariance, C Asymmetry, and Baryon Asymmetry of the Universe". In: *Soviet Journal of Experimental and Theoretical Physics Letters* 5 (Jan. 1967), p. 24. ISSN: ['0021-3640'].

[2] J. H. Christenson et al. "Evidence for the 2π Decay of the K_2^0 Meson". In: *Physical Review Letters* 13.4 (July 1964), pp. 138–140. DOI: `10.1103/PhysRevLett.13.138`.

[3] Makoto Kobayashi and Toshihide Maskawa. "CP-Violation in the Renormalizable Theory of Weak Interaction". In: *Progress of Theoretical Physics* 49.2 (Feb. 1973), pp. 652–657. ISSN: 0033-068X. DOI: `10.1143/PTP.49.652`.

[4] The ATLAS Collaboration et al. "The ATLAS Experiment at the CERN Large Hadron Collider". In: *Journal of Instrumentation* 3.08 (Aug. 2008), S08003–S08003. ISSN: 1748-0221. DOI: `10.1088/1748-0221/3/08/S08003`.

[5] The CMS Collaboration et al. "The CMS Experiment at the CERN LHC". In: *Journal of Instrumentation* 3.08 (Aug. 2008), S08004. ISSN: 1748-0221. DOI: `10.1088/1748-0221/3/08/S08004`.

[6] G. Aad et al. "Observation of a New Particle in the Search for the Standard Model Higgs Boson with the ATLAS Detector at the LHC". In: *Physics Letters B* 716.1 (Sept. 2012), pp. 1–29. ISSN: 0370-2693. DOI: `10.1016/j.physletb.2012.08.020`.

[7] S. Chatrchyan et al. "Observation of a New Boson at a Mass of 125 GeV with the CMS Experiment at the LHC". In: *Physics Letters B* 716.1 (Sept. 2012), pp. 30–61. ISSN: 0370-2693. DOI: `10.1016/j.physletb.2012.08.021`.

[8] Lyndon Evans and Philip Bryant. "LHC Machine". In: *Journal of Instrumentation* 3.08 (Aug. 2008), S08001–S08001. ISSN: 1748-0221. DOI: `10.1088/1748-0221/3/08/S08001`.

[9] Nicola Cabibbo. "Unitary Symmetry and Leptonic Decays". In: *Physical Review Letters* 10.12 (June 1963), pp. 531–533. DOI: `10.1103/PhysRevLett.10.531`.

[10] Lincoln Wolfenstein. "Parametrization of the Kobayashi-Maskawa Matrix". In: *Physical Review Letters* 51.21 (Nov. 1983), pp. 1945–1947. DOI: `10.1103/PhysRevLett.51.1945`.

[11] J. Charles et al. "CP Violation and the CKM Matrix: Assessing the Impact of the Asymmetric B Factories". In: *The European Physical Journal C - Particles and Fields* 41.1 (May 2005). Updated results and plots available at: http://ckmfitter.in2p3.fr, pp. 1–131. ISSN: 1434-6052. DOI: `10.1140/epjc/s2005-02169-1`.

[12] Super-Kamiokande Collaboration et al. "Evidence for Oscillation of Atmospheric Neutrinos". In: *Physical Review Letters* 81.8 (Aug. 1998), pp. 1562–1567. DOI: `10.1103/PhysRevLett.81.1562`.

[13] Vera C. Rubin and W. Kent Ford Jr. "Rotation of the Andromeda Nebula from a Spectroscopic Survey of Emission Regions". In: *The Astrophysical Journal* 159 (Feb. 1970), p. 379. ISSN: 0004-637X. DOI: `10.1086/150317`.

[14] B. Aubert et al. "The BABAR Detector". In: *Nuclear Instruments and Methods in Physics Research Section A: Accelerators, Spectrometers, Detectors and Associated Equipment*. Detectors for Asymmetric B-Factories 479.1 (Feb. 2002), pp. 1–116. ISSN: 0168-9002. DOI: `10.1016/S0168-9002(01)02012-5`.

[15] Belle Collaboration et al. "Observation of Mixing-Induced CP Violation in the Neutral B Meson System". In: *Physical Review D* 66.3 (Aug. 2002), p. 032007. DOI: `10.1103/PhysRevD.66.032007`.

[16] BABAR Collaboration et al. "Observation of *CP* Violation in the B^0 Meson System". In: *Physical Review Letters* 87.9 (Aug. 2001), p. 091801. DOI: `10.1103/PhysRevLett.87.091801`.

[17] D. Andrews et al. "The CLEO Detector". In: *Nuclear Instruments and Methods in Physics Research* 211.1 (June 1983), pp. 47–71. ISSN: 0167-5087. DOI: `10.1016/0167-5087(83)90556-2`.

[18] R. Ammar et al. "Evidence for Penguin-Diagram Decays: First Observation of $B \to K^*\gamma$". In: *Physical Review Letters* 71.5 (Aug. 1993), pp. 674–678. DOI: `10.1103/PhysRevLett.71.674`.

[19] A. Abashian et al. "The Belle Detector". In: *Nuclear Instruments and Methods in Physics Research Section A: Accelerators, Spectrometers, Detectors and Associated Equipment*. Detectors for Asymmetric B-Factories 479.1 (Feb. 2002), pp. 117–232. ISSN: 0168-9002. DOI: `10.1016/S0168-9002(01)02013-7`.

[20] Belle Collaboration et al. "Evidence for Isospin Violation and Measurement of *CP* Asymmetries in $B \to K^*(892)\gamma$". In: *Physical Review Letters* 119.19 (Nov. 2017), p. 191802. DOI: `10.1103/PhysRevLett.119.191802`.

[21] Belle Collaboration et al. "Observation of $b \to d\gamma$ and Determination of $|V_{td}/V_{ts}|$". In: *Physical Review Letters* 96.22 (June 2006), p. 221601. DOI: `10.1103/PhysRevLett.96.221601`.

[22] BABAR Collaboration et al. "Branching Fraction Measurements of $B^+ \to \rho^+\gamma$, $B^0 \to \rho^0\gamma$, and $B^0 \to \omega\gamma$". In: *Physical Review Letters* 98.15 (Apr. 2007), p. 151802. DOI: `10.1103/PhysRevLett.98.151802`.

[23] Belle Collaboration et al. "Measurement of Branching Fractions, Isospin, and *CP*-Violating Asymmetries for Exclusive $b \to d\gamma$ Modes". In: *Physical Review Letters* 101.11 (Sept. 2008), p. 111801. DOI: `10.1103/PhysRevLett.101.111801`.

[24] M. R. Ahmady and F. Mahmoudi. "Constraints on the Minimal Supergravity Parameter Space from NLO Calculation of Isospin Asymmetry in $B \to K^*\gamma$". In: *Physical Review D* 75.1 (Jan. 2007), p. 015007. DOI: `10.1103/PhysRevD.75.015007`.

[25] F. Mahmoudi. "SuperIso: A Program for Calculating the Isospin Asymmetry of $B \to K^*\gamma$ in the MSSM". In: *Computer Physics Communications* 178.10 (May 2008), pp. 745–754. ISSN: 0010-4655. DOI: `10.1016/j.cpc.2007.12.006`.

[26] T. Horiguchi. "Measurement of Branching Fractions as well as Isospin Asymmetries in Decays at the Belle experiment". PhD thesis. Tohoku University, Sendai, Japan, 2017. URL: `http://epx.phys.tohoku.ac.jp/eeweb/jp/paper/2017_Dthesis_horiguchi.pdf`.

[27] Alexander L. Kagan and Matthias Neubert. "Isospin Breaking in $B \to K^*\gamma$ Decays". In: *Physics Letters B* 539.3-4 (July 2002), pp. 227–234. ISSN: 03702693. DOI: `10.1016/S0370-2693(02)02100-7`. arXiv: `hep-ph/0110078`.

[28] M. Ciuchini et al. "Next-to-Leading QCD Corrections to $B \to X_s\gamma$ in Supersymmetry". In: *Nuclear Physics B* 534.1 (Nov. 1998), pp. 3–20. ISSN: 0550-3213. DOI: `10.1016/S0550-3213(98)00516-1`.

[29] A. Ali and E. Lunghi. "Extended Minimal Flavour Violating MSSM and Implications for B Physics". In: *The European Physical Journal C - Particles and Fields* 21.4 (July 2001), pp. 683–700. ISSN: 1434-6052. DOI: `10.1007/s100520100767`.

[30] A. Ali and E. Lunghi. "Implications of $B \to \rho\gamma$measurements in the Standard Model and Supersymmetric Theories". In: *The European Physical Journal C - Particles and Fields* 26.2 (Dec. 2002), pp. 195–200. ISSN: 1434-6052. DOI: `10.1140/epjc/s2002-01053-x`.

[31] N. Taniguchi. "Measurement of branching fractions, isospin and cp-violating asymmetries for exclusive $b \to d\gamma$ modes". PhD thesis. Kyoto University, Kyoto, Japan, 2008. URL: `https://www-he.scphys.kyoto-u.ac.jp/member/nanae/thesis/thesis_nanae.pdf`.

[32] *KEKB B-Factory Design Report*. KEK Report 95-7. Aug. 1995.

[33] S. Kurokawa and E. Kikutani. "Overview of the KEKB Accelerators". In: *Nuclear Instruments and Methods in Physics Research Section A: Accelerators, Spectrometers, Detectors and Associated Equipment*. KEK-B: The KEK B-Factory 499.1 (Feb. 2003), pp. 1–7. ISSN: 0168-9002. DOI: `10.1016/S0168-9002(02)01771-0`.

[34] Yukiyoshi Ohnishi et al. "Accelerator Design at SuperKEKB". In: *Progress of Theoretical and Experimental Physics* 2013.3 (Mar. 2013). DOI: `10.1093/ptep/pts083`.

[35] T. Abe et al. "Belle II Technical Design Report". In: *arXiv:1011.0352 [hep-ex, physics:physics]* (Nov. 2010). arXiv: `1011.0352 [hep-ex, physics:physics]`.

[36] Tetsuo Abe et al. "Achievements of KEKB". In: *Progress of Theoretical and Experimental Physics* 2013.3 (Mar. 2013). DOI: `10.1093/ptep/pts102`.

[37] Kazunori Akai, Kazuro Furukawa, and Haruyo Koiso. "SuperKEKB Collider". In: *Nuclear Instruments and Methods in Physics Research Section A: Accelerators, Spectrometers, Detectors and Associated Equipment*. Advances in Instrumentation and Experimental Methods (Special Issue in Honour of Kai Siegbahn) 907 (Nov. 2018), pp. 188–199. ISSN: 0168-9002. DOI: `10.1016/j.nima.2018.08.017`.

[38] *SuperKEKB group web site*. `http://www-superkekb.kek.jp/img/ProjectedLuminosity_v20190128.png`.

[39] E. Kou et al. "The Belle II Physics Book". In: *Progress of Theoretical and Experimental Physics* 2019.12 (Dec. 2019). DOI: `10.1093/ptep/ptz106`.

[40] I. Adachi et al. "Detectors for Extreme Luminosity: Belle II". In: *Nuclear Instruments and Methods in Physics Research Section A: Accelerators, Spectrometers, Detectors and Associated Equipment*. Advances in Instrumentation and Experimental Methods (Special Issue in Honour of Kai Siegbahn) 907 (Nov. 2018), pp. 46–59. ISSN: 0168-9002. DOI: `10.1016/j.nima.2018.03.068`.

[41] J. Kemmer et al. "Low Capacity Drift Diode". In: *Nuclear Instruments and Methods in Physics Research Section A: Accelerators, Spectrometers, Detectors and Associated Equipment* 253.3 (Jan. 1987), pp. 378–381. ISSN: 0168-9002. DOI: `10.1016/0168-9002(87)90519-5`.

[42] P. Fischer et al. "Progress towards a Large Area, Thin DEPFET Detector Module". In: *Nuclear Instruments and Methods in Physics Research Section A: Accelerators, Spectrometers, Detectors and Associated Equipment*. VERTEX 2006 582.3 (Dec. 2007), pp. 843–848. ISSN: 0168-9002. DOI: `10.1016/j.nima.2007.07.108`.

[43] Z. Natkaniec et al. "Status of the Belle Silicon Vertex Detector". In: *Nuclear Instruments and Methods in Physics Research Section A: Accelerators, Spectrometers, Detectors and Associated Equipment*. Proceedings of the 13th International Workshop on Vertex Detectors 560.1 (May 2006), pp. 1–4. ISSN: 0168-9002. DOI: `10.1016/j.nima.2005.11.228`.

[44] M Akatsu et al. "MCP-PMT Timing Property for Single Photons". In: *Nuclear Instruments and Methods in Physics Research Section A: Accelerators, Spectrometers, Detectors and Associated Equipment* 528.3 (Aug. 2004), pp. 763–775. ISSN: 0168-9002. DOI: `10.1016/j.nima.2004.04.207`.

[45] Belle-ECL et al. "Electromagnetic Calorimeter for Belle II". In: *Journal of Physics: Conference Series* 587 (Feb. 2015), p. 012045. ISSN: 1742-6596. DOI: `10.1088/1742-6596/587/1/012045`.

[46] V. Aulchenko et al. "Time and Energy Reconstruction at the Electromagnetic Calorimeter of the Belle-II Detector". In: *Journal of Instrumentation* 12.08 (Aug. 2017), pp. C08001–C08001. ISSN: 1748-0221. DOI: `10.1088/1748-0221/12/08/C08001`.

[47] A. Kuzmin. "Endcap Calorimeter for SuperBelle Based on Pure CsI Crystals". In: *Nuclear Instruments and Methods in Physics Research Section A: Accelerators, Spectrometers, Detectors and Associated Equipment*. 1st International Conference on Technology and Instrumentation in Particle Physics 623.1 (Nov. 2010), pp. 252–254. ISSN: 0168-9002. DOI: `10.1016/j.nima.2010.02.212`.

[48] P. A. Čerenkov. "Visible Radiation Produced by Electrons Moving in a Medium with Velocities Exceeding That of Light". In: *Physical Review* 52.4 (Aug. 1937), pp. 378–379. DOI: `10.1103/PhysRev.52.378`.

[49] J. V. Jelley. "Cerenkov Radiation and Its Applications". In: *British Journal of Applied Physics* 6.7 (July 1955), pp. 227–232. ISSN: 0508-3443. DOI: `10.1088/0508-3443/6/7/301`.

[50] T Iijima et al. "Aerogel Cherenkov Counter for the BELLE Detector". In: *Nuclear Instruments and Methods in Physics Research Section A: Accelerators, Spectrometers, Detectors and Associated Equipment*. Proc. 7th Int. Conf on Instrumentation for Colliding Beam Physics 453.1 (Oct. 2000), pp. 321–325. ISSN: 0168-9002. DOI: `10.1016/S0168-9002(00)00652-5`.

[51] Shohei Nishida. “Study of kaon and pion identification using inclusive D^* sample”. Belle Note 779. 2005.

[52] H.Hamasaki et al. “Study of kaon and pion identification using inclusive D^* sample”. Belle Note 321. 2000.

[53] S. Iwata et al. “Particle Identification Performance of the Prototype Aerogel RICH Counter for the Belle II Experiment”. In: *Progress of Theoretical and Experimental Physics* 2016.3 (Mar. 2016). DOI: `10.1093/ptep/ptw005`.

[54] S. Iwata. “Development of the Aerogel RICH counter for a super B-factory experiment”. PhD thesis. Tokyo Metropolitan University, Tokyo, Japan, 2016. URL: `https://www-hep.phys.se.tmu.ac.jp/thesis/doc/2015-Dthesis-iwata.pdf`.

[55] M. Mrvar. “Calibration of Aerogel Ring-Imaging Cherenkov Detector in Belle II Spectrometer”. PhD thesis. University of Ljubljana, Ljubljana, Slovenia, 2019. URL: `https://confluence.desy.de/download/attachments/120379241/MancaMrvarPhD.pdf?version=1&modificationDate=1550824216591&api=v2`.

[56] Makoto Tabata et al. “Development of Transparent Silica Aerogel over a Wide Range of Densities”. In: *Nuclear Instruments and Methods in Physics Research Section A: Accelerators, Spectrometers, Detectors and Associated Equipment*. 1st International Conference on Technology and Instrumentation in Particle Physics 623.1 (Nov. 2010), pp. 339–341. ISSN: 0168-9002. DOI: `10.1016/j.nima.2010.02.241`.

[57] I. M. Frank and I. E. Tamm. “Coherent Visible Radiation of Fast Electrons Passing through Matter”. In: *Compt.Rend.Acad.Sci.URSS* 14.3 (1937), pp. 109–114. DOI: `10.3367/UFNr.0093.196710o.0388`.

[58] Makoto Tabata et al. “Hydrophobic Silica Aerogel Production at KEK”. In: *Nuclear Instruments and Methods in Physics Research Section A: Accelerators, Spectrometers, Detectors and Associated Equipment* 668 (Mar. 2012), pp. 64–70. ISSN: 0168-9002. DOI: `10.1016/j.nima.2011.12.017`.

[59] T. Iijima et al. “A Novel Type of Proximity Focusing RICH Counter with Multiple Refractive Index Aerogel Radiator”. In: *Nuclear Instruments and Methods in Physics Research Section A: Accelerators, Spectrometers, Detectors and Associated Equipment* 548.3 (Aug. 2005), pp. 383–390. ISSN: 0168-9002. DOI: `10.1016/j.nima.2005.05.030`.

[60] Peter Križan, Samo Korpar, and Toru Iijima. “Study of a Nonhomogeneous Aerogel Radiator in a Proximity Focusing RICH Detector”. In: *Nuclear Instruments and Methods in Physics Research Section A: Accelerators, Spectrometers, Detectors and Associated Equipment* 565.2 (Sept. 2006), pp. 457–462. ISSN: 0168-9002. DOI: `10.1016/j.nima.2006.05.233`.

[61] R. Pestotnik et al. “Design Optimization of the Proximity Focusing RICH with Dual Aerogel Radiator Using a Maximum-Likelihood Analysis of Cherenkov Rings”. In: *Nuclear Instruments and Methods in Physics Research Section A: Accelerators, Spectrometers, Detectors and Associated Equipment*. RICH 2007 595.1 (Sept. 2008), pp. 256–259. ISSN: 0168-9002. DOI: `10.1016/j.nima.2008.07.019`.

[62] Makoto Tabata et al. “Large-Area Silica Aerogel for Use as Cherenkov Radiators with High Refractive Index, Developed by Supercritical Carbon Dioxide Drying”. In: *The Journal of Supercritical Fluids* 110 (Apr. 2016), pp. 183–192. ISSN: 0896-8446. DOI: `10.1016/j.supflu.2015.11.022`.

[63] I. Adachi et al. “Construction of Silica Aerogel Radiator System for Belle II RICH Counter”. In: *Nuclear Instruments and Methods in Physics Research Section A: Accelerators, Spectrometers, Detectors and Associated Equipment*. The 9th International Workshop on Ring Imaging Cherenkov Detectors (RICH2016) 876 (Dec. 2017), pp. 129–132. ISSN: 0168-9002. DOI: `10.1016/j.nima.2017.02.036`.

[64] Makoto Tabata et al. “Assembly of a Silica Aerogel Radiator Module for the Belle II ARICH System”. In: *Proceedings of International Conference on Technology and Instrumentation in Particle Physics 2017*. Ed. by Zhen-An Liu. Springer Proceedings in Physics. Singapore: Springer, 2018, pp. 253–256. ISBN: 9789811313134. DOI: `10.1007/978-981-13-1313-4_48`.

[65] S. Korpar et al. “A 144-Channel HAPD for the Aerogel RICH at Belle II”. In: *Nuclear Instruments and Methods in Physics Research Section A: Accelerators, Spectrometers, Detectors and Associated Equipment*. RICH2013 Proceedings of the Eighth International Workshop on Ring Imaging Cherenkov Detectors Shonan, Kanagawa, Japan, December 2-6, 2013 766 (Dec. 2014), pp. 145–147. ISSN: 0168-9002. DOI: `10.1016/j.nima.2014.05.060`.

[66] Y. Yusa et al. “Test of the HAPD Light Sensor for the Belle II Aerogel RICH”. In: *Nuclear Instruments and Methods in Physics Research Section A: Accelerators, Spectrometers, Detectors and Associated Equipment*. The 9th International Workshop on Ring Imaging Cherenkov Detectors (RICH2016) 876 (Dec. 2017), pp. 149–152. ISSN: 0168-9002. DOI: `10.1016/j.nima.2017.02.046`.

[67] K. Ogawa et al. “Behavior of 144ch HAPDs for the Belle II Aerogel RICH in the Magnetic Field”. In: *Proceedings of International Conference on Technology and Instrumentation in Particle Physics 2017*. Ed. by Zhen-An Liu. Springer Proceedings in Physics. Singapore: Springer, 2018, pp. 315–318. ISBN: 9789811313165. DOI: `10.1007/978-981-13-1316-5_59`.

[68] H. Kakuno et al. “Readout ASIC and Electronics for the 144ch HAPD for Aerogel RICH at Belle II”. In: *Nuclear Instruments and Methods in Physics Research Section A: Accelerators, Spectrometers, Detectors and Associated Equipment*. RICH2013 Proceedings of the Eighth International Workshop on Ring Imaging Cherenkov Detectors Shonan, Kanagawa, Japan, December 2-6, 2013 766 (Dec. 2014), pp. 225–227. ISSN: 0168-9002. DOI: `10.1016/j.nima.2014.04.053`.

[69] R. Pestotnik et al. “Front-End Electronics of the Belle II Aerogel Ring Imaging Detector”. In: *Nuclear Instruments and Methods in Physics Research Section A: Accelerators, Spectrometers, Detectors and Associated Equipment* (Dec. 2018). ISSN: 0168-9002. DOI: `10.1016/j.nima.2018.12.026`.

[70] Shohei Nishida et al. “Development of the Readout ASIC for the 144ch HAPD for Aerogel RICH”. In: *Nuclear Instruments and Methods in Physics Research Section A: Accelerators, Spectrometers, Detectors and Associated Equipment*. 1st International Conference on Technology

and Instrumentation in Particle Physics 623.1 (Nov. 2010), pp. 504–506. ISSN: 0168-9002. DOI: `10.1016/j.nima.2010.03.051`.

[71] *CAEN web site*. `http://www.caen.it`.

[72] M. Yonenaga et al. “Development of Slow Control System for the Belle II ARICH Counter”. In: *Nuclear Instruments and Methods in Physics Research Section A: Accelerators, Spectrometers, Detectors and Associated Equipment*. The 9th International Workshop on Ring Imaging Cherenkov Detectors (RICH2016) 876 (Dec. 2017), pp. 241–245. ISSN: 0168-9002. DOI: `10.1016/j.nima.2017.03.037`.

[73] M. Yonenaga et al. “Development of Slow Control System for the Belle II ARICH Counter”. In: *Proceedings of International Conference on Technology and Instrumentation in Particle Physics 2017*. Ed. by Zhen-An Liu. Springer Proceedings in Physics. Singapore: Springer, 2018, pp. 46–49. ISBN: 9789811313134. DOI: `10.1007/978-981-13-1313-4_10`.

[74] *PostgresSQL we site*. `https://www.postgresql.org`.

[75] *Control System Studio web site*. `http://controlsystemstudio.org`.

[76] *Eclipse web site*. `https://eclipse.org`.

[77] K. Hataya et al. “Development of the ARICH Monitor System for the Belle II Experiment”. In: *Nuclear Instruments and Methods in Physics Research Section A: Accelerators, Spectrometers, Detectors and Associated Equipment*. The 9th International Workshop on Ring Imaging Cherenkov Detectors (RICH2016) 876 (Dec. 2017), pp. 176–180. ISSN: 0168-9002. DOI: `10.1016/j.nima.2017.02.070`.

[78] Masanobu Yonenaga et al. “Performance and Commissioning of HAPDs in the Aerogel RICH Counter”. In: *Nuclear Instruments and Methods in Physics Research Section A: Accelerators, Spectrometers, Detectors and Associated Equipment*. 10th International Workshop on Ring Imaging Cherenkov Detectors (RICH 2018) 952 (Feb. 2020), p. 162264. ISSN: 0168-9002. DOI: `10.1016/j.nima.2019.06.005`.

[79] M. Yonenaga, *et al.* “Performance evaluation of the aerogel RICH counter for the Belle II spectrometer using early beam collision data”. to appear in PTEP. DOI: 10.1093/ptep/ptaa090.

[80] R. Pestotnik et al. “Calibration of the Belle II Aerogel Ring Imaging Detector”. In: *Nuclear Instruments and Methods in Physics Research Section A: Accelerators, Spectrometers, Detectors and Associated Equipment*. 10th International Workshop on Ring Imaging Cherenkov Detectors (RICH 2018) 952 (Feb. 2020), p. 161800. ISSN: 0168-9002. DOI: `10.1016/j.nima.2019.01.027`.

[81] P. Baillon. “Cherenkov Ring Search Using a Maximum Likelihood Technique”. In: *Nuclear Instruments and Methods in Physics Research Section A: Accelerators, Spectrometers, Detectors and Associated Equipment* 238.2 (Aug. 1985), pp. 341–346. ISSN: 0168-9002. DOI: `10.1016/0168-9002(85)90471-1`.

[82] Roger Forty. “RICH Pattern Recognition for LHCb”. In: *Nuclear Instruments and Methods in Physics Research Section A: Accelerators, Spectrometers, Detectors and Associated Equipment* 433.1 (Aug. 1999), pp. 257–261. ISSN: 0168-9002. DOI: `10.1016/S0168-9002(99)00310-1`.

[83] BILOKIN Sviatoslav. "Study of π^0 and η veto systematics using Belle II data". Belle II Note : BELLE2-NOTE-TE-2019-005.

[84] *PDG Live*. `https://pdglive.lbl.gov/Viewer.action`.

[85] Prasanth Krishnan, Manish Kumar, Minakshi Nayak, Karim Trabelsi. "K_S^0 reconstruction using phase 2 data". Belle II Note : BELLE2-NOTE-TE-2018-017.

[86] S. Tamechika and H. Kakuno, A. Ishikawa. "Study of $B \to K^*\gamma$ decays at Phase II". Belle II Note : BELLE2-NOTE-TE-2018-011.

[87] Thomas Keck. "FastBDT: A Speed-Optimized Multivariate Classification Algorithm for the Belle II Experiment". In: *Computing and Software for Big Science* 1.1 (Sept. 2017), p. 2. ISSN: 2510-2044. DOI: `10.1007/s41781-017-0002-8`.

[88] D. M. Asner et al. "Search for Exclusive Charmless Hadronic B Decays". In: *Physical Review D* 53.3 (Feb. 1996), pp. 1039–1050. DOI: `10.1103/PhysRevD.53.1039`.

[89] Particle Data Group et al. "Review of Particle Physics". In: *Physical Review D* 98.3 (Aug. 2018), p. 030001. DOI: `10.1103/PhysRevD.98.030001`.

[90] T. Skwarnicki. "A Study of the Radiative Cascade Transitions between the Upslilon-Prime and Upsilon Resonances". PhD thesis. Institute for Nueclear Physics, Krakow, The republic of Poland, 1986. URL: `http://inspirehep.net/record/230779/files/f31-86-02.pdf`.

[91] H. Albrecht et al. "Search for Hadronic B→u Decays". In: *Physics Letters B* 241.2 (May 1990), pp. 278–282. ISSN: 0370-2693. DOI: `10.1016/0370-2693(90)91293-K`.

[92] Torben Ferber. "Neutrals performance". Internal presentation.

[93] C. Cecchi, G. De Nardo, E. Manoni, M. Merola. "Study of R_2 distribution and B counting in Early Phase 3 Data". Belle II Note : BELLE2-NOTE-PH-2019-025.

[94] Naraliia Kovalchuk and Torben Ferber. "Measurement of the data to MC ratio of the photon reconstruction efficiency of the Belle II calorimeter using radiative muon pair event". Belle II Note : BELLE2-NOTE-PH-2019-028.

[95] Alexander Glazov, Petar Rados, Ami Rostomyan, Eugeno Paoloni, Laura Zani, G′uney Polat, and Justine Serrano. "Measurement of the track reconstruction efficiency in Phase 3 data using $e^+e^- \to \tau^+\tau^-$". Belle II Note : BELLE2-NOTE-PH-2020-006.

[96] S. Sandilya and A. Schwartz. "Study of Kaon and Pion Identification Performances in Phase III data with D^{*+} sample". Belle II Note : BELLE2-NOTE-PH-2019-048.

[97] A. Gaz. "Rediscovery of $B^+ \to \phi K^{(*)+}$ and $B^0 \to \phi K^{(*)0}$ using the Summer 2020 dataset". Belle II Note : BELLE2-NOTE-PH-2020-019.

[98] T. Koga, A. Selce, S. Stengel. "Optimization of π^0 reconstruction selection and first systematic uncertainty evaluation of the efficiencies". Belle II Note : BELLE2-NOTE-PH-2020-003.

Note : "Belle note" and "Belle II Note" are the internal review paper in Belle and Belle II group, respectively,